Using of Digital Image Correlation for Description of Mechanical Behaviour of Rubber during its Quasi-Static Loading

Bc. Nikolas Ryzí

Master's thesis
2022

Tomas Bata University in Zlín
Faculty of Technology

Univerzita Tomáše Bati ve Zlíně
Fakulta technologická
Ústav výrobního inženýrství

Akademický rok: 2021/2022

ZADÁNÍ DIPLOMOVÉ PRÁCE

(projektu, uměleckého díla, uměleckého výkonu)

Jméno a příjmení:	**Bc. Nikolas Ryzí**
Osobní číslo:	**T19513**
Studijní program:	**N0788A270002 Výrobní inženýrství**
Specializace:	**Stroje a nástroje pro zpracování polymerů a kompozitů**
Forma studia:	**Prezenční**
Téma práce:	**Využití digitální obrazové korelace pro popis mechanického chování pryže při jejím kvazi-statickém zatížení**

Zásady pro vypracování

1. Teoretická část
2. Mechanické vlastnosti elastomerů
3. Digitální obrazová korelace
4. Praktická část
5. Příprava série zkušebních těles
6. Provedení série experimentů (tahová zkouška, DIC, FEA)
7. Vyhodnocení výsledky, formulace závěrů

Forma zpracování diplomové práce: **tištěná/elektronická**
Jazyk zpracování: **Angličtina**

Seznam doporučené literatury:

1. Stocek R, et al. Determining Parametrical Functions Defining the Deformations of a Plane Strain Tensile Rubber Sample. Advances in Polymer Science, 2021, 286, 19-38
2. Schreier H, et al. Image Correlation for Shape, Motion and Deformation Measurements. Springer,
3. Bossuyt, S. Optimized Patterns for Digital Image Correlation. 2012

Vedoucí diplomové práce: **Ing. Martin Stěnička, Ph.D.**
Centrum polymerních systémů

Datum zadání diplomové práce: **3. ledna 2022**
Termín odevzdání diplomové práce: **13. května 2022**

L.S.

prof. Ing. Roman Čermák, Ph.D. v.r.
děkan

prof. Ing. Berenika Hausnerová, Ph.D. v.r.
ředitel ústavu

Ve Zlíně dne 18. února 2022

PROHLÁŠENÍ AUTORA
DIPLOMOVÉ PRÁCE

Beru na vědomí, že:

- diplomová práce bude uložena v elektronické podobě v univerzitním informačním systému a dostupná k nahlédnutí;
- na moji diplomovou práci se plně vztahuje zákon č. 121/2000 Sb. o právu autorském, o právech souvisejících s právem autorským a o změně některých zákonů (autorský zákon) ve znění pozdějších právních předpisů, zejm. § 35 odst. 3;
- podle § 60 odst. 1 autorského zákona má Univerzita Tomáše Bati ve Zlíně právo na uzavření licenční smlouvy o užití školního díla v rozsahu § 12 odst. 4 autorského zákona;
- podle § 60 odst. 2 a 3 autorského zákona mohu užít své dílo – diplomovou práci nebo poskytnout licenci k jejímu využití jen s předchozím písemným souhlasem Univerzity Tomáše Bati ve Zlíně, která je oprávněna v takovém případě ode mne požadovat přiměřený příspěvek na úhradu nákladů, které byly Univerzitou Tomáše Bati ve Zlíně na vytvoření díla vynaloženy (až do jejich skutečné výše);
- pokud bylo k vypracování diplomové práce využito softwaru poskytnutého Univerzitou Tomáše Bati ve Zlíně nebo jinými subjekty pouze ke studijním a výzkumným účelům (tj. k nekomerčnímu využití), nelze výsledky diplomové práce využít ke komerčním účelům;
- pokud je výstupem diplomové práce jakýkoliv softwarový produkt, považují se za součást práce rovněž i zdrojové kódy, popř. soubory, ze kterých se projekt skládá. Neodevzdání této součásti může být důvodem k neobhájení práce.

Prohlašuji,

- že jsem diplomové práci pracoval samostatně a použitou literaturu jsem citoval. V případě publikace výsledků budu uveden jako spoluautor.
- že odevzdaná verze diplomové práce a verze elektronická nahraná do IS/STAG jsou obsahově totožné.

Ve Zlíně dne: 11.4.2022

Jméno a příjmení studenta: Nikolas Rýzí

.....
podpis studenta

ABSTRAKT

Předložená práce se zabývá porovnáním spolehlivosti hyperelastických modelů konečně prvkových analýz s reálnými daty získanými experimentální analýzou za použití digitální obrazové korelace v případech deformací elastomerních materiálů při kvazistatickém zatížení v tahu. Teoretická část je zaměřena na základní popis mechanického chování elastomerů s důrazem na hyperelastickou povahu těchto materiálů a na teoretický souhrn principů digitální obrazové korelace. Praktická část se pak věnuje konkrétní použité metodice měření a tvorbě konečně prvkových simulací. V závěru jsou pak výsledky konečně prvkových simulací a reálného měření digitální obrazové korelace vzájemně porovnány a kriticky zhodnoceny tak, aby poukázaly na spolehlivost aplikovaných hyperelastických modelů.

Klíčová slova: Pryž, Hyperelasticita, Digitální obrazová korelace, DIC, Metoda konečných prvků, FEM

ABSTRACT

The presented thesis deals with reliability comparison between finite element analysis hyperelastic models' predictions and practical digital image correlation measurements in the cases of elastomer material deformations under uniaxial quasi – static loading. Theoretical part is focused on fundamental description of elastomers' mechanical behaviour with high emphasis on hyperelastic nature of these materials. Furthermore, theoretical summary of digital image correlation principles is provided. Practical part is then focused on specific digital image correlation measurement methodology and on modelling and implementation of finite element method analysis. In conclusion of the thesis, the results of finite element analysis are compared with digital image correlation measurements. The results are evaluated to highlight reliability of applied hyperelastic models.

Keywords: Rubber, Hyperelasticity, Digital Image Correlation, DIC, Finite Element Method, FEM

"Způsob, jakým lidé vnímají své okolí je pro ně nezvratným důkazem o jejich nadřazenosti a unikátnosti v porovnání s jinými formami existence. Milénia arogance a sebestřednosti je dovedla k názoru, že právě tato jejich intuitivní interakce s realitou z nich dělá jediné bytosti, jež jsou schopny své okolí doopravdy vnímat a smetly ze stolu jakékoliv dohady o opaku. Svůj život a vše točící se kolem něj přizpůsobili tak, aby to korespondovalo s touto vizí. Zejména pak čas. Avšak jak jepici nedokážeme vysvětlit přísloví co můžeš udělat dnes, neodkládej na zítra, tak ani lidem nedokážeme vysvětlit myšlenkové pochody hory, která se probudila z poledního šlofíka a diví se, kam že se to poděly ty dvounohé zubaté ještěrky, které měla tak ráda."

Dítě

„Cožpak má být strop bílý, prázdný a zapomenutý? Lidé se upínají jen k normalizovanému vyjádření a to jak na stěnách tak i v životě a přitom máme tolik možností."

I hereby declare that the print version of my Master's thesis and the electronic version of my thesis deposited in the IS/STAG system are identical.

CONTENTS

INTRODUCTION

Together with increasing use of polymer materials for technical and functional products' manufacturing, requirements to decrease economic and environmental costs of designing, prototyping, manufacturing, and testing of new products and concepts are rising. One way to achieve these needs is an implementation of Finite Element Method (FEM) analysis into a designing and testing process instead of physical prototyping. This implementation is highly suitable in the case of elastomer materials for which manufacturers cannot rely on already fully established prototyping technologies as is for example 3D printing technologies used for both thermoplastic and reactoplastic materials.

By implementation of FEM analysis into prototyping and manufacturing process, a necessary simplification and efficiency is gained, together with a detailed description of complex material behaviour under combined mechanical loading. However, by transferring of a real physical product into virtual environment, an obvious need of material behaviour description under specific loading conditions arises. These information are then particularly necessary in the case of elastomer materials, which are capable of high deformations, while nonlinear nature of their hyperelastic behaviour, and possible material and geometrical complexity of tested products, substantially complicate acquiring of accurate and reliable information of their mechanical behaviour during loadings. Acquiring information about material behaviour of geometrically complex products under combined loadings is possible by implementation of Digital Image Correlation (DIC) into practical testing process. DIC in comparison with basic mechanical testing methods as is for example tensile test is capable to provide highly accurate behaviour data for multiple values in focus within a single measurement. Furthermore, DIC measurement is time dependent, therefore it can provide description of material behaviour for individual moments throughout whole loading process. These information are highly needed to recognize product's critical areas for potential future optimization.

The aim of this thesis is to describe current means of predictive capabilities of FEM hyperelastic models and introduce possible practical implementation of this method to describe mechanical behaviour of elastomer materials. Developed FEM simulations will be subsequently compared with real samples' behaviour data obtained by experimental DIC measurement to clearly determine reliability and necessity of both FEM hyperelastic models' predictions and advantages of DIC measurement technique implementation for the specific quasi-static tension loading cases of focus. Furthermore, a high focus will be placed upon

potential effects of investigated materials' composition, samples' geometry, boundary conditions, measuring techniques and other external influences on practical measurements and their subsequent results and precision.

The comparison of simulated and real samples' behaviour under simple quasi – static tension outlines future possibilities of FEM and DIC implementation especially in cases of products of complex geometries under multilevel loadings.

I. THEORY

1 MECHANICAL PROPERTIES OF ELASTOMERS

Properties of elastomeric materials, which can be divided into two fundamental groups of physical properties and chemical properties, significantly differs in their basic behaviour from other materials commonly used in constructional and functional components. By physical properties we characterise properties as are elasticity, strength, hardness, and others which can be furthermore extended by description of specific loading cases as are tensile modulus, shear modulus, bulk modulus, or Poisson's ratio. These properties of elastomer materials in their vulcanized state are in comparison with other materials highly dependent on environment in which the products are used, especially on the temperature, chemical nature of the environment and due to its viscoelastic behaviour on time as well. Despite their specific aspects of usage, elastomers are necessary and, in many cases, essential and irreplaceable materials mainly for their elastic properties under static and dynamic loads, for ability to continuously re-deform without fracture, or for their damping and energy dissipation properties. However, the basic properties are not unified for all types of elastomers, because apart from environment influence, the properties are highly dependent on their compound mixture as well as on processing history and final product manufacturing conditions. Due to all these influences, it is essential to test and evaluate required properties of individual elastomer compounds before their final application. [1]

The most important and the most tested property of elastomers is elasticity, which is in their case referred as entropic elasticity. In ideal unloaded state the crosslinked polymer chains of elastomers follows random distribution and random direction, thus maximizing entropy for the entire system. This entropy can be described as an effort to minimalize inner energy of the system. When loaded, the polymer network follows direction of applied force and creates oriented structure of deformation, in which the elastic force is accumulated. Local deformation of polymer chains acts as elements of system's entropy reduction. Resulting elastic force is reaction of polymer chains and their effort to return to original state of pure entropy under unloaded, respectively undeformed condition. This effort, to return to the original state of pure entropy, can be described as reversible elastic behaviour.

Material behaviour and elastic recovery of elastomers can be in basic cases described by Hooke's law of linear elasticity, where the deformation is directly proportional to the applied stress and the inner energy required for return to the original undeformed state of pure entropy is equal to the energy used for initial deformation. However, the Hooke's law can

be used only when deformations are no larger than low percentage units. When it comes to larger deformations the linear elasticity model can no longer be used, as the elastomer behaviour does not follow Hooke's law of direct stress strain proportion ratio anymore. Behaviour of elastomers, where a deformation is no longer directly proportional to applied stress is then described as hyperelasticity with its own independent models specifically determined for cases of high elastic deformations. [2,3]

1.1 Isotropic linear elasticity

Isotropic linear elasticity is the most used method to describe mechanical behaviour of solid materials under small levels of deformation without preferred orientation.

Isotropic linear elastic materials will, under small strain levels, show following behaviour:

- Stress is directly proportional to strain.
- Material deformation is reversable; if loading is removed the material will return to the exact original geometry.
- Deformation is dependent purely on applied loads; load speeds or history of loading is irrelevant.
- Material is not characterized by orientation. When loaded, reaction of the material will be identical in all directions of fully symmetrical test sample. [4]

Isotropic linear elasticity is generally described by Hooke's law, which can be specified in several variants.

First variant is set of equations (1 – 4) determining strain under specific stress:

$$\varepsilon_{11} = \frac{1}{E}[\sigma_{11} - \upsilon(\sigma_{22} + \sigma_{33})] \tag{1}$$

$$\varepsilon_{22} = \frac{1}{E}[\sigma_{22} - \upsilon(\sigma_{33} + \sigma_{11})] \tag{2}$$

$$\varepsilon_{33} = \frac{1}{E}[\sigma_{33} - \upsilon(\sigma_{11} + \sigma_{22})] \tag{3}$$

$$\varepsilon_{12} = \frac{\sigma_{12}}{2\mu} \tag{4}$$

Where: E is Young's elasticity modulus, μ is shear modulus, and v is Poisson's ratio. [3]
The set of equations can be written in short form (Equation 5):

$$\varepsilon_{ij} = \frac{1+\nu}{E}\sigma_{ij} - \frac{\upsilon}{E}\sigma_{kk}\delta_{ij} \tag{5}$$

Where: indexes *i* and j can be values 1, 2 and 3 and δ_{ij} is the Kronecker delta function defined as (Equation 6):

$$\delta_{ij} = \begin{cases} 1, & if\ i = j, \\ 0, & if\ i \neq j. \end{cases} \tag{6}$$

Another common variant of Hooke's law description is determination of stress by applied strain (Equation 7):

$$\sigma_{ij} = 2\mu\varepsilon_{ij} + \lambda\varepsilon_{kk}\delta_{ij} \tag{7}$$

where μ is shear modulus and λ is Lame's constant.

Isotropic linear elasticity theory requires two known parameters of material behaviour obtained by practical experimental measurements. Pair of known parameters can be combined according to the Table 1. The table shows simple approach of numerical determination of unknown parameters from two experimentally measured material constants.

Table 1 Conversion equations for linear elasticity parameters

Known constants	**E**	**ν**	**μ**	**κ**	**λ**
Shear modulus μ, Bulk modulus κ	$\frac{9\kappa\mu}{3\kappa+\mu}$	$\frac{3\kappa-2\mu}{6\kappa+2\mu}$	μ	κ	$\frac{3\kappa-2\mu}{3}$
Young's modulus E, Poisson's ratio ν	E	ν	$\frac{E}{2(1+\nu)}$	$\frac{E}{3(1-2\nu)}$	$\frac{E}{(1+\nu)(1-2\nu)}$
Young's modulus E, Shear modulus μ	E	$\frac{E-2\mu}{2\mu}$	μ	$\frac{E\mu}{3(3\mu-E)}$	$\frac{\mu(E-2\mu)}{3\mu-E}$
Young's modulus E, Bulk modulus κ	E	$\frac{3\kappa-E}{6\kappa}$	$\frac{3\kappa E}{9\kappa-E}$	κ	$\frac{3\kappa(3\kappa-E)}{9\kappa-E}$
Shear modulus μ, Lame's constant λ	$\frac{\mu(3\lambda+2\mu)}{\lambda+\mu}$	$\frac{\lambda}{2(\lambda+\mu)}$	μ	$\frac{3\lambda+2\mu}{3}$	λ

The process of determination of isotropic linear elasticity model consists of experimental measurement of uniaxial tensile test, which specify stress – strain behaviour, from which Young's modulus *E* of examined material is obtained. Furthermore, transverse sample's contraction is measured and compared to the perpendicular elongation, thus obtaining Poisson's ratio.

Once two parameters are experimentally determined, their values can be used to calculate the rest of material behaviour constants according to the Table 1. The whole material model can be further used to precisely simulate behaviour and deformations of isotropic linear materials in FEM analysis.

As was described above, the main limitation of linear elastic models, when used to describe and simulate mechanical behaviour of polymer materials, is their specific area of application. Polymer materials follows linear behaviour only under small deformations, low temperature range, and low loading speeds. For cases of elastomer material simulations, where deformations are in higher ranges, or loadings are not reliably constant, it is necessary to use hyperelastic models. [3]

1.2 Isotropic hyperelasticity

Hyperelasticity and hyperelastic models are used to describe behaviour of materials which react elastically even in deformation cases of tens to hundreds of percentages to the original dimensions and which stress – strain proportion is not linear. Hyperelasticity is non-linear variation of linear elasticity and is suitable for behaviour predictions of highly deformed materials. [3,4]

These materials mainly consist of polymeric materials which include elastomers, and are characterized with following hyperelastic behaviour:

- Possible elastic deformations are several times higher than in ideally elastic materials and their ductility (elongation at break) reaches hundreds of percent to the original dimension.
- Proportion between stress and strain is highly non-linear. (Figure 1)
- Material can be deformed with relatively small forces.
- Volume stiffness is usually considerably high, and bulk modulus reaches from hundreds to thousands MPa.
- Poisson's ratio approaches value of 0.5, thus the material can be considered as incompressible in volume. [5]

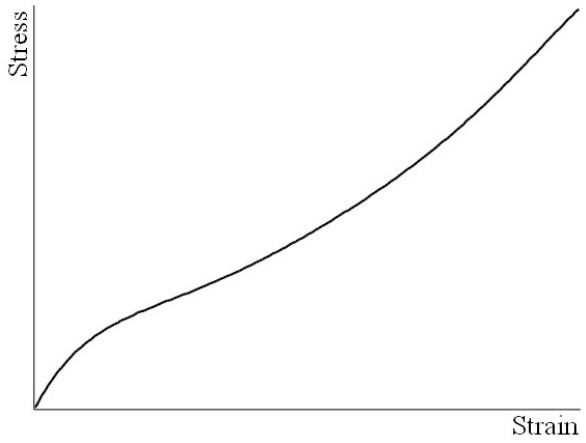

Figure 1 General stress-strain relationship curve for hyperelastic materials [5]

Another typical characteristic of elastomers' deformation behaviour is their time dependence. This behaviour acts due to braking effects of inner viscous resistance, which makes elastomer materials viscoelastic. Viscoelastic behaviour of elastomers can be described by simplified Maxwell's model, where elastic element is represented by primitive spring and viscous element by hydraulic damper.

As previously mentioned, mechanical behaviour of elastomers is highly temperature dependent when used. If the material is exposed to low temperatures its stiffness and strength increases in some cases almost to properties of metals. If the material is exposed to high temperatures its stiffness and strength decreases. [5]

However, even when a temperature of use is stable and in limits of specific elastomer type, due to crystallization behaviour of certain elastomers (NR, CR), a change in their stiffness and strength can be observed when highly deformed. This behaviour can be referred as strain – induced crystallization (SIC) and can be observed also for high cis polybutadiene (BR) when exposed to high strain levels under lower temperatures. Despite that, the changes in stiffness and strength are in both temperature and high deformation cases reversable, they significantly contribute to non-linear behaviour of specific elastomer materials. [2]

For reasons described above, it was highly necessary to place considerable effort on development of new models which could reliably describe, predict, and simulate non-linear behaviour of elastomers. [3] First basic models were considering just purely hyperelastic behaviour issue and did not consider speed and history of applied deformations. However, newly developed models consider these aspects to some degree. [5] Majority of hyperelastic models is available in most of commercial FEM software.

Samples examined in practical analysis part of this study will be submitted to primitive quasi-static loading in tens of percent deformation to the original dimension. Considering these known boundary conditions, it can be already decided that the material behaviour predictions which will be programmed and simulated in FEM software ABAQUS will have to be based on hyperelastic models.

1.2.1 Methods to acquire hyperelastic material behaviour data

The most of the hyperelastic models relies on similar sets of input data from which desired material constants with which models operate are then determined. These sets consist of stress – strain curves data of a material in focus. Typical data sets consist of uniaxial and biaxial tension curves, together with planar tension curve as illustrated on the Figure 2. [6]

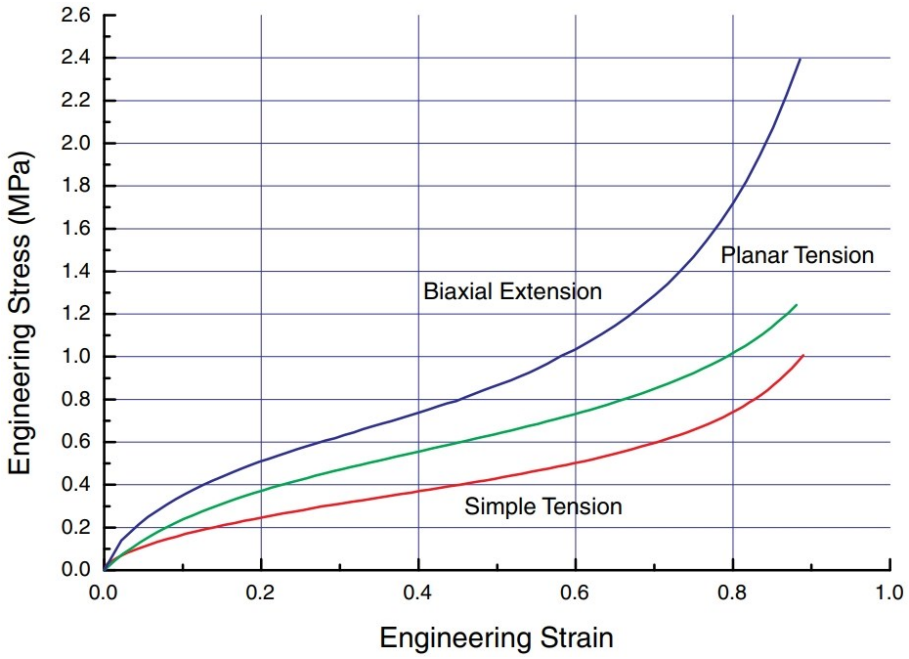

Figure 2 General representation of hyperelastic material behaviour curves [6]

The presented combination of material behaviour curves of different deformation types is used when a sample subjected to FEM simulation is under complex deformation. In these complex cases a data set from one type of deformation could not be sufficient to reliably predict resulting behaviour. Simply put a prediction of planar tension behaviour based on a data set of simple uniaxial tension would not provide reliable results, as the material response to planar tension deformation would not be sufficiently described.

Load degree needs to be considered too as in case of elastomers the difference in material response to small loads and high loads is highly probable to be diverse. Data set describing material behaviour under small deformations would not necessary reliably describe cases of predictions for high deformations. [7,8]

Therefore, experimental measurements focus to achieve the purest load type possible due to the need of precise and reliable results describing distinguish material behaviours, whereas practical experiments are not based on the description of overall yield strength or maximal tensile strength, but it is focused only on the specific area of load in which material or part will be applied. [6]

Uniaxial tension

Uniaxial tension test is the most common experimental measurement for describing material behaviour. Fundamentally, these tests consist of measurements during which a sample is subjected to loading in direction of one axis. Definition of uniaxial deformation is then based on the common premise of incompressibility of elastomers and is characterized by relative elongation: $\lambda_1=\lambda$, $\lambda_2=\lambda_3=\lambda^{-1/2}$. [9]

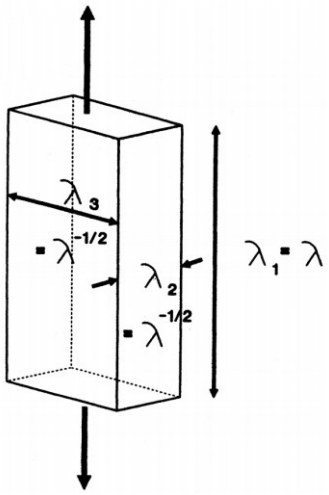

Figure 3 Principle of uniaxial tension [9]

Tensile tests are subjected to standardizations in which necessary information for practical measurements as samples geometry, methodology and boundary conditions are provided. In Europe, ISO 37 is determined for elastomers. [10]

However, in case of material data necessary for application of hyperelastic models, the standardized tests do not need to be strictly followed, as these describes material behaviour

until sample's break point, respectively tensile strength which is not always necessary when acquiring material parameters for hyperelastic models. Meanwhile the necessity to achieve pure tension and thus acquiring the most precise stress – strain curve data remains. Therefore, sample's dimension must meet requirements of minimal ratios between sample's length in the axis of load and width perpendicular to the loading axis. [6] In the case of uniaxial tension sample, the minimal length – width ratio is 10:1. [11]

The length of the sample is in this case referred as the part between fixing clamps of the tensile tester. The fixing clamps can create indefinite local stresses in the area of constrained sample's material which could seriously affect the final results. Due to this limitation a measured sample's part consists only of the length between holding clamps which is not affected by their influence and is measured by additional device called extensometer. [6]

To achieve quasi – static loading and thus maximal elimination of time and speed dependent dynamic effects, a tested sample should be exposed to slow loading speed, so the deformation speed is similarly slow. For elastomers is the speed generally between 0.004 and 0.4 s^{-1}. [12]

Biaxial tension

To achieve pure biaxial tension a flat material sample must be loaded in all direction of its main plane, thus equalling stresses in both axes of the examined part. [5]

This condition is illustrated on the Figure 6 where FEM simulation of biaxial sample loading is shown. In this particular case the light green colour represents equal stress in the plane of interest. [13]

Relative elongation for biaxial tension is defined by: $\lambda_1 = \lambda_2 = \lambda$, $\lambda_3 = \lambda^{-1/2}$.

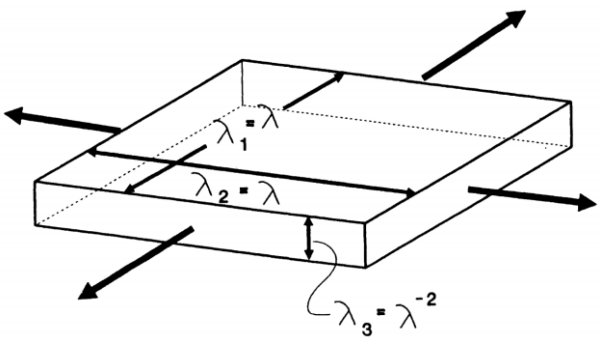

Figure 4 Principle of biaxial tension [9]

Biaxial tension can be practically achieved by several experimental methods:

- By bulging thin rubber sample by pressured air (Figure 5). [8,14]

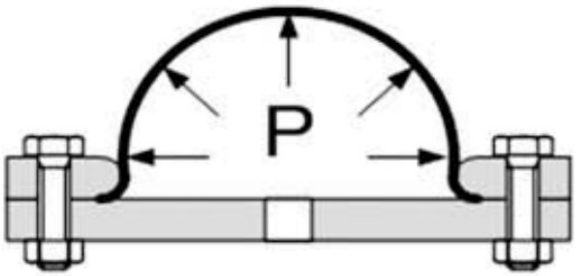

Figure 5 Biaxial tension bulge test [8]

- By radial stretching of a circular sample (Figure 6). [13,15]

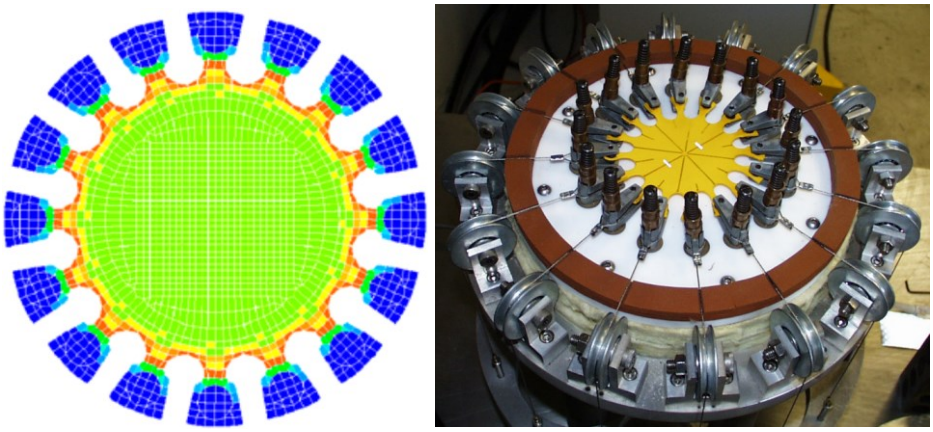

Figure 6 Biaxial radial tension test [13,15]

- By perpendicular stretching of a square sample (Figure 7). [16,17]

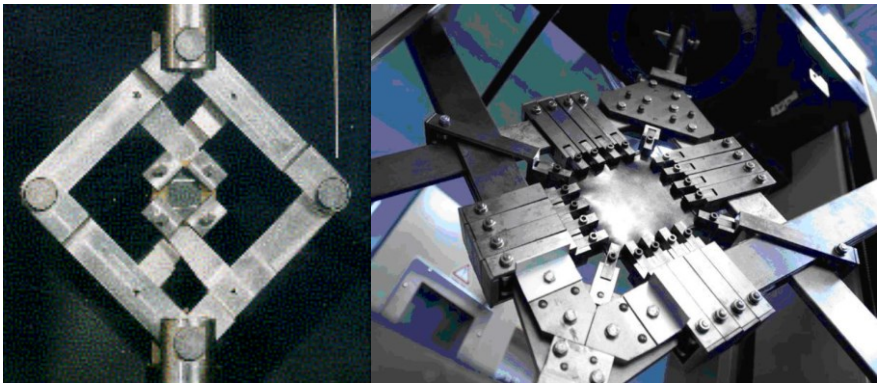

Figure 7 Biaxial perpendicular tension test [16,17]

- By dynamic stretching of a square sample (Figure 8). [18]

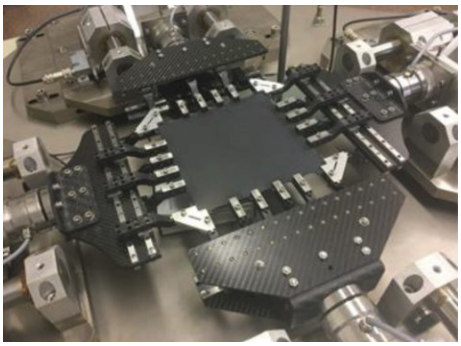

Figure 8 Biaxial dynamic tension test [19]

Planar tension

In the case of elastomers, planar tension state can be accomplished by relatively simple means. Test sample of specific geometry, where horizontal height is significantly larger than vertical height, is subjected to vertical loading. By this setup contraction occurs only in the axis of samples thickness. [6,16] Ratio between horizontal and vertical heights must be minimally 10:1 [20]

Relative elongation for planar tension is defined by: $\lambda_1=\lambda$, $\lambda_2=1$ *a* $\lambda_3=\lambda^{-1}$.

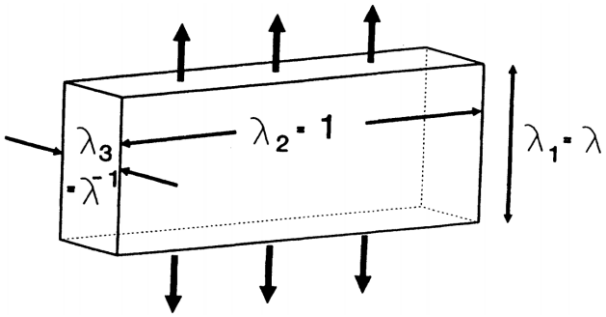

Figure 9 Principle of planar tension [9]

Figure 10 Planar tension test [5]

1.2.2 Hyperelastic models

Hyperelastic models represent basic strategy for describing deformation behaviour of elastomers. These models can be divided into two fundamental groups. Phenomenological and mechanical. The mechanical models are based on micro mechanical models of inner structure of elastomers and their material constants have specific physical meaning. The mechanical group includes models as Neo – Hookean and Arruda – Boyce. The phenomenological group consists of polynomial model, Mooney – Rivlin, Ogden and Yeoh models. Phenomenological models are based only on observations of deformation stress behaviour of elastomers on macroscopic level, in order to be capable to optimally approximate the observed behaviour. Phenomenological models' constants are usually not based on specific physical meaning. [5]

Despite these two groups, all models are based on the definition of strain energy density *W*, which is described as strain gradient tensor function: *W = W(F)*. This definition ensures pure elasticity of examined material and further use of function's scalar only.

Nowadays used hyperelastic models define general relation of strain energy density by equations (8, 9):

$$W = f(I_1, I_2, I_3\{M\}) \tag{8}$$

$$W = f(\lambda_1, \lambda_2, \lambda_3\{M\}) \tag{9}$$

Where: I_i are invariants of right Cauchy – Green strain tensor, λ_i are main stretches and *{M}* is set of material constants.

Main stretches λ_i are defined by ratio between deformed length l_i in the direction of I axis to initial undeformed length l_0 shown in equation (10):

$$\lambda_i = \frac{l_i}{l_0} \tag{10}$$

Deformation invariants I_i are defined by equations (11, 12 and 13):

$$I_1 = {\lambda_1}^2 + {\lambda_2}^2 + {\lambda_3}^2 \tag{11}$$

$$I_2 = {\lambda_1}^2{\lambda_2}^2 + {\lambda_2}^2{\lambda_3}^2 + {\lambda_3}^2{\lambda_1}^2 \tag{12}$$

$$I_3 = {\lambda_1}^2 {\lambda_2}^2 {\lambda_3}^2 \tag{13}$$

For incompressible materials $I_3 = 1$.

If the function W is known, the stress can be determined as derivation of W function by related deformation element shown in equation (14):

$$S_{ij} = 2\frac{\partial W}{\partial C_{ij}} \tag{14}$$

Where: S_{ij} is the second Piola – Kirchhoff stress tensor and C_{ij} is the right Cauchy – Green strain tensor.

If chosen coordinate system is coincident with the main deformation directions, then the right Cauchy – Green strain tensor is defined by equation (15):

$$C_{ij} = \begin{bmatrix} \lambda_1^2 & 0 & 0 \\ 0 & \lambda_2^2 & 0 \\ 0 & 0 & \lambda_3^2 \end{bmatrix} \tag{15}$$

The components of Cauchy tensor can be derived from equation (14) as equation (16):

$$\sigma_{ij} = -p\delta_{ij} + 2\frac{\partial W}{\partial I_1}C_{ij} - 2\frac{\partial W}{\partial I_2}{C_{ij}}^{-1} \tag{16}$$

where p is unspecified pressure and δ_{ij} is Kronecker constant, for which applies ($\delta_{ij} = 1$, $i = j$; $\delta_{ij} = 0$, $i \neq j$)

In the next chapters an introduction and more detailed description of individual hyperelastic models is provided. The main focus is placed upon the models which are available in the commercial FEM software ABAQUS as it will be used in practical analysis of this thesis.

Neo – Hookean Model

Neo – Hookean model is one of the oldest hyperelastic model. It is based on two material parameters. On shear modulus μ and bulk modulus κ. In addition, it is based on thermodynamic principles and statistic approach to modelling of elastomer structure. Model is defined by equations (17 and 18): [3,5]

$$W = \frac{\mu}{2}(I_1 - 3) \tag{17}$$

Where: μ is initial shear modulus defined as:

$$\mu = nkT \tag{18}$$

Where: n is number of polymer chains in unitary volume, k is Boltzmann's constant and T marks the absolute temperature.

Neo – Hookean model is intended for materials with limited compressibility, and it should be used only for cases where $\kappa >> \mu$. [4] In this case the reaction of Neo – Hookean model would be guided only by shear modulus μ. [3]

Neo – Hookean model is applicable for deformations under 40% in uniaxial loading. The Figure 11 shows predictions of Neo – Hookean model compared to experimental data. The hyperelastic predictions of uniaxial tension shows rather linear behaviour even in high strains, whereas experimental data shows sudden non-linear leap in stress – strain curve, respectively change in material's stiffness. [3]

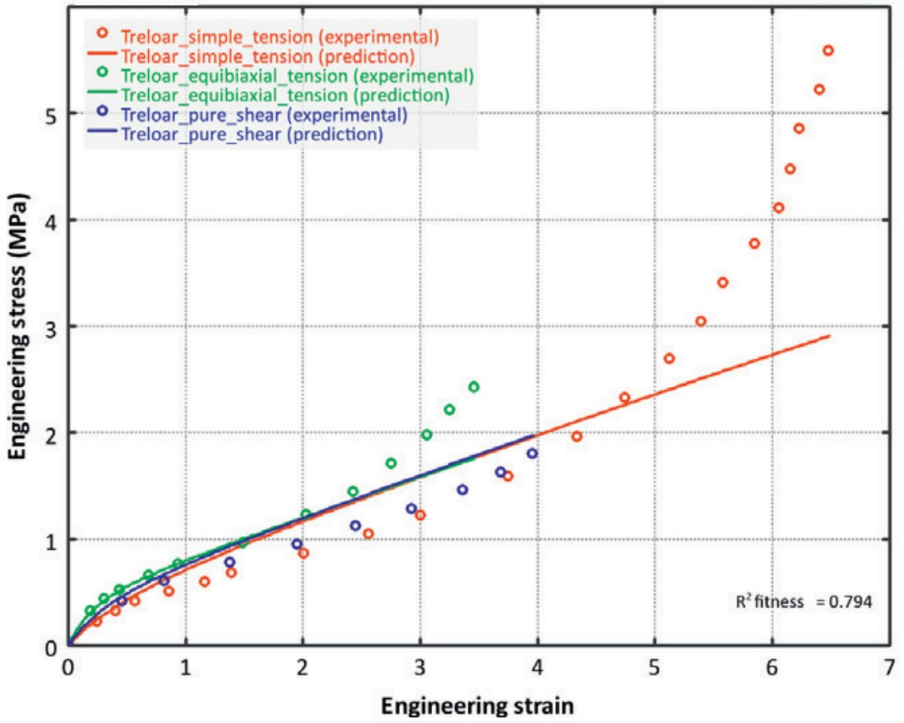

Figure 11 Comparison between experimental data and predictions from the Neo – Hookean material model [3,21]

The graphic comparison indicates that Neo – Hookean model is not reliably able to simulate hyperelastic behaviour during higher deformation levels, where stiffening phase of stress – strain response occurs. This limitation is due to model's incapacity to properly include high deformation elongations on the level of polymer chains. [3,5]

The main advantage of Neo – Hookean model is its simplicity. If shear modulus μ is known than the model is able to effectively predict material's behaviour in optional loading mode. However, the model's limitations need to be considered, as the higher deformations are applied the less accurate predictions can be provided. [3]

Arruda – Boyce Model

Arruda – Boyce model, also referred as Eight – Chain model, is based on deformation behaviour of elastomers' microstructure. The basic assumption is that macromolecules or chain molecules are, on average, located along the diagonals of a unit cell. [3,22]

The model is defined by equation (19):

$$W = \mu \sum_{i=1}^{5} \frac{C_{ij}}{\lambda_L^{2i-1}} (I_1^i - 3^i) \tag{19}$$

Where: μ is initial shear modulus and λ_L is the maximal stretch of micromechanical structure network of the material, during which the network is no longer stretched further, and stress is approaching infinite. [5]

Constants C_i are based on real values and are defined as:

$$C_1 = \frac{1}{2}, C_2 = \frac{1}{20}, C_3 = \frac{11}{1050}, C_4 = \frac{19}{7000}, C_5 = \frac{519}{673750}$$

On the Figure 12 a high improvement in predictions for high deformations can be observed. The model is applicable for deformations up to 300 % to the original dimension.

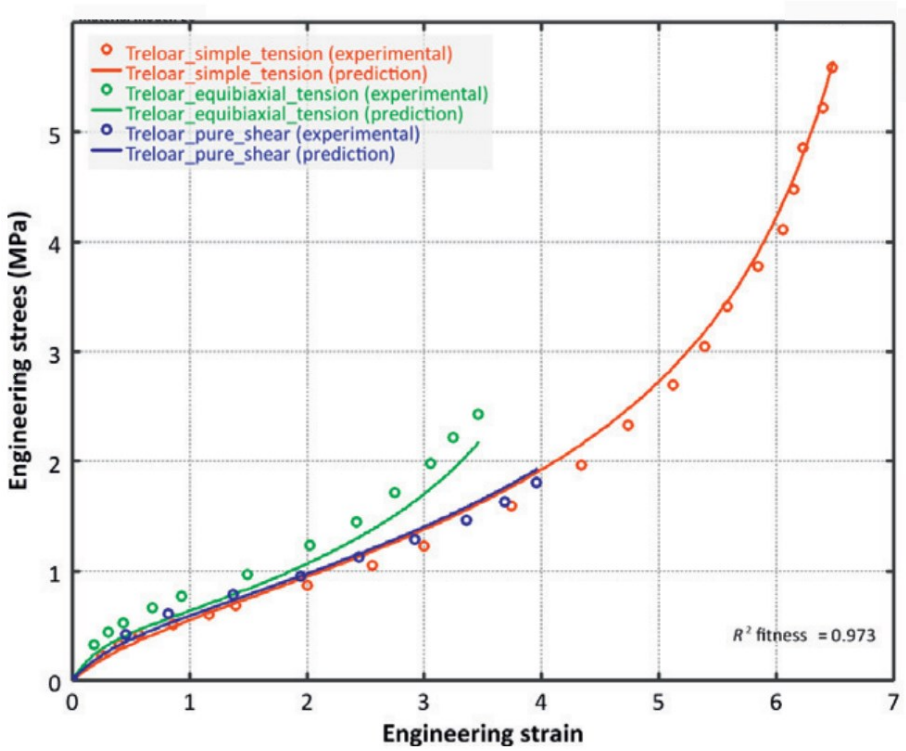

Figure 12 Comparison between experimental data and predictions from the Arruda – Boyce material model [3,23]

Polynomial Model

Polynomial model is based on the first and second deformation invariants (I_1, I_2). The function for strain energy density is then defined by equation (20):

$$W = \sum_{i+j=1}^{N} C_{ij} \, (I_1 - 3)^i (I_2 - 3)^j \tag{20}$$

Where: C_{ij} are material constants and N represents value from 1 to infinity. However, N is usually no larger than 3. [5]

This description of strain energy density is quite general and makes it difficult to determine the most suitable set of material parameters to acquire accurate predictions in multiaxial loading cases. Due to this drawback, the model is not usually used for more complex multiaxial deformation cases as are used models with fixed number of parameters. [3]

Yeoh Model

Yeoh model is similar to the polynomial form, but it is based only on the first deformation invariant. Its assessment is more difficult, and it provides less accurate results. However, it is part of the simpler models. It is defined by equation (21):

$$W = \sum_{i=1}^{N} C_{i0} \, (I_1 - 3)^i \tag{21}$$

Where: C_{i0} is material constant and N represents value from 1 to infinity. If $N = 1$ it is Neo – Hookean model.

Yeoh model is usually considered for $N = 3$. Three – parameters Yeoh model operates with three material parameters: C_{10}, C_{20} *a* C_{30} and generally provides reliable results in cases of high deformation range. Although it may not be as accurate for lower deformations. [23,24]

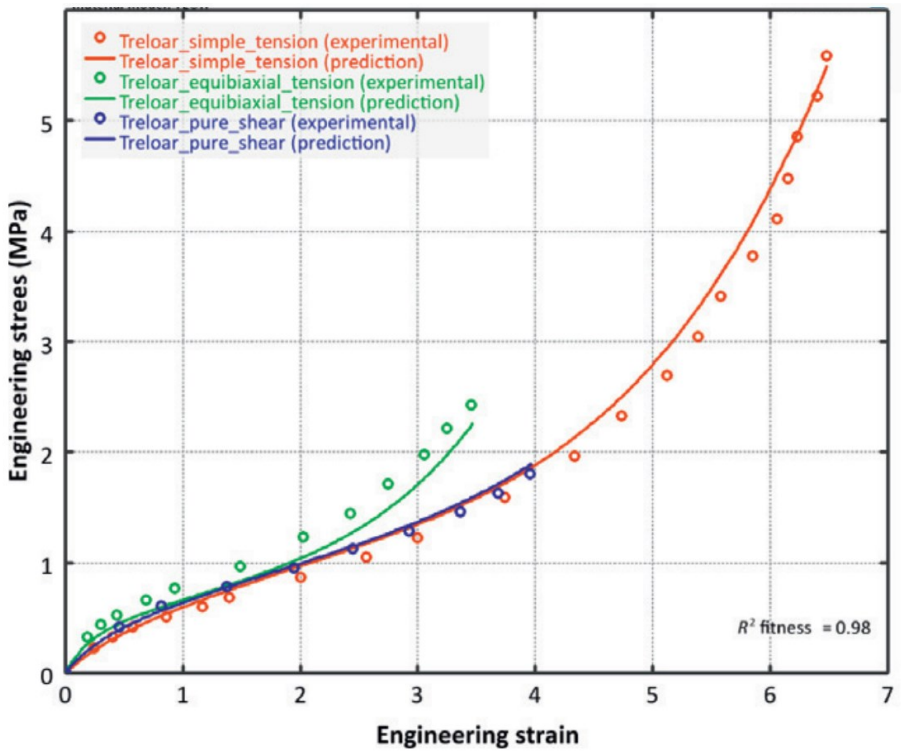

Figure 13 Comparison between experimental data and predictions from the Yeoh material model [3,21]

Mooney – Rivlin Model

Mooney – Rivlin model can be considered as an extension to the Neo – Hookean model. It attempts to improve accuracy of predictions by including a linear dependence on the second deformation invariant I_2. This linear dependence counts with linear relation between applied load and resulting shear stress during simple shear deformation. The model is used in two, three, five, and nine parameters' forms. [25,26]

Two parameters' model defined by equation (22) is the most common one and it is, in its core, equivalent to the polynomial form with $N = 1$:

$$W = C_{10}(I_1 - 3) + C_{01}(I_2 - 3) \tag{22}$$

Where: C_{10}, C_{01}, are material constants.

Multi – parameter models operate with expanded number of material constants: C_{10}, C_{01}, C_{11}, C_{20}, C_{02}, C_{30}, C_{21}, C_{12}, C_{03}.

The Figure 14 shows some improvement of predictions in comparison with Neo – Hookean model. However, the improvements often include only one type of loading while the other modes are left unstable.

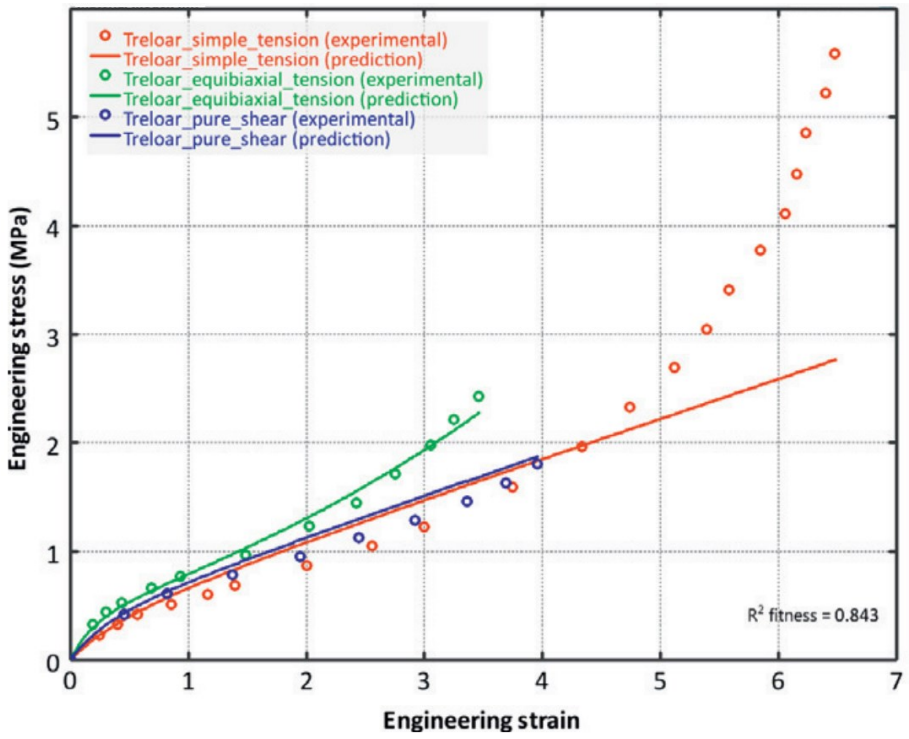

Figure 14 Comparison between experimental data and predictions from the Mooney - Rivlin material model [3,21]

Two – parameter model is usually used for deformations smaller than 100 %. While five and nine – parameter models can be used for deformations up to 300 %. [5]

Ogden Model

Ogden model is a function expressed in values of the main stretches. It is widely used for its reliability in cases of high deformation predictions. It is defined by equation (23):

$$W = \sum_{i=1}^{N} \frac{\mu_i}{\alpha_i} (\lambda_1^{\alpha_i} + \lambda_2^{\alpha_i} + \lambda_3^{\alpha_i} - 3) \quad (23)$$

Where: μ_i and α_i are material constants without specific physical meaning and N represents value 1 to infinity. N is usually no larger than 3.

For $N = 1$; $\alpha_1 = 2$ and $\mu_1 = \mu$ is Ogden equivalent to Neo – Hookean model. For $N = 2$; $\alpha_1 = 2$; $\alpha_2 = -2$; $\mu_1 = 2c_{10}$ *and* $\mu_2 = 2c_{01}$ is Ogden equivalent to two – parameter Mooney Rivlin model. Ogden can be generally applied for deformations up to 700 %. [5]

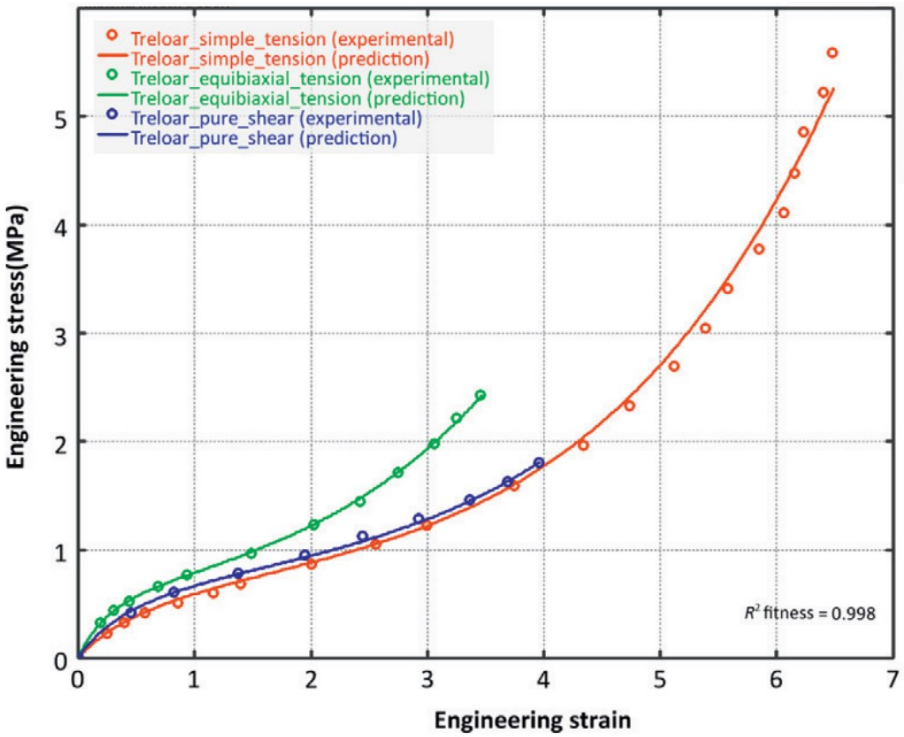

Figure 15 Comparison between experimental data and predictions from the three – parameter Ogden material model [3,21]

The Figure 15 shows improvement in predictions of three – parameter Ogden model compared to Neo – Hookean and Mooney – Rivlin models. The model is able to reliably describe S shaped stiffening phase of elastomer behaviour. However, appropriate application of Ogden model should be considered as usage of Ogden model predictions for complex deformation with pure uniaxial stress data is not recommended. [27]

The description of chosen models and definition of their strain energy density functions is based on the assumption of elastomers' absolute incompressibility, thus their independence on the third deformation invariant I_3. If inclusion of volume compressibility is desired, it is necessary to include function W_{vol} to the definitions. W_{vol} is dependent on relative volume deformation and bulk modulus κ. [5]

In the practical analysis of this theses only pure uniaxial tension is considered for the examined samples. This basic condition allows to use only material data sets measured by uniaxial tension, thus safely neglect evaluation of hyperelastic model's precision in biaxial and planar tension modes.

1.2.3 Theoretical accuracy of hyperelastic models

The predictive capabilities of hyperelastic models and their ability to simulate material behaviour curve based on material parameters, were discussed for each model in previous chapter. Comparison of predictive capabilities within one specific model as well as between different models is difficult and not always straightforward. The final results of such comparison are always based on measurements and simulations of a specific material, used geometry and boundary conditions of the experiment.

Following mutual comparison of the hyperelastic models is an illustrative summary of results published in [3,21]. Comparison is based on experimental measurement's data of natural rubber samples. [28]

Comparison of predictive capabilities can be divided into three groups:

1. **By the coefficient of determination** – by the quantified coefficient of determination (R^2) the precision of individual models can be summarized into the Table 2. The table shows that the best results can be acquired by application of three – parameters Ogden model. [3]

Table 2 Comparison of models' predictive capabilities by the coefficient of determination R^2 [3]

Hyperelastic model	R^2 – Coefficient of determination
Neo – Hookean	0.794
Arruda – Boyce	0.973
Yeoh	0.98
Mooney – Rivlin	0.843
Ogden (two – parameter)	0.977
Ogden (three – parameter)	0.998

2. **By the number of required material parameters** – in this case, it can be assumed that model which operates with lower number of material parameters is simpler for the final calibration and thus is its application more ideal and preferred in comparison with models which operates with larger number of material parameters. According to the Figure 16 Arruda – Boyce (EC) model has the most promising results of accuracy and number of parameters ratio. [3]

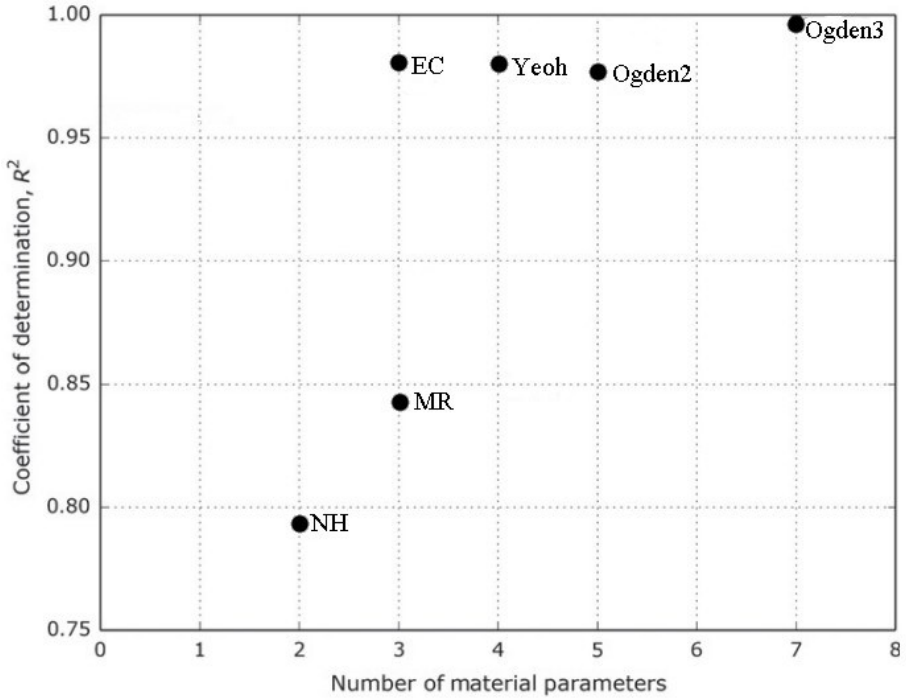

Figure 16 Comparison of models' predictive capabilities by the accuracy and the number of material parameters [3]

3. **By the minimum number of experimental measurements required for the models' calibration** – in this case, models are graded accordingly to the number of necessary deformation invariants for their application. Models based only on the first deformation invariant I_1 were graded (1) as the minimal number of experimental measurements is one. Models based on both I_1 and I_2 deformation invariants or the principal stretches were graded (2) as the minimal number of experimental measurements is two. The Figure 17 shows that by this comparison the most suitable are Yeoh and Arruda – Boyce (EC) models. [3]

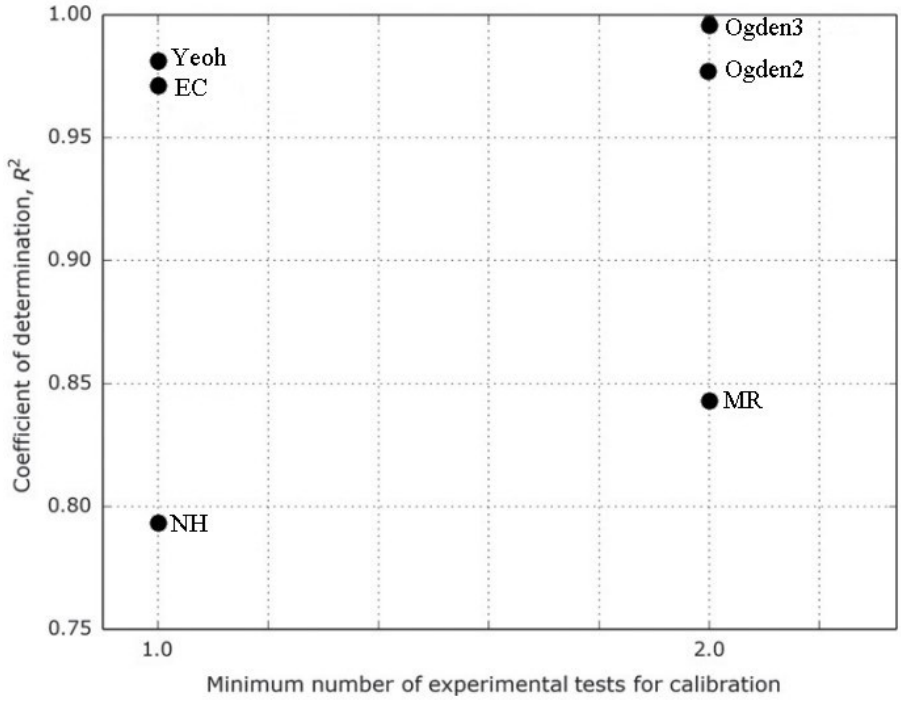

Figure 17 Comparison of models' predictive capabilities by the accuracy and the minimal number of experimental measurements required [3]

The same set of material data [28] were subjected to examination and mutual comparison of hyperelastic models in publication [29] which states following points:

- For the models available in the ABAQUS software the results showed that behaviour of elastomers can be on every level reliably described only by six – parameter Ogden model. However, the high memory and high computing power requirements were pointed out for the use of six – parameter Ogden model.
- Models that use only two or three material parameters as is Arruda – Boyce and two and three – parameter Ogden model proved as less effective, when describing full scale deformation. Their main disadvantage is in cases when the complex loading predictions are based only on material parameters acquired by a simple uniaxial set of deformation data.
- In cases of deformation from 200 to 250 % the two – parameter Mooney – Rivlin model was the most effective one.
- For small deformations up to 150 % the Neo – Hookean model was evaluated as the most suitable as it could reliably predict different deformations despite its one material parameter requirements.

The results and recommendations published in [3,21,29] should be considered only as general suggestion of models' precision. The comparison is based on experimental measurement and subsequent predictions of specific natural rubber samples, and it considers only non – linear hyperelastic part of material behaviour, while a non – linear viscous part and possible material's history in form of Mullin's cyclic loading effect is neglected. Furthermore, the comparison is also based on specific boundary conditions which may not correspond to other different cases of experimental measurements, thus the final models' precision and reliability may vary. Because of these reasons, the provided comparison of models' precision should be considered only as illustrative and inspirational as it does not describe general state of means which could be used for predictions of different sets of material data. It is also important to state that individual evaluation and assessment of prediction quality is recommended for every new material data set. This evaluation will be part of experimental analysis part of this thesis.

2 DIGITAL IMAGE CORRELATION

As mentioned in previous chapter, need for precise and reliable material data is fundamentally critical for hyperelastic models' implementation and their subsequent reliable results, so the simulated material behaviour correlate as much as possible to the real behaviour. For this reason, it is highly necessary to know the real material behaviour and the behaviour of the sample during experimental measurements, so the results can be accordingly compared with hyperelastic models' predictions. By simplified test samples we can compare simulated and real material behaviour before the process is implemented onto a real, geometrically more complex component subjected to complex loading states. This comparison of simulated and real deformation behaviour enables us to determine precision and reliability of used hyperelastic model and therefore allows us to choose more suitable model for the specific application, improve existing model or propose fully new numerical approach. Nevertheless, acquiring description of real behaviour, respectively precise information about deformation and boundary conditions dependence, is especially difficult in the case of elastomers. However, at the same time, these information, considering high deformation values which elastomers may be subjected to, are highly required and in many cases necessary. Complexity of these deformations results in insufficiency of standard means of their recording as is mechanical extensometer which by their mechanical principle may severely affect the resulting data. These reasons lead to implementation of reliable and effective contactless measuring techniques as is Digital Image Correlation (DIC)

2.1 DIC principle

DIC is innovative optical method of surface displacements measuring. It is based on comparison of sample's surface digital images under various loading stages to the original undeformed geometry. Sample's surface is additionally covered with artificial pattern structure, composed of individual points as illustrated on the Figure 18. Images of sample's patterned surface are subsequently converted to digital form by software with correlation algorithm. Digital images are then split into individual pixel's subsets, which can be individually tracked within full load recording, thus enabling to determine their surface displacement to the original position. Software is therefore, according to local displacement data, able to create complex map of time dependent displacements for whole examined part of a sample subjected to loading. Figures 19 and 20 show initial steps of DIC measurement.

[30,31]

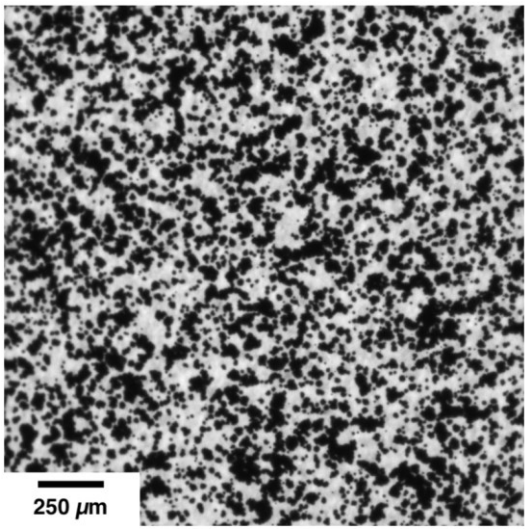

Figure 18 Pattern structure on the surface of examined sample [32]

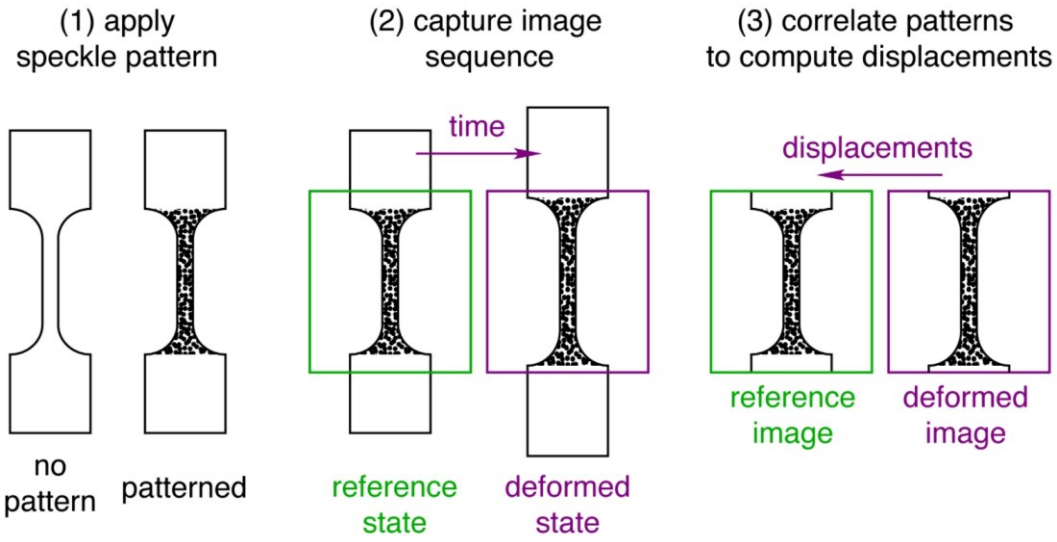

Figure 19 DIC principle [32]

After initial steps (1), where surface is patterned, reference image is created and (2), where full process of deformation is digitally captured, comes the most important step (3), where each image is correlated with the initial reference point, in other words comparing differences in patterns and subsequent calculation of displacement. [32]

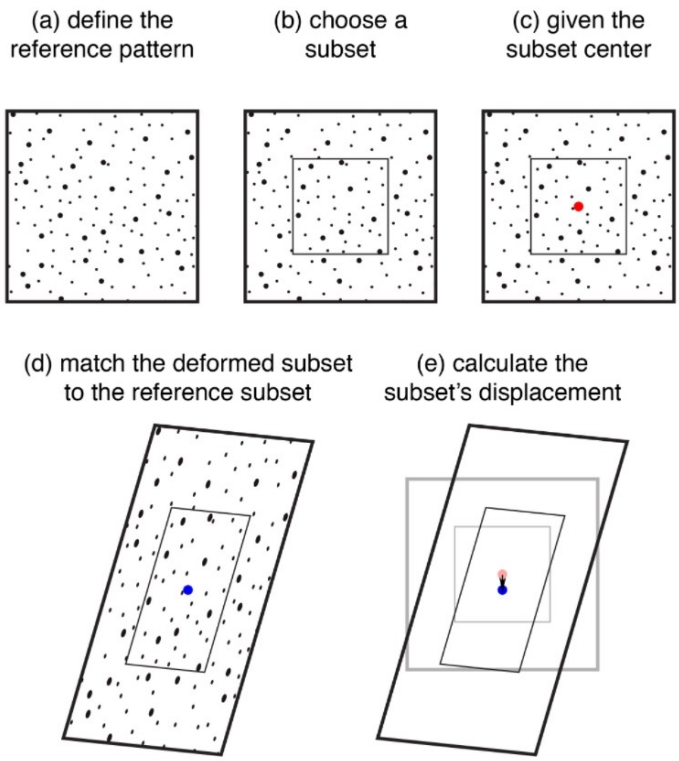

Figure 20 Process of displacement calculation [32]

Process of displacement calculation illustrated in several steps on the Figure 20 begins with definition of recognizable pattern area on which further focus is placed (a). Part of the chosen area is then selected for specific diagnostic, thus creating tracked subset (b). The subset is composed from several pixels, as it is quite difficult to track points using only one pixel. Definition of 20 × 20 pixels grid will ensure unique subset's footprint of light intensity, which can be reliably tracked by software, as it is assumed that the light intensity will not change during deformation. This process is illustrated on the Figure 21. [31,32]

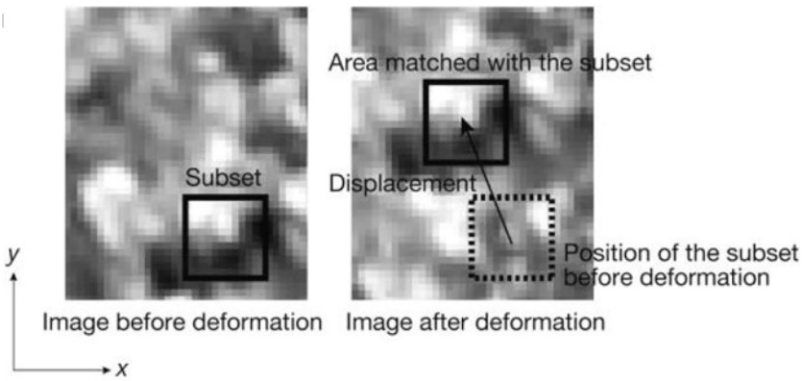

Figure 21 Illustration of subset displacement [31]

By subset's centring, using digital reference point (red dot), position from which displacement will be calculated is acquired (c). After deformation process the subset image is connected with undeformed reference image (d), while DIC software calculates relative displacement between digital centre points of both images (e). Calculated displacement is illustrated by difference between position of the original red dot and the new blue dot. [32]

To obtain full displacement field (map), it is necessary to track own and mutual subset's displacement of whole surface area. The Figure 22 illustrates identical process as figure 20 but using 2 × 2 subsets grid. [32]

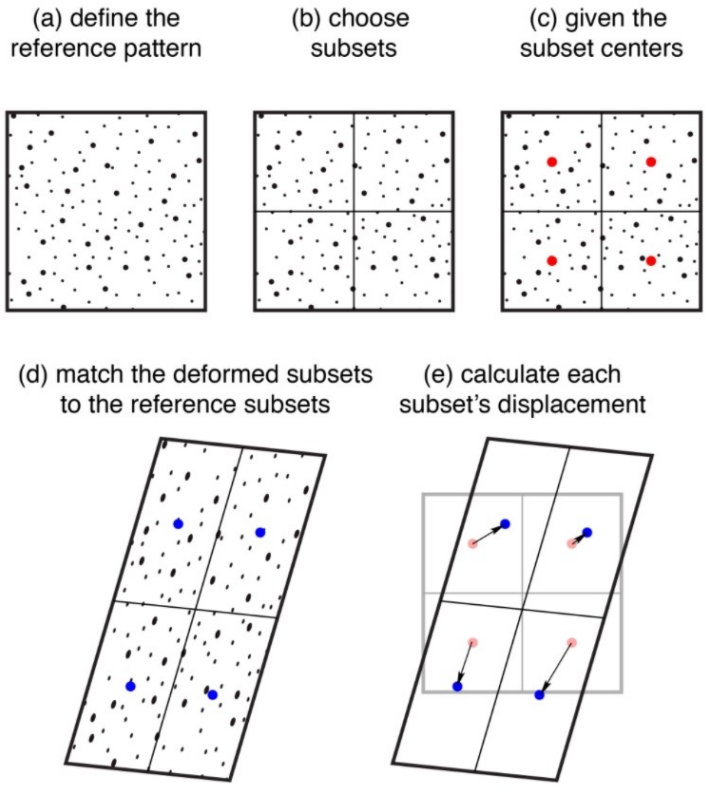

Figure 22 Process of displacement calculation using four subsets [32]

After composing all correlations together, thus creating the displacement field, we gain five points for which the displacements were calculated as shown on the Figure 23. Each of these points can be referred as DIC point.

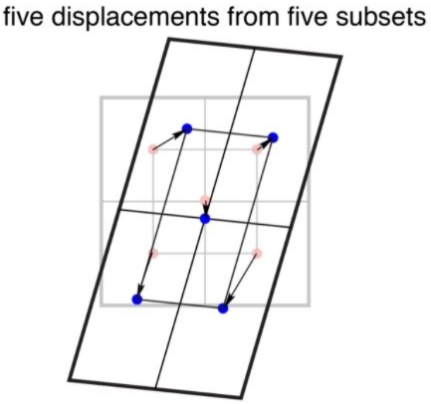

Figure 23 Displacement for five DIC points [32]

Displacement for each DIC point can be thought of as vector, which can be split into cartesian coordinate system with horizontal "*x*" and vertical "*y*" coordinate displacement. With coordinate system the whole surface area of a sample can be substitute with numerical map, which can be depicted as image field of absolute displacement values as shown on the Figure 24. In other words, the imagine field is similar illustration of stress – strain dependence as in the case of FEM systems. [32]

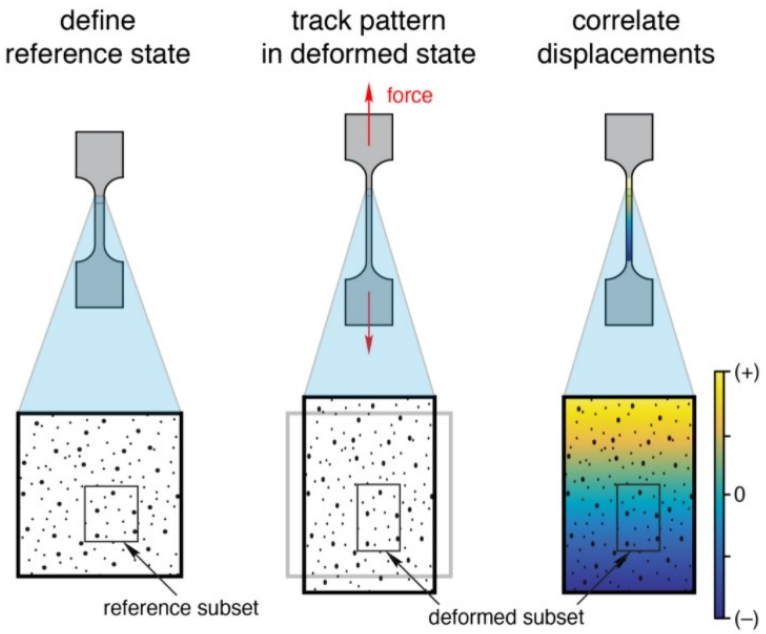

Figure 24 Illustration of image field of absolute displacement values [32]

2.2 Subset and step sizes

Setting up subset size and step size is one of the most important parts of DIC boundary conditions. Size of a subset is defined by height of reference subset square on undeformed sample's area. The step size is a distance between centres of individual subsets. Both subset size and step size are measured in pixels. [32]

The main factor in determining subset size is the quality or fineness of used patter. Each subset should contain at least three unmistakable recognizable sections of light intensity, in other words spots. [33]

The second factor is that in case of larger subsets it is more probable to found higher number of unique spots which contributes to higher accuracy of displacement tracking. However, this calibration also contributes to lower spatial resolution because as subset is larger the lower is the number of DIC points generated in the whole displacement field. [32]

Nevertheless, step size has far greater effect on the final resolution then subset size on its own. The denser are overlaps between subsets, the higher number of DIC points is generated, thus improving the final resolution. However, this results in higher computing demands and processing times. [32]

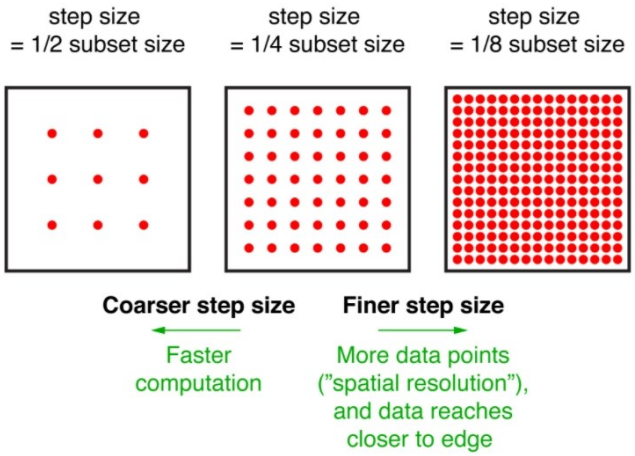

Figure 25 Illustration of step size to subset size overlapping [32]

2.3 Resolution

The final resolution is based on the smallest measurable displacement and exposition time.

- **Measurable displacement** – is limited by quality of captured images. However, these images can be smoothened via special interpolation as shown on the Figure 26.

[34,35] DIC method is capable to track displacement in order of 0.01 pixel but usually it operates within order of 0.1 pixel. [32]

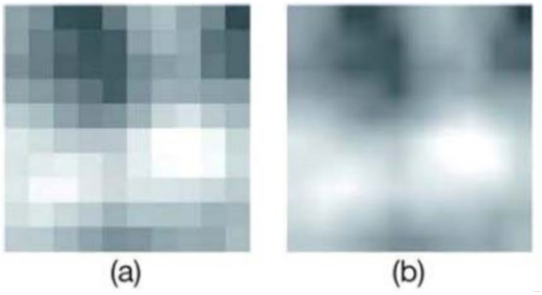

Figure 26 Original image (a); image after interpolation (b) [31]

- **Exposition time** – is highly dependent on the smallest measurable displacement as in these maximal intervals should the image be recorded. To improve reliability, the interval should be smaller than measurable displacement. In the case of smallest measurable displacement of 0.1 pixels, the interval should be even less than 0.01 pixel. If the interval would be higher than the smallest measurable displacement, the final images would be blurry, thus compromising resolution quality. [32]

2.4 Patterning

For reliable and precise use of DIC method, quality of used pattern is critical. Pattern and its application on sample's surface should follow several basic requirements when used.

a) Pattern covers only the area of interest.

b) Distribution of pattern spots should be random, but their size should be equal.

c) Pattern density should be 50 % to the original surface as shown on the Figure 27. When the density is lower or higher subsets' recognizability decreases. [36]

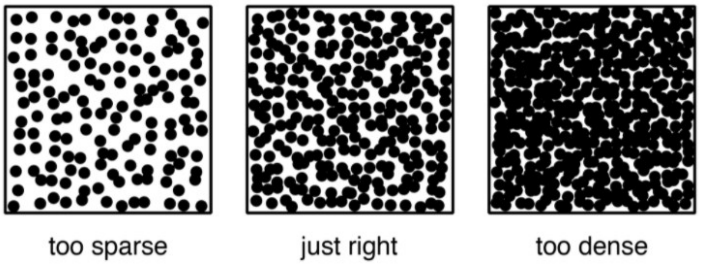

Figure 27 Illustration of pattern density [32]

d) Pattern moves and deforms together with examined surface, while pattern's mechanical properties does not influence the material properties. Ideally, a pattern should be perfectly connected to the examined material, and at the same time, its deformation should be extremely easy compared to the examined material.

e) Size of individual spots should be at least 3 × 3 pixels, so aliasing of images does not appear [37] and no larger than 7 × 7 pixels so the final DIC points density is sufficient. [36]

f) Pattern has high image contrast in comparison with the original surface. [33]

g) Spots' edges should be smooth and rounded. Aliasing could appear if the edges would be sharp. [38]

h) Pattern should be stable, consistent, and not degrading in test conditions as well as inert with material's surface.

2.4.1 Patterning methods

Several patterning methods are used mainly according to tested material.

- Paint – is used mainly for its reliable compatibility with most of construction materials, speed of application and quality of contrast. [39] In the cases of high deformation, time of paint application should be considered, as it dries and gradually loses ability to reliably co – deform with the sample after 48 hours from application. [40]
- Ink and dyes – are used mainly for hyperelastic materials as paints are unable to reliably duplicate high deformation cases. [32]
- Powder particles – are used mainly for wet and sticky surfaces on which they can adhere much easier than liquid variants. Powders can be graphite, aluminium, or magnesium. [32]
- Laser engraving – in some cases pattern needs to be created directly in the surface of the sample. Laser engraving ensures dimensional stability, even when the measurement is under extreme conditions. [41]

II. ANALYSIS

3 PREPARATION OF TEST SAMPLES

3.1 Rubber compound recipes

Two rubber compounds described in the Table 3 were used for the experimental analysis of this study. First compound was based on natural rubber (NR). Second compound was based on polybutadiene rubber (BR). N330 carbon black were used as fillers together with sulphur-based vulcanization system. Two rubber compounds, distinguished in the base rubber polymer, were used to provide extended material comparison for the experimental part of this thesis, as their individual mechanical behaviour is expected to diverse when subjected to chosen loading conditions, thus showing reliability of implemented experimental techniques regardless of material composition.

Table 3 Compounds recipe in phr

			NR	BR
Master Batch	Rubber	**NR SIR 20**	100	-
		BR Synteca 44	-	100
	Fillers	**N330 CB**	50	50
Final Batch	Vulcanization activators	**ZnO**	2	2
		Stearin	1	1
	Vulcanization accelerators	**TBBS**	1	2
		MBTS	-	0.5
	Antioxidant	**6PPD**	1	1
	Vulcanization agent	**Sulphur**	2	2
		Total phr	**157**	**158.5**

3.2 Preparation of rubber compounds

Both compounds were prepared in two steps according to the Table 4 using internal mixer SYD-2L. The final batch was then milled and sheeted using two-roll mill and stored for additional 24 h before further use.

Table 4 Compound preparation procedure

T0 [min]		**NR or BR**	
T1 [min]	Master Batch	**Fillers**	100 RPM, 70 °C (chamber)
T5 [min]		**Removal**	
T0 [min]		**Master Batch**	
T0.5 [min]	Final Batch	**ZnO + Stearin + 6PPD**	56 RPM, 70 °C (chamber)
T1.5 [min]		**TBBS + MTBS + Sulphur**	
T3 [min]		**Removal**	

3.3 Preparation of test samples

Test samples for both tensile tests and DIC measurements were prepared using hydraulic press LaBEcon 300 (Fontijne Presses, Netherlands) at temperature of 160 °C, pressure of 150 kN and curing time T_{90} = 4 min 30 s (+ 1 min per 1 mm thickness). Test samples were subsequently cut to the required dimensions.

4 EXPERIMENTAL METHODS

4.1 Tensile test

Tensile test was carried on measuring device Testometric M350-5CT (Testometric Co. Ltd., UK) and pneumatic clamps using set of ten unstandardized cut samples 100 × 10 mm for each material. The speed of the test was set on 25 mm/min. Unstandardized means of tensile measurement were chosen according to explanation stated in chapter 1.2.1.

4.2 Digital image correlation

DIC measurement was carried out using Instron 8871 tensile test machine (Instron, Canton, MA). Three sample types with specific geometry (see Figure 28) were designed for the experiment.

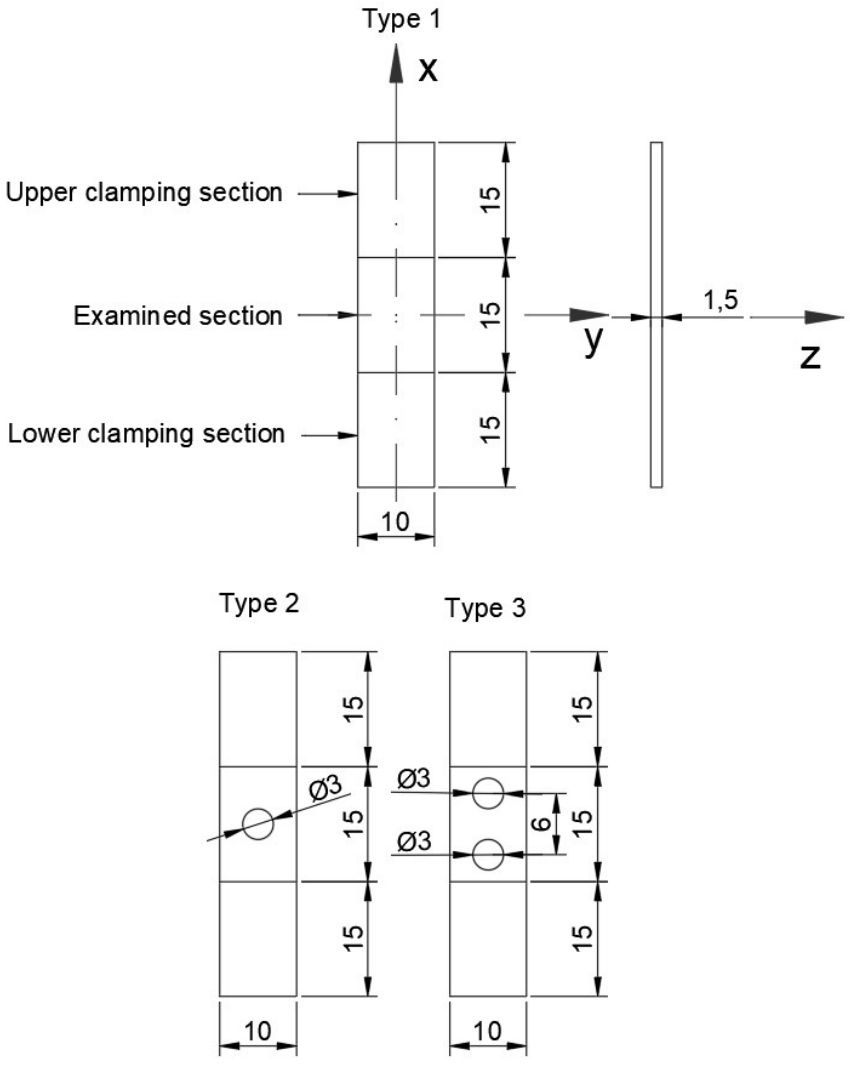

Figure 28 DIC sample types

Each samples' surface was covered with unique pattern using anti – reflective spray MR2000 Anti-Reflex L (MR Chemie GmbH, Germany) with high focus on examined section as shown on the Figure 29.

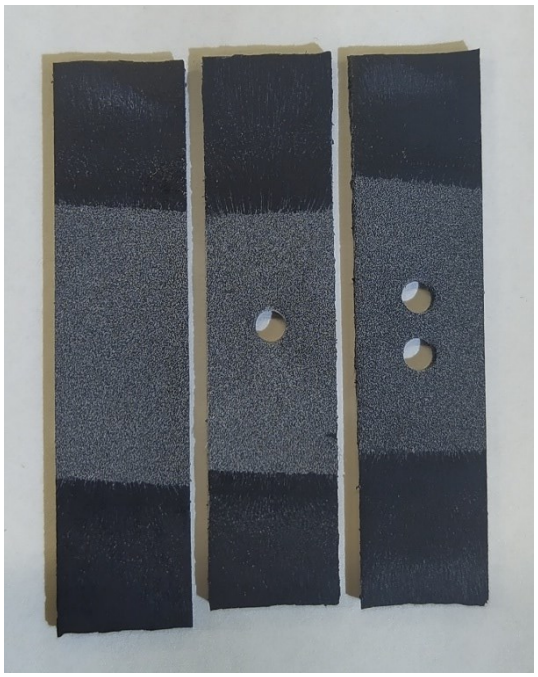

Figure 29 Samples covered with unique patterns

Patterned samples were fixed into clamps of the tensile tester according to the experimental setup scheme shown in the Figure 30. Then, samples underwent gradual stretching up to 100 % elongation of the examined section at the speed of 25 mm/min. Loading steps were recorded by monochrome camera system attached to a tripod in the presence of additional light source shown in the Figure 31.

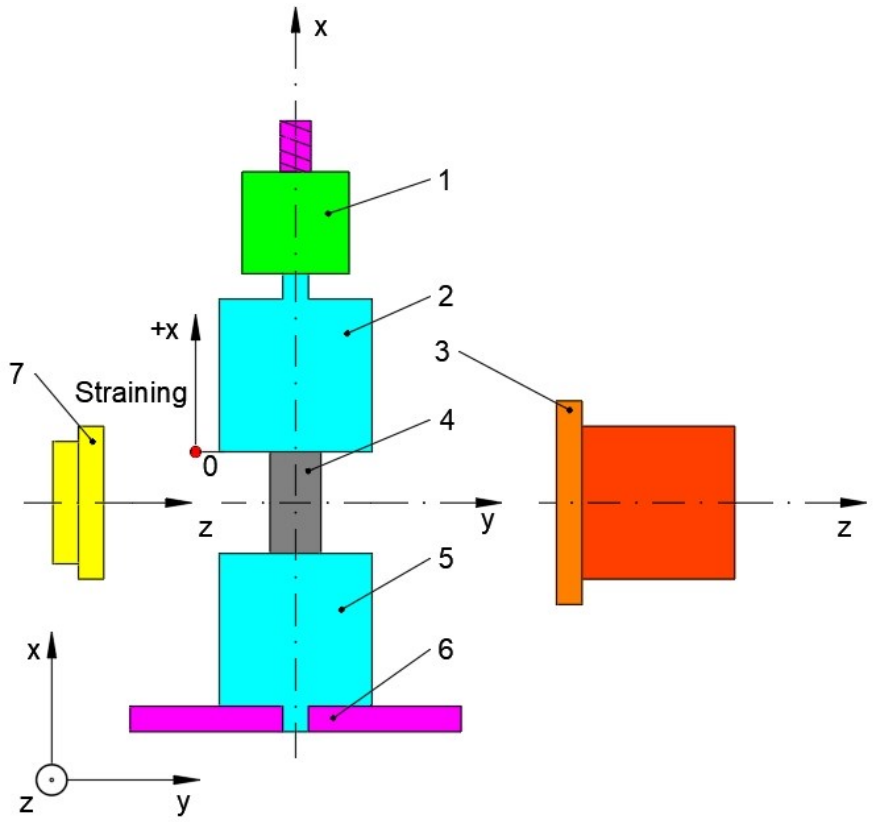

Figure 30 The scheme of INSTRON experimental DIC setup: 1 – loading cell in the x direction; 2 – upper movable clamps; 3 – monochrome camera; 4 – test sample; 5 – lower unmovable clamps; 6 – fixed base; 7 – light source

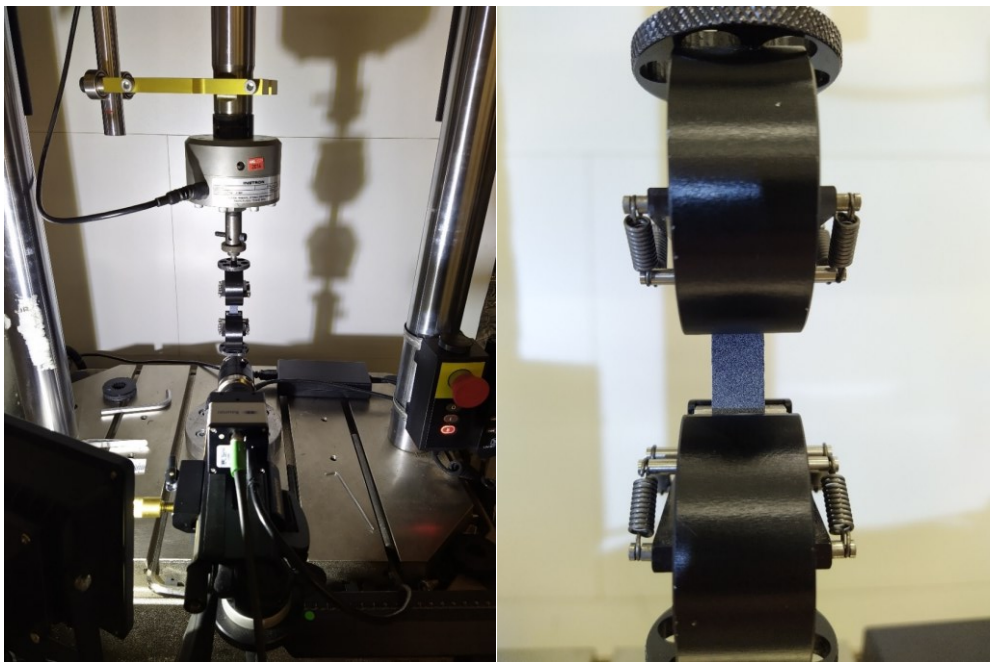

Figure 31 Picture of DIC measurement assembly

The frame recording frequency (Figure 32) was set to 15 Hz and the whole record was processed in commercial GOM Snap and evaluated in GOM Correlate DIC software (GOM Correlate, Germany) according to the method described below.

Figure 32 Single recorded frame

Needs to be shortly stated that the measurements were performed vertically as shown in the Figure 31, but for the practical purposes, the final recording, respectively the camera angle was rotated by 90° as shown in the Figure 32.

1. **Record adjustment** – the captured digital record was saved and modified through GOM Snap software. Subsequently the file was uploaded to GOM Correlate software in which the record could be edited according to the evaluation needs.

2. **Scale set up** – true scale was set up according to known sample's dimension. The scale defines main dimension value throughout the whole recording. All displacements are calculated according to this dimension value (Figure 33).

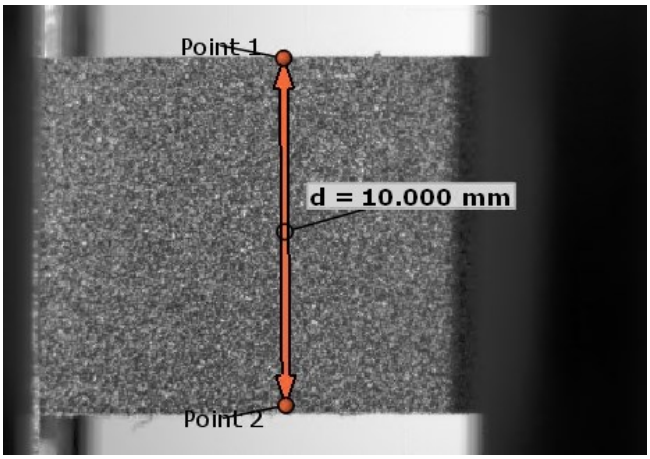

Figure 33 Scale set up

3. **Surface element set up** – surface element was created with subset size of 20 pixels and step size of 5 pixels.

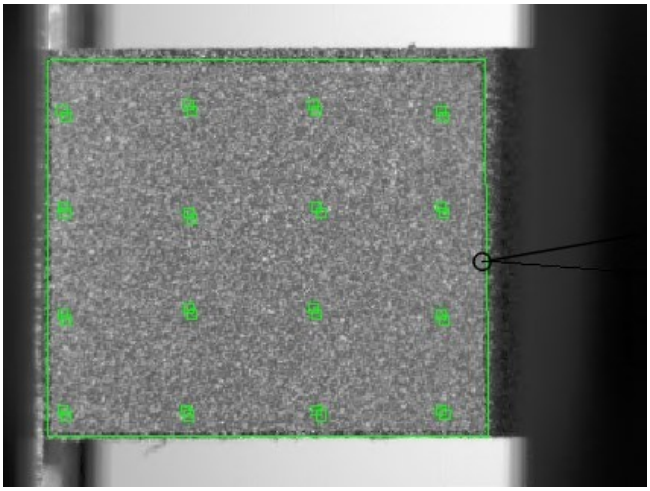

Figure 34 Surface element set up

4. **Geometry definition** – by defining specific lines (Figure 35) we acquire precise surface geometry description, with which dimensional changes throughout loading process are observed and measured. Geometries are chosen individually for each sample type according to Figures 36 and 37.

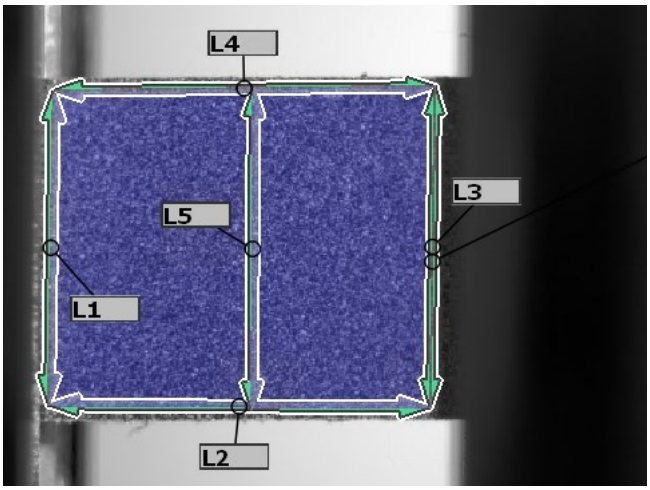

Figure 35 Geometry definition of points (left), lines (right)

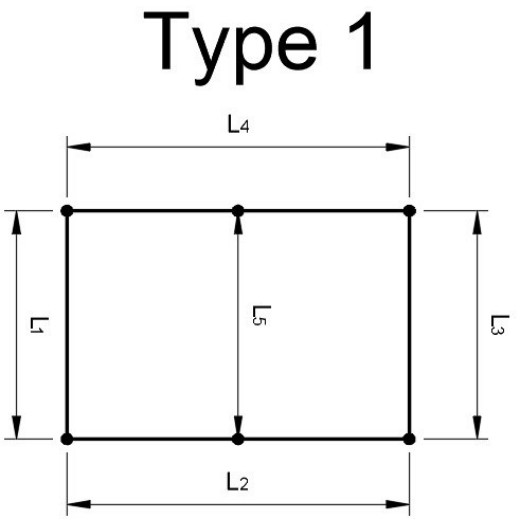

Figure 36 Type 1 geometry

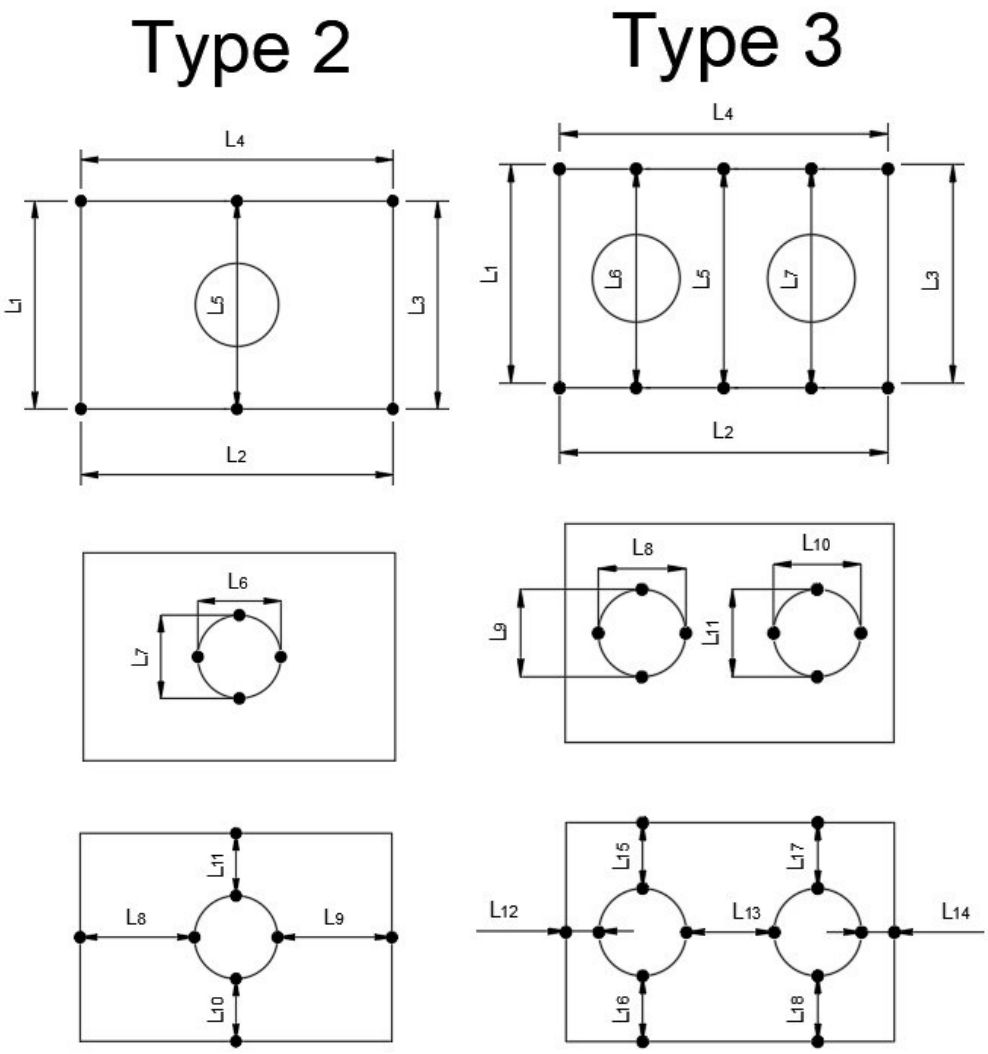

Figure 37 Type 2 geometry (left); Type 3 geometry (right)

5. **Elements' properties assignment** – after geometries definition each element is assigned with properties of focus as shown in the Figure 38. Changes in values of these properties can be observed throughout the entire process of loading. These values include lines' displacement in vertical and horizontal axis, lines' length changes, and entire element displacements.

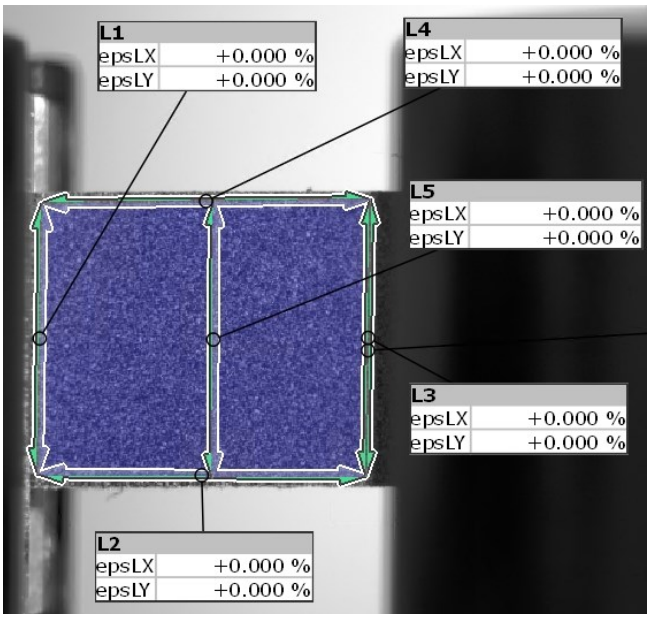

Figure 38 Elements' properties assignment

6. **Evaluation of results** – resulting values are evaluated according to the Figure 39, Table 5 and Equation 24 where:

   $\varepsilon_{x;y}$ is proportional change in transverse or lengthwise dimension, L_n is deformed length dependent on immediate strain level and L_{n0} is original length.

   The resulting data sets consist of 21 values of geometry changes to the main deformation by increments of 5 %.

$$\varepsilon_{x;y} = \left[\frac{L_n - L_{n0}}{L_{n0}}\right] \cdot 100\ [\%] \tag{24}$$

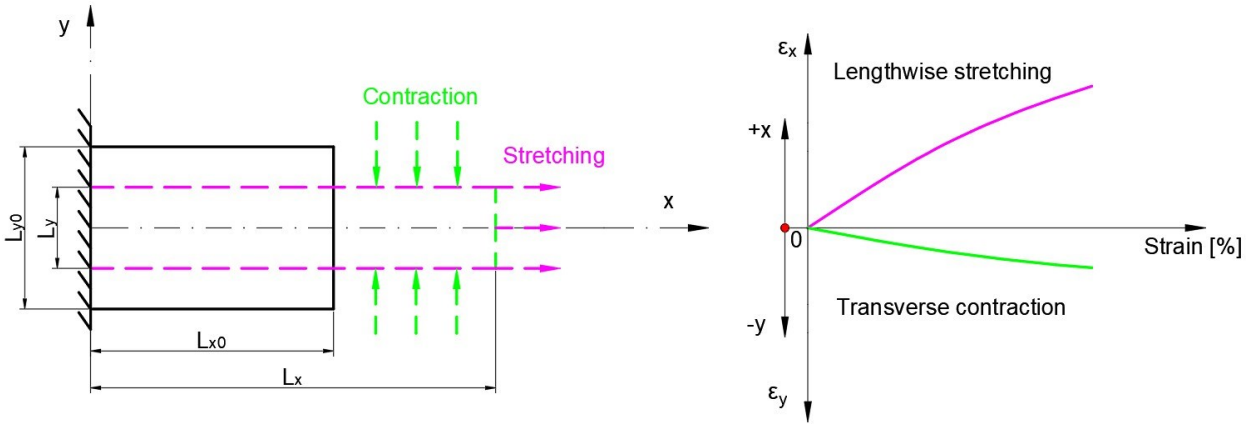

Figure 39 Loading process evaluation

Table 5 DIC values of interest

Geometry	Observed values	Strain [%]
Type 1	ε_y – L_5	0 – 100
Type 2	ε_y – L_5, L_7, L_{10}, L_{11} ε_x – L_6, L_8, L_9	0 – 100
Type 3	ε_y – L_5, L_6, L_7, L_9, L_{11}, L_{15}, L_{16}, L_{17}, L_{18} ε_x – L_8, L_{10}, L_{12}, L_{13}, L_{14}	0 – 100

Together with DIC data, each measurement provides stress – strain curves for future assessment and comparison with FEM predictions.

4.3 Finite element method

Commercial software ABAQUS was used to carry out the FEM practical part of this thesis. The analysis was carried out in two steps:

- Material data evaluation
- Modelling and load simulation

4.3.1 Material data evaluation

Complete data sets of both BR and NR mechanical behaviour obtained by tensile tests were evaluated in ABAQUS hyperelastic module for specific hyperelastic models: Neo – Hookean, Arruda – Boyce, polynomial, Yeoh, Mooney – Rivlin and Ogden described in chapter 1.2.2. Data sets were evaluated for values of 25, 50, 75 and 100 % deformation to the original length. Data evaluation, in these levels of deformation, allowed us to observe fitness and suitability of individual models not only for the maximal chosen deformation of 100 %, but for the whole load scale. Maximal strain of 100 % was chosen because rubber components usually do not exceed strains of tens of percent in practical implementation as is sealing, driving, conveyor and other application. The comparison of individual models is based on the interpolation of stress – strain curves obtained from the individual models' predictions and stress – strain curves of the original tensile data. Stress – strain curves are subsequentially subjected to linear regression, from which coefficient of determination R^2 is acquired for each model. Coefficient of determination R^2 is capable to describe values of fitness of interpolated curves, where if $R^2 = 1$ the course of compared curves fully correlates, whereas if value R^2 approaches zero, the similarity in course of inspected curves decreases. Coefficient of determination R^2 is calculated according to equation (25):

$$R^2 = 1 - \frac{\sum_{i=1}^{N}(\hat{P}_i - P_i)^2}{\sum_{i=1}^{N}(P_i - \bar{P})^2} \tag{25}$$

Where P_i are stress – strain values from the original tensile data, $\hat{P}_i$ are stress – strain values from models' predictions, $\bar{P}$ are the average values of P_i, and N is the number of original tensile data. [42]

The main goal of this evaluation part is to determine the most suitable model which is able to reliably duplicate the original hyperelastic data.

During the last step of material evaluation, the material constants for each examined hyperelastic model will be acquired. The material constants are crucial for the modelling and prediction parts of FEM analysis.

It is necessary to state that the original tensile data obtained by practical tensile measurements needed to be edited into suitable form, so they can be appropriately used in ABAQUS and reliably compared with generated data of material behaviour predictions. This means the original tensile data which consists of hundreds of individual stress – strain points needed to be edited, so the number of points of curves is no larger than 41. Editing was done by linear strain increments of 2.5 % with corresponding stress value.

4.3.2 Modelling and load simulation

For each individual sample examined by DIC, a 2D digital sample was created (Figure 40 left) with specific dimensions obtained during DIC measurement. The sample is considered as fully deformable in the *y* axis, even in the outmost positions. To achieve this boundary condition the model needs to be transversely split with a cut on which boundary condition of zero displacement in *y* axis is placed. Furthermore, boundary condition of zero displacement in *x* axis is placed onto the left side position, ensuring full secure sample. Finally main displacement in *x* axis is applied onto the right side of the sample. All boundary conditions applied onto the model are illustrated in the Figure 40 (right), where orange arrows represent removed degrees of freedom, respectively displacement direction.

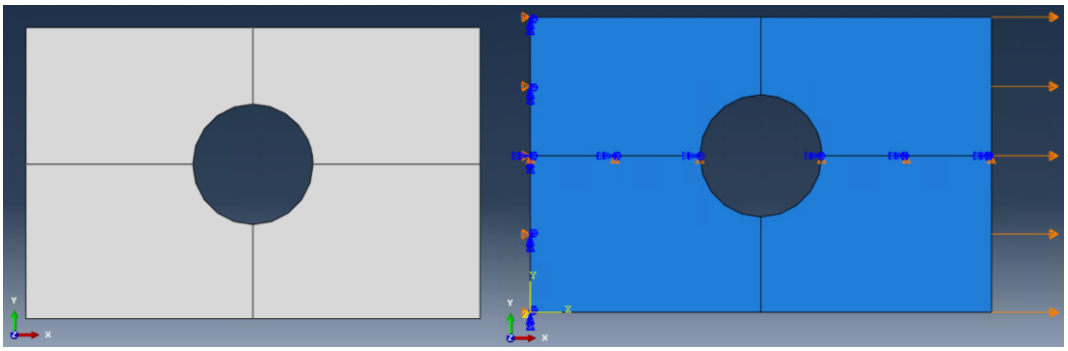

Figure 40 2D sample (left); 2D sample with boundary conditions (right)

Each model is assigned with the most propriate hyperelastic model and its material constants acquired by evaluation of tensile data. Then the model is meshed with 2D quadrangular elements CPS4R of size 0.25 mm. The mesh itself (Figure 41) needs to be structured so the final displacement readings are more precise and constant during the loading process. The structured mesh can be achieved by a second vertical cut which splits the model into four parts (Figure 40). No other boundary conditions are applied on to the vertical cut.

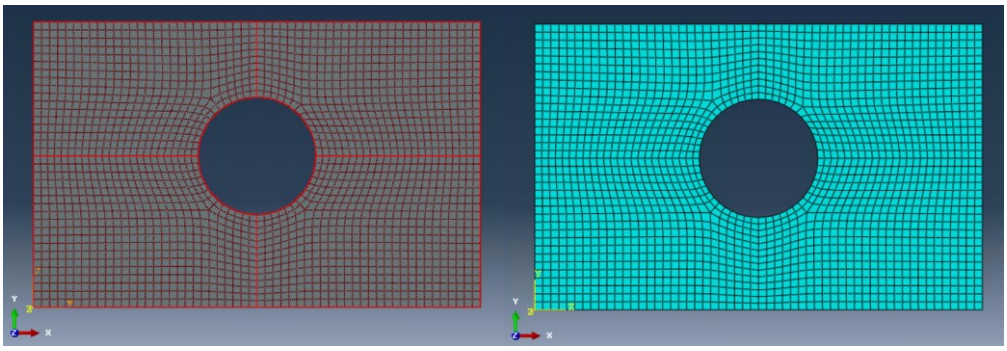

Figure 41 Meshing process (left); Final 2D mesh (right)

Final FEM analysis is set as purely static problem which enable us to neglect weight and viscoelastic effects.

Examined values are based on the samples' geometries illustrated on Figures 36 and 37 and summarized in Table 5. Displacement data are obtained together with stress data. The values were recorded up to the maximal strain of 100 % by strain steps of 5 % throughout the whole loading process. Obtained and evaluated data are compared with measured DIC data in the results and discussion chapter of this theses.

5 RESULTS AND DISCUSSION

5.1 Tensile test

The tensile tests were carried out according to description in chapter 4.1. Measured stress – strain curves for both BR and NR materials were not evaluated for standard material constants as is Young's modulus *E,* but for hyperelastic models' suitability and fitness in upcoming chapter. For each material set of 6 samples were measured. The results are presented in the figure 42 for BR and in the figure 43 for NR.

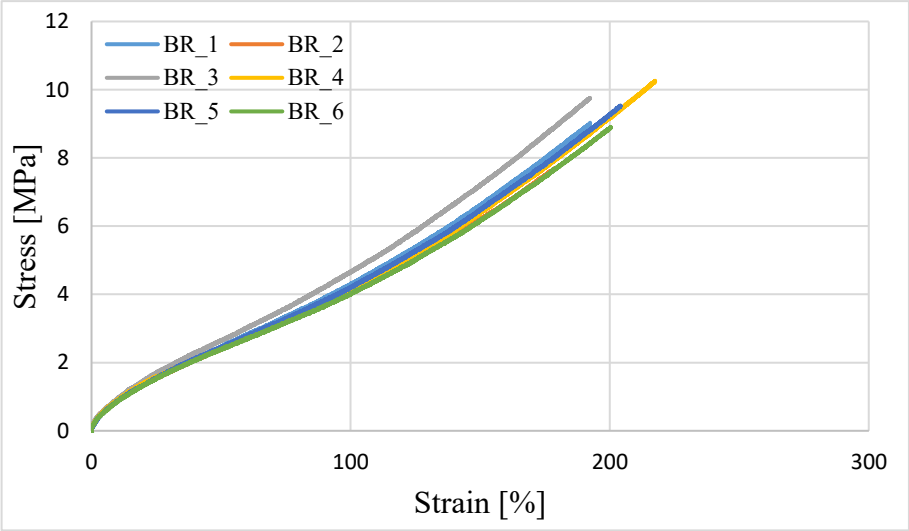

Figure 42 Stress - Strain curves of BR

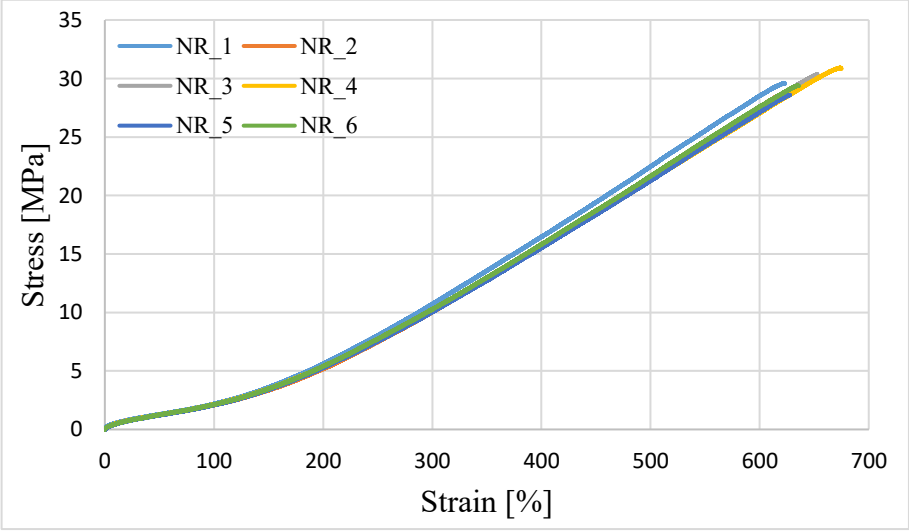

Figure 43 Stress - Strain curves of NR

5.2 Finite element method

5.2.1 Material tensile data evaluation

Material tensile data of BR and NR materials introduced in chapter 5.1 were assessed and evaluated according to chapter 4.3.1. As mentioned, it was necessary to edit the tensile data before using in ABAQUS. The final tensile curves' data consists of 41 stress – strain data points which corresponds to 41 stress – strain data points generated by hyperelastic model predictions in ABAQUS. This edit was necessary for all levels of deformations sets: 25, 50, 75 and 100%.

Results of material tensile data evaluation for both BR and NR are described in steps by individual hyperelastic models to properly present their overall fitness for the application in subsequent simulations. The focus is placed only on predictions up to 100 % strain level. At the end of this chapter short summarization for all strain levels within all hyperelastic models is provided.

Tensile data

Edited tensile data used for hyperelastic evaluation are introduced in the table 6 and the Figure 44. BR_6 and NR_6 data presented in chapter 5.1 were used as original data for subsequent editing.

Table 6 Edited tensile data for BR and NR

		BR	**NR**
n	Strain [%]	Stress [MPa]	Stress [MPa]
1	0	0	0
2	2.5	0.31	0.2
3	5	0.49	0.32
4	7.5	0.66	0.39
5	10	0.82	0.47
6	12.5	0.94	0.52
7	15	1.04	0.6
8	17.5	1.17	0.67
9	20	1.29	0.71
10	22.5	1.38	0.77
11	25	1.49	0.81
12	27.5	1.59	0.88
13	30	1.7	0.91
14	32.5	1.77	0.95
15	35	1.86	0.97
16	37.5	1.94	1.01
17	40	2.03	1.08
18	42.5	2.11	1.11
19	45	2.21	1.16
20	47.5	2.27	1.21
21	50	2.36	1.27
22	52.5	2.44	1.29
23	55	2.51	1.32
24	57.5	2.59	1.33
25	60	2.66	1.39
26	62.5	2.75	1.43
27	65	2.82	1.5
28	67.5	2.9	1.52
29	70	2.98	1.55
30	72.5	3.05	1.62
31	75	3.14	1.65
32	77.5	3.21	1.69
33	80	3.3	1.72
34	82.5	3.38	1.79
35	85	3.45	1.83
36	87.5	3.54	1.88
37	90	3.63	1.94
38	92.5	3.71	1.98
39	95	3.78	2.02
40	97.5	3.89	2.07
41	100	3.98	2.12

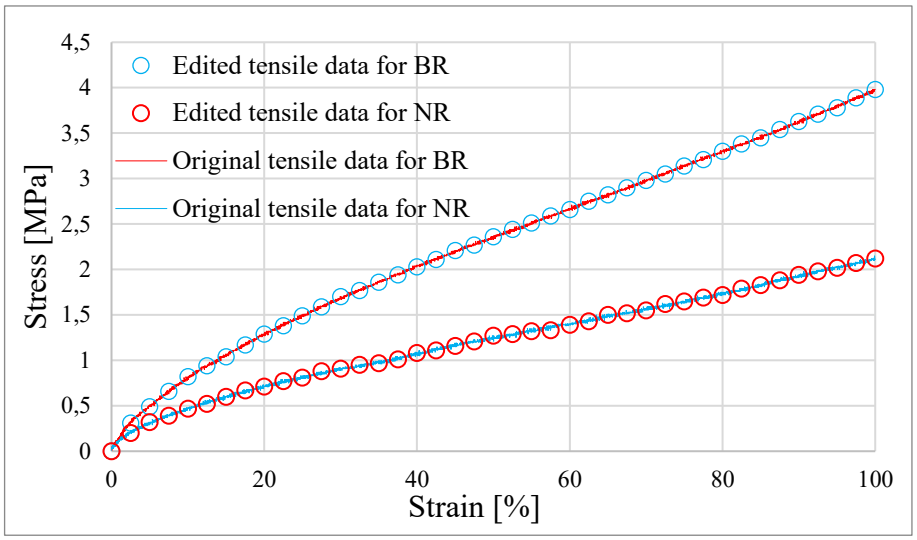

Figure 44 Edited tensile data for both BR and NR

5.2.2 Hyperelastic models comparison

Stress – strain curves of predictions of individual hyperelastic models interpolated into stress – strain curves of tensile data for both BR and NR are described in the figures 45 – 52. Coefficients of determination R^2 acquired by linear regression of tensile stress – strain data with predicted stress – strain data are written down to the Table 7 – 14 together with material coefficients for individual models.

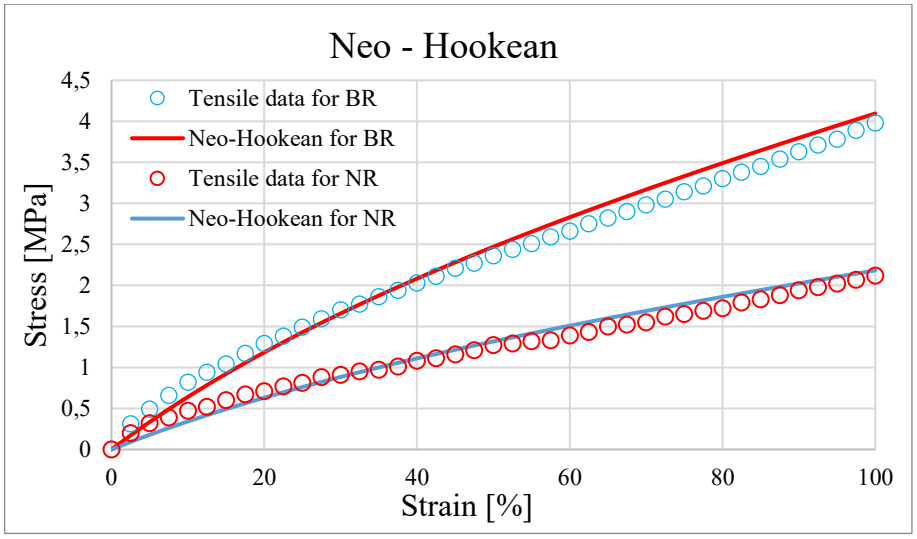

Figure 45 Comparison between original tensile data and predictions of Neo – Hookean model for both BR and NR

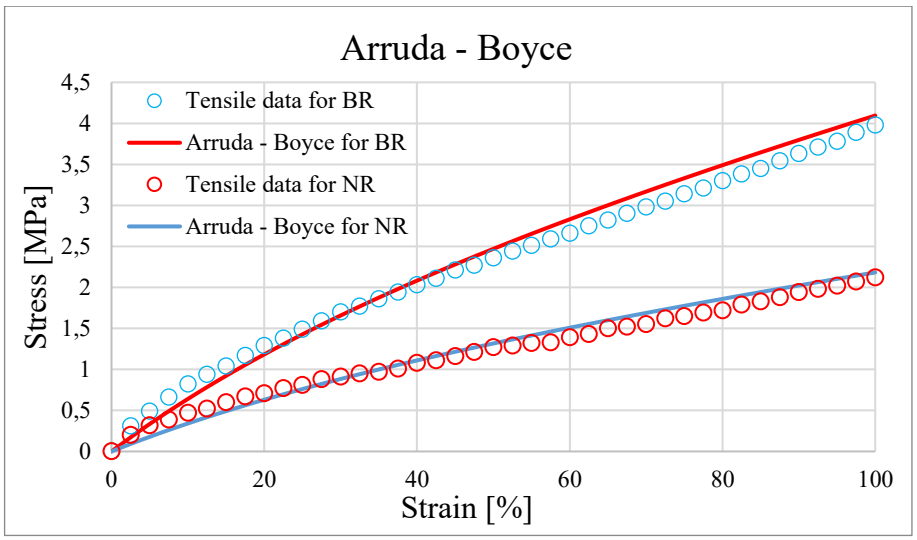

Figure 46 Comparison between original tensile data and predictions of Arruda – Boyce model for both BR and NR

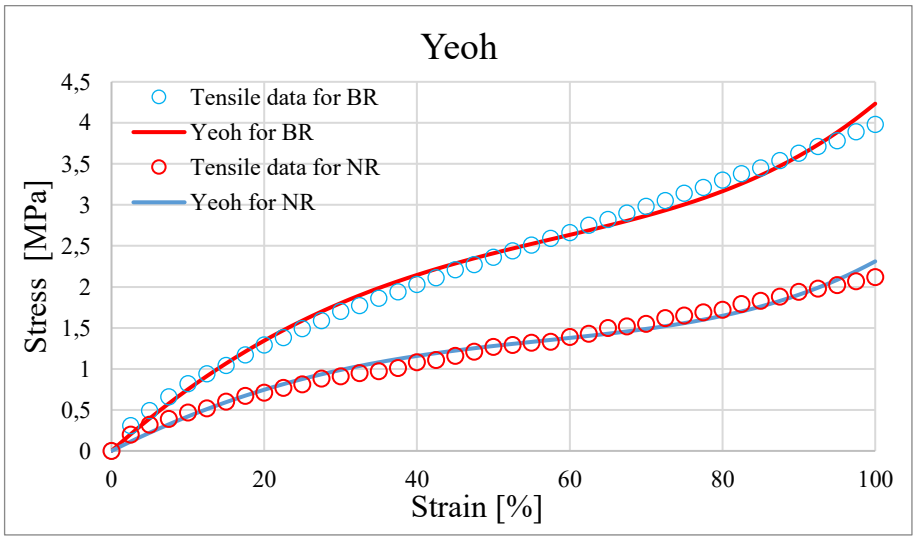

Figure 47 Comparison between original tensile data and predictions of Yeoh model for both BR and NR

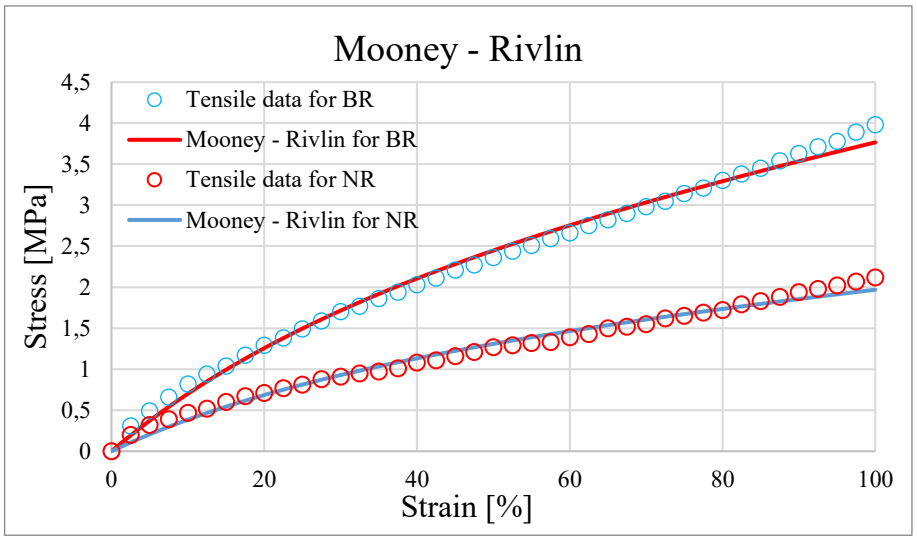

Figure 48 Comparison between original tensile data and predictions of Mooney – Rivlin model for both BR and NR

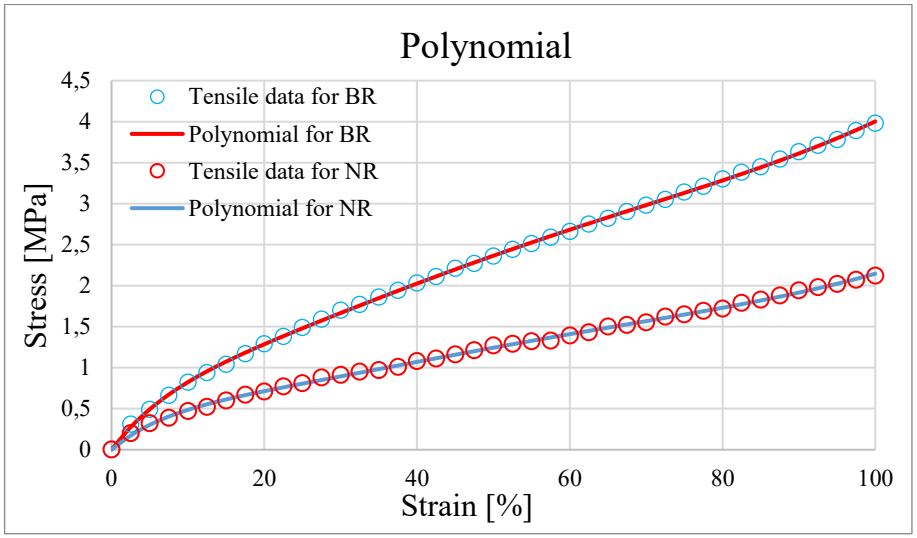

Figure 49 Comparison between original tensile data and predictions of Polynomial model for both BR and NR

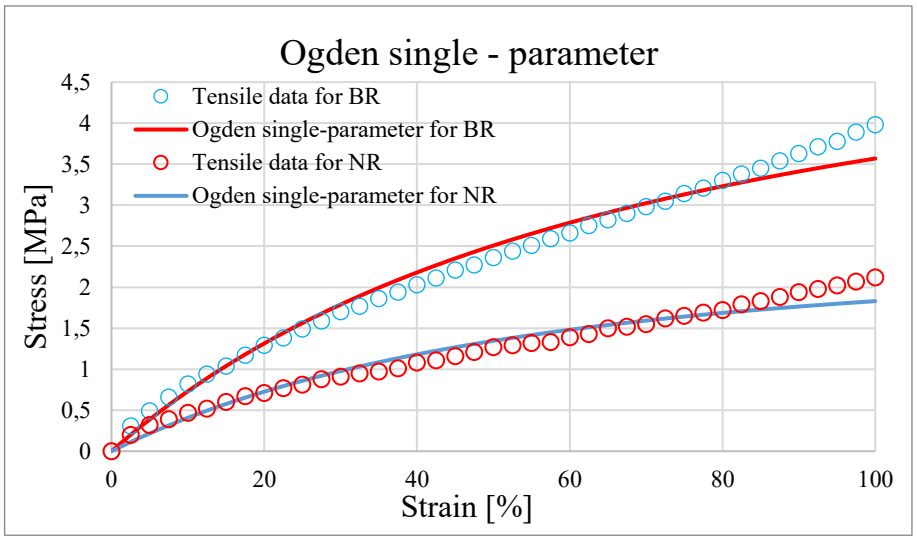

Figure 50 Comparison between original tensile data and predictions of single – parameter Ogden model for both BR and NR

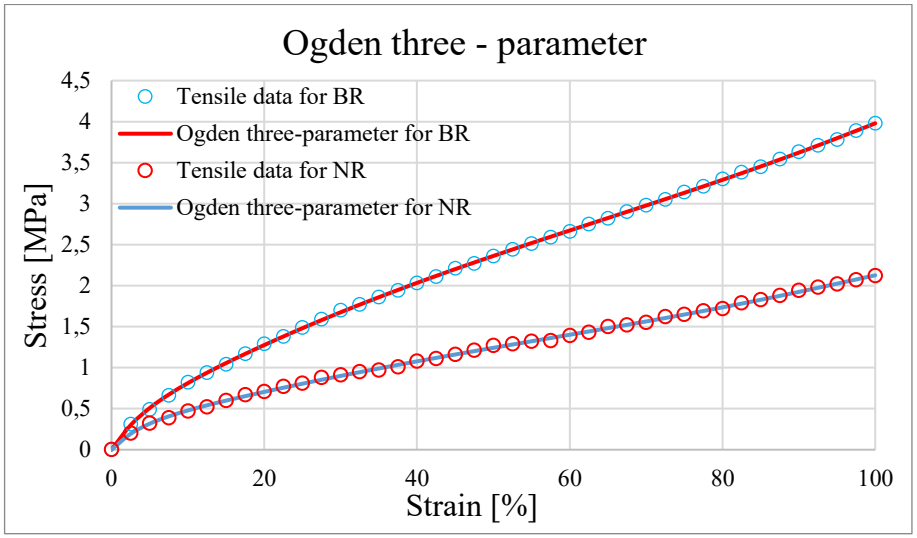

Figure 51 Comparison between original tensile data and predictions of three – parameter Ogden model for both BR and NR

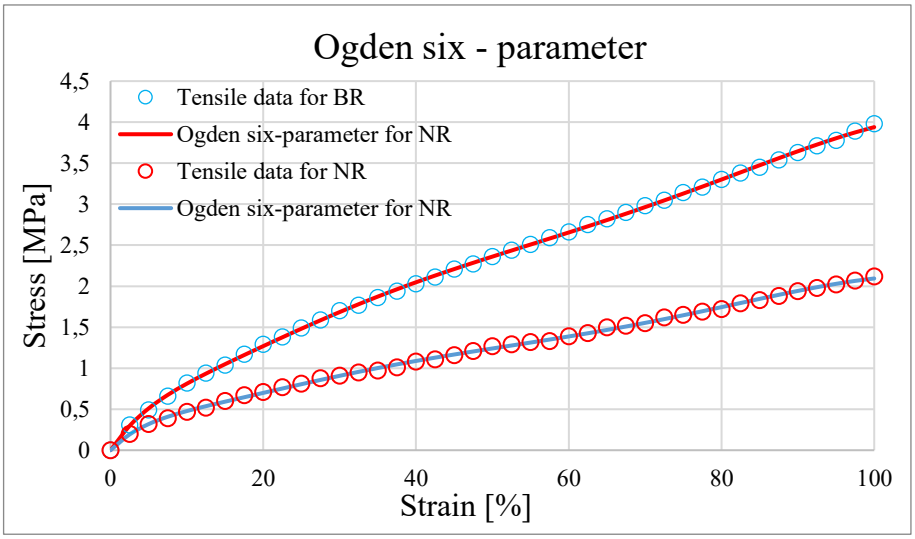

Figure 52 Comparison between original tensile data and predictions of six – parameter Ogden model for both BR and NR

Table 7 Resulting coefficient of determination R^2 and material coefficients of Neo – Hookean model for both BR and NR

	R^2		D1	C10	C01
BR	0.9986573		0	1.1700875	0
NR	0.9972214		0	0.6235453	0

Table 8 Resulting coefficient of determination R^2 and material coefficients of Arruda – Boyce model for both BR and NR

	R^2		MU	MU_0	LAMBDA_M	D
BR	0.9986573		2.3401749	2.3401751	2717.1349	0
NR	0.9972214		1.2470905	1.2470907	2118.972	0

Table 9 Resulting coefficient of determination R^2 and material coefficients of Yeoh model for both BR and NR

BR	R^2	0.9984855	**D1**	0	**C10**	1.3866996	**C01**	0	**C02**	0
			D2	0	**C20**	-0.2787453	**C11**	0	**C12**	0
			D3	0	**C30**	0.078157	**C21**	0	**C03**	0
NR	R^2	0.9971376	**D1**	0	**C10**	0.7778949	**C01**	0	**C02**	0
			D2	0	**C20**	-0.1960719	**C11**	0	**C12**	0
			D3	0	**C30**	0.0555561	**C21**	0	**C03**	0

Table 10 Resulting coefficient of determination R^2 and material coefficients of Mooney – Rivlin model for both BR and NR

	R_2		D1	C10	C01
BR	0.99885931		0	0.825883123	0.4999812
NR	0.99747016		0	0.390309518	0.3444379

Table 11 Resulting coefficient of determination R^2 and material coefficients of Polynomial model for both BR and NR

BR	R^2	0.9999661	**D1**	0	**C10**	-5.95469119	**C01**	8.00532883	**C02**	9.89234654
			D2	0	**C20**	2.19467117	**C11**	-8.0216296		
NR	R^2	0.9998505	**D1**	0	**C10**	-4.83785911	**C01**	6.14752346	**C02**	7.25603305
			D2	0	**C20**	1.564159	**C11**	-5.75541325		

Table 12 Resulting coefficient of determination R^2 and material coefficients of single – parameter Ogden model for both BR and NR

	R^2		I	MU_I	ALPHA_I	D_I
BR	0.99658436		1	2.74257387	1.0242242	0
NR	0.99346907		1	1.54376514	0.6473279	0

Table 13 Resulting coefficient of determination R^2 and material coefficients of three – parameter Ogden model for both BR and NR

	R^2		I	MU_I	ALPHA_I	D_I
BR	0.99998728		1	2.39329914	1.3734807	0
			2	-2.48778475	12.501308	0
			3	4.98422883	-24.998483	0
NR	0.99990324		1	1.28423212	1.1078029	0
			2	-2.00004355	12.501772	0
			3	4.00757286	-24.998906	0

Table 14 Resulting coefficient of determination R^2 and material coefficients of six – parameter Ogden model for both BR and NR

	R^2		I	MU_I	ALPHA_I	D_I
BR	0.99996526		1	-46.0928554	1.9998527	0
			2	6.44574148	3.9999184	0
			3	-2.80110064	5.9999608	0
			4	293.162474	-2.0001567	0
			5	-461.537857	-4.0002034	0
			6	215.555432	-6.0002242	0
NR	0.9998563		1	-39.8457268	1.9996705	0
			2	6.03760419	3.9997299	0
			3	-2.41321513	6.000015	0
			4	243.589292	-2.0003547	0
			5	-382.043957	-4.0004409	0
			6	177.849635	-6.0004708	0

Hyperelastic models' fitness comparison for 100 % strain

Despite the relatively small hyperelastic deformation during which according to [3, 8, 28] should have stand out simple Neo – Hookean model the table 15 shows, that it is together with Yeoh and Arruda – Boyce models the least reliable. Neo – Hookean and Arruda – Boyce predictions are according to the value R^2 almost identical. Both models approximate tensile data with almost linear course, which in the case of our two materials, used boundary conditions, and used loading proved to be unreliable. Yeoh model then tries to approximate the data using final stiffening S-shaped phase. However, both BR and NR materials under the small 100 % strain have not reach the stiffening phase. The best results for both BR and NR were reached by three – parameter Ogden model followed by both polynomial and six – parameter Ogden models. Despite the final order, the evaluation of uniaxial tensile data for both BR and NR materials showed high values of fitness for first four models. For simulations of simple strain problems, the multi – parameter models could be used. In a case of more complex multi – axial loading problems, for which we need to consider computing power and computing times, simpler model as is Mooney – Rivlin or polynomial model could be used.

Table 15 Comparison of hyperelastic models' fitness for 100 % strain

Material	Order	Model	R^2
BR	1	Ogden N=3	0.9999873
	2	Polynomial N=2	0.9999661
	3	Ogden N=6	0.9999653
	4	Mooney-Rivlin	0.9988593
	5	Neo-Hookean	0.9986573
	6	Arruda-Boyce	0.9986573
	7	Yeoh	0.9984855
	8	Ogden N=1	0.9965844
NR	1	Ogden N=3	0.9999032
	2	Ogden N=6	0.9998563
	3	Polynomial N=2	0.9998505
	4	Mooney-Rivling	0.9974702
	5	Neo-Hooke	0.9972214
	6	Arruda-Boyce	0.9972214
	7	Yeoh	0.9971376
	8	Ogden N=1	0.9934691

It also needs to be stated that stability limit of the models' prediction capabilities should be considered if the application consists of larger strains than those we obtained by tensile

measurements. Each model has its own limits, and it usually follows a simple rule, when the more complex model, the lower strains it can be used for. Model's instability is characterized with extremely low or extremely high constant values during its assessment. If a model is used beyond strains for which it was assessed as stable, its behaviour becomes unpredictable, thus compromising any results. [43]

Table 16 shows stability limitations for uniaxial tension according to the final order of evaluated models.

Table 16 Stability limits comparison for individual models

Material	Order	Model	Stability limits
BR	1	Ogden N=3	140 %
	2	Polynomial N=2	303 %
	3	Ogden N=6	117 %
	4	Mooney-Rivlin	Stable for all strains
	5	Neo-Hookean	Stable for all strains
	6	Arruda-Boyce	Stable for all strains
	7	Yeoh	Stable for all strains
	8	Ogden N=1	Stable for all strains
NR	1	Ogden N=3	130 %
	2	Ogden N=6	111 %
	3	Polynomial N=2	315 %
	4	Mooney-Rivling	Stable for all strains
	5	Neo-Hooke	Stable for all strains
	6	Arruda-Boyce	Stable for all strains
	7	Yeoh	Stable for all strains
	8	Ogden N=1	Stable for all strains

Hyperelastic models' fitness comparison for all deformation levels

Figures 53 to 56 shows, that the models evaluated as the best for strain up to 100 % are similarly suitable for all evaluated strain levels. Furthermore, results show correlation between rising strain and increase in suitability for both Neo – Hookean and Arruda – Boyce models. Mooney – Rivlin and Yeoh models acts relatively evenly throughout all strain levels. Three – parameter Ogden model evaluated as the best for the application of our concern shows slight increase in suitability throughout strain levels, thus overtaking other models for both BR and NR materials. On the contrary single – parameter Ogden model shows considerable decrease in suitability leading it as the worst model for 100 % strain level.

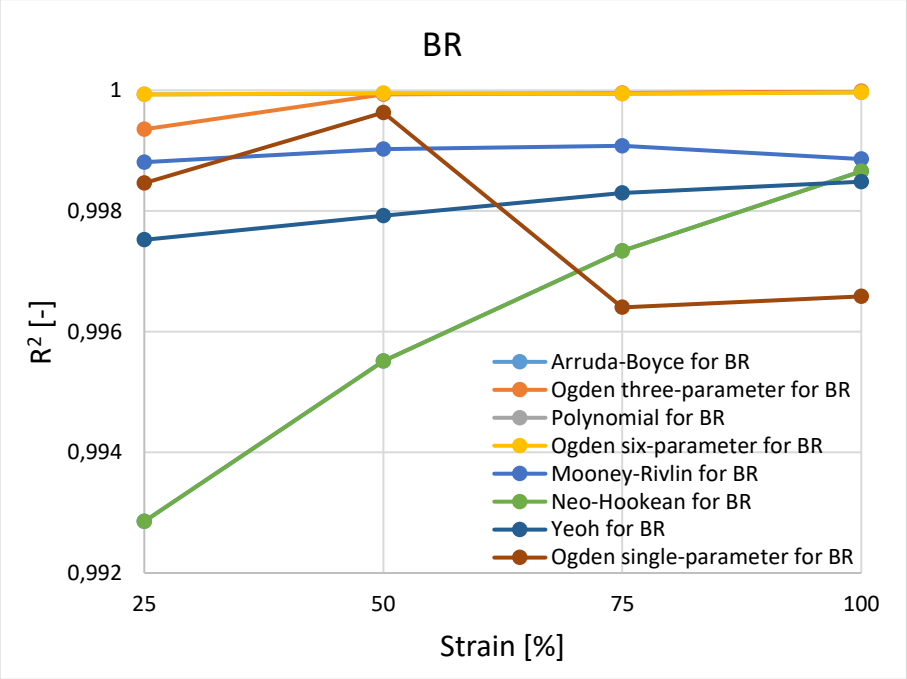

Figure 53 Hyperelastic models' fitness comparison for all deformation levels for BR

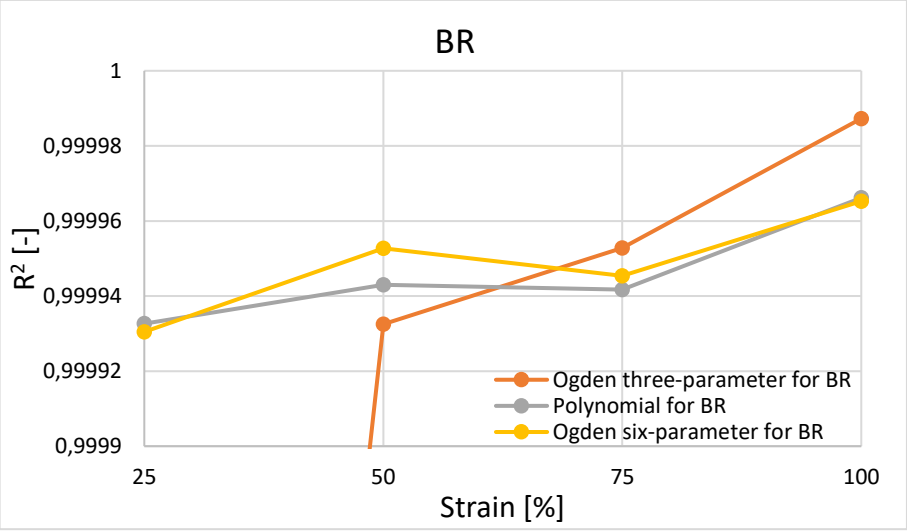

Figure 54 Fitness comparison of the best three models for all deformation levels for BR

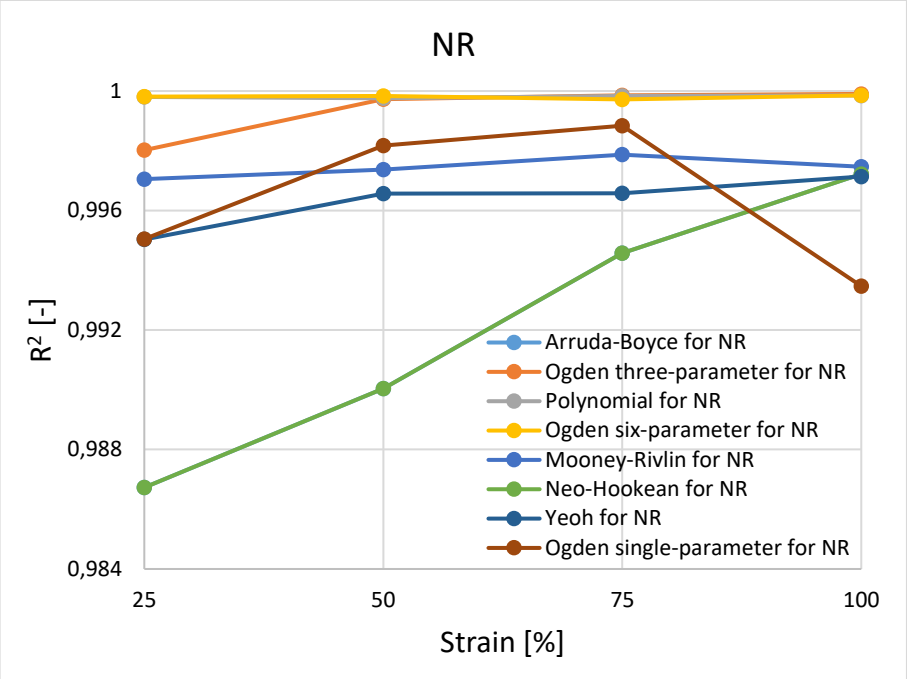

Figure 55 Hyperelastic models' fitness comparison for all deformation levels for NR

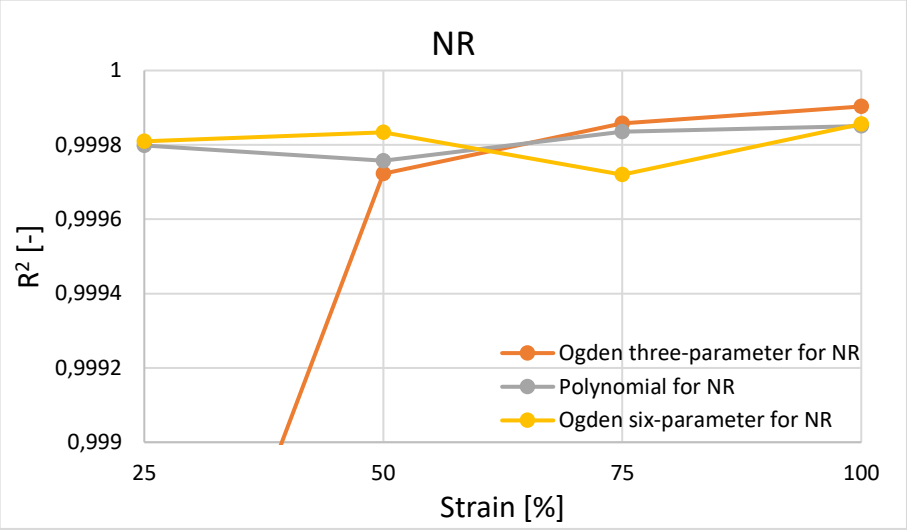

Figure 56 Fitness comparison of the best three models for all deformation levels for NR

Evaluation of experimental tensile data for hyperelastic models provided comparison of suitability according to coefficient of determination R^2 within two examined materials and four levels of strain. For both BR and NR the three – parameter Ogden model was evaluated as the most suitable for strain levels up to 100 %. Therefore, this model with its unique material constants is used for specific simulations, which are compared with DIC measurement results in the upcoming chapters.

5.2.3 Load simulation

Modelling and evaluation of load simulation of specific digital samples were carried out according to method and criteria introduced in chapter 4.3.2. Simulations were based on data and results summarized in chapters 5.1 and 5.2.1.

Each individual digital sample was based and designed according to unique dimensions of samples in unloaded state acquired by DIC measurements. However, the process of transformation of a real object to simulated environment carries with itself several error areas. These consists of dimension reading inaccuracies, samples' shape and dimensions inaccuracies, and practical measurement inaccuracies. Because of these reasons it was necessary to implement several basic conditions for simulations' unification:

- Samples' boundary dimensions were considered equal thus $L_1 = L_3$ a $L_2 = L_4$, so they would be perpendicular and parallel to each other.
- Holes on type 2 and type 3 geometries were considered as perfectly circular, and their diameter was set as an average value of horizontal and vertical dimensions.
- Holes' centres on type 3 geometry were consider equal in y axis.
- Load axis was considered as purely horizontal.

The real samples' geometries for both studied materials and three geometry types were edited according to basic condition summarized above and implemented in individual simulations. The values were then observed for transverse ε_y and lengthwise ε_x proportional strain changes to the original values. Observed strain was in full range from 0 to 100 % by 20 steps of 5 % increments. The results in the form of relative dimensional changes were written down to excel sheets, evaluated and will be presented in the final chapter together with DIC results.

5.3 Digital image correlation

Measurement of DIC analysis and subsequent evaluation of the results was carried out according to description provided in chapter 4.2, however significant inaccuracies occurred during the measurement on Instron 8871 according to the experimental setup scheme shown in the Figure 29. These inaccuracies were furthermore confirmed during the results' evaluation.

5.3.1 Measurement inaccuracies

First inaccuracy appeared due to the shape of used clamps. Their shape shown in the Figure 57 affected the true length of the sample. Basically, it made the sample's length longer than the originally desired length as shown in the Figure 58. Therefore, displacement calculated for the original length was not equal to 100 % strain.

Figure 57 Photo of clamped sample

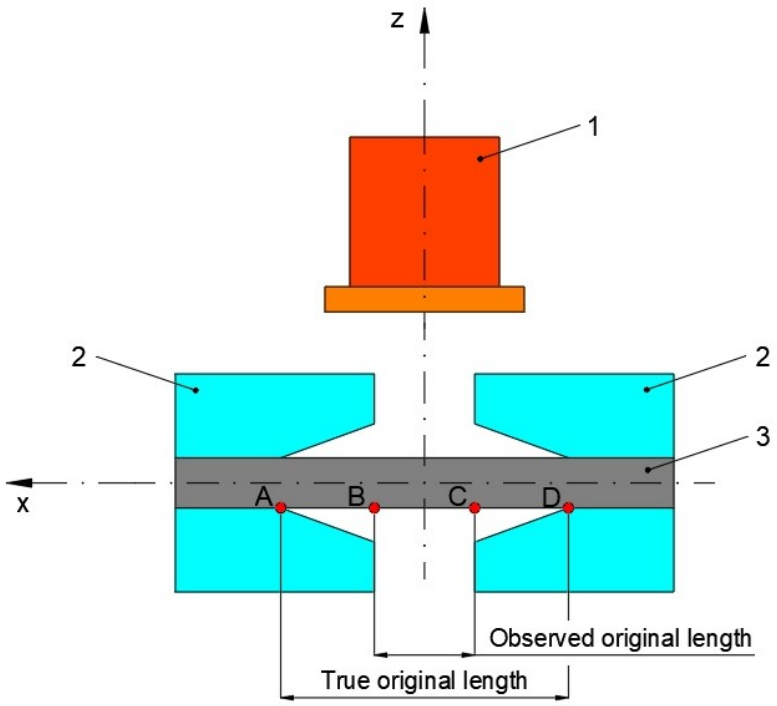

Figure 58 Scheme of clamped sample: 1 – monochrome camera, 2 – clamps, 3 – sample

Second inaccuracy affected original length of the sample even more as the clamping strength of mechanical clamps used for Instron measurement seemed insufficient and thus allowing sample to slip through the clamps as illustrated in the Figure 59.

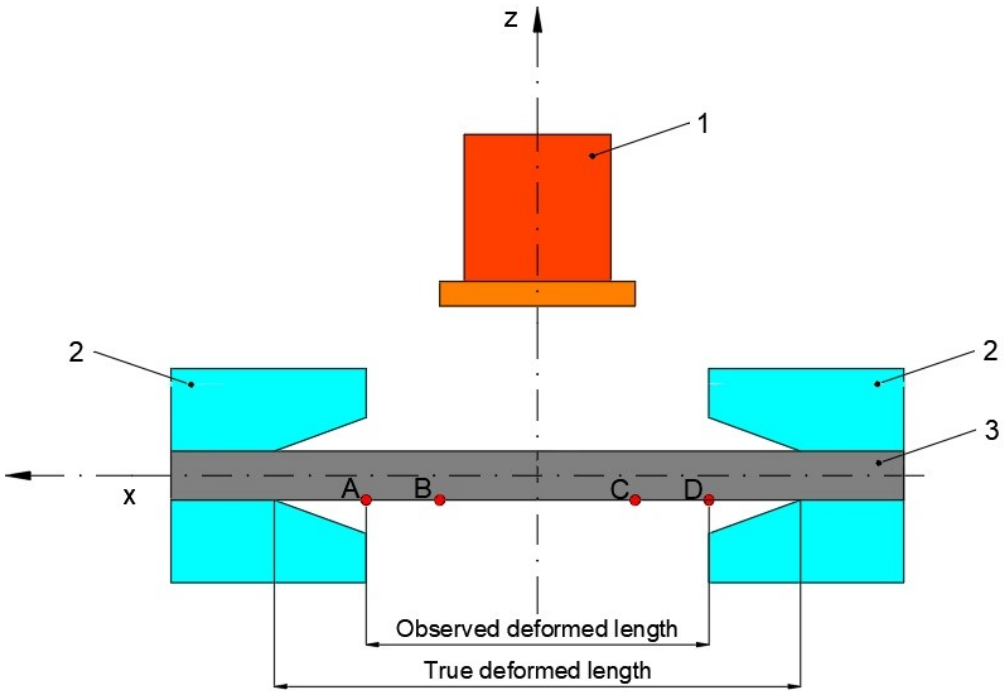

Figure 59 Scheme of clamped sample after loading process: 1 – monochrome camera, 2 – clamps, 3 – sample

These inaccuracies resulted in compromising of measured data as the samples were practically unable to reached desired levels of strain. The error can be seen in the Figure 60 where is undeformed sample (left) compared with deformed sample (right) from practical DIC measurement. The deformed sample shows displacement of outer areas which moved out of the clamps during the load process and thus are left out from examined section, defined by bordered area on undeformed sample. This undesired behaviour resulted in lower final displacements even though, the displacement of clamps was equal to 100 % to the original sample's length.

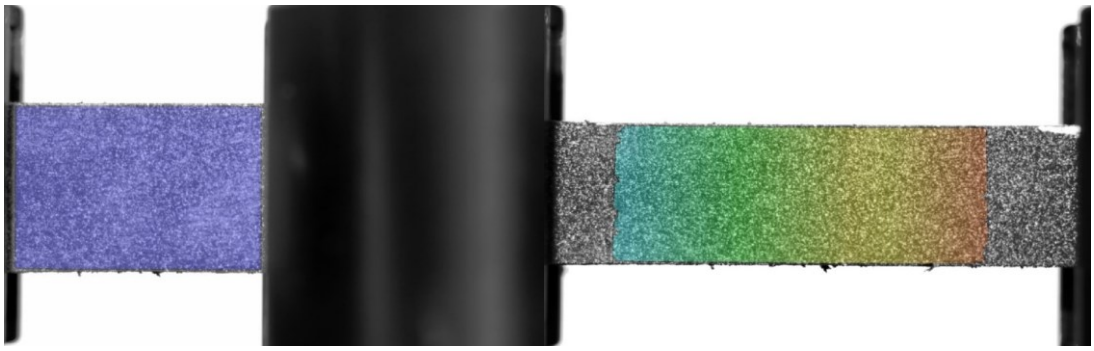

Figure 60 Undeformed sample (left); deformed sample (right)

Slipping error was partly eliminated by using sandpaper inserts between clamps and samples' surfaces, thus increasing friction. However, despite this improvement samples were still not able to reach desired deformation of 75 and 100 %.

Furthermore, additional errors as pattern density (figure 61 left), pattern flaws (figure 61 right), insufficient light source, inaccurate camera angle, surface reflections, uneven surface and thickness of sample, scratches and other surface flaws were recognized. These errors usually resulted in broken DIC mesh which could not be used for any future assessment as illustrated on the Figure 62.

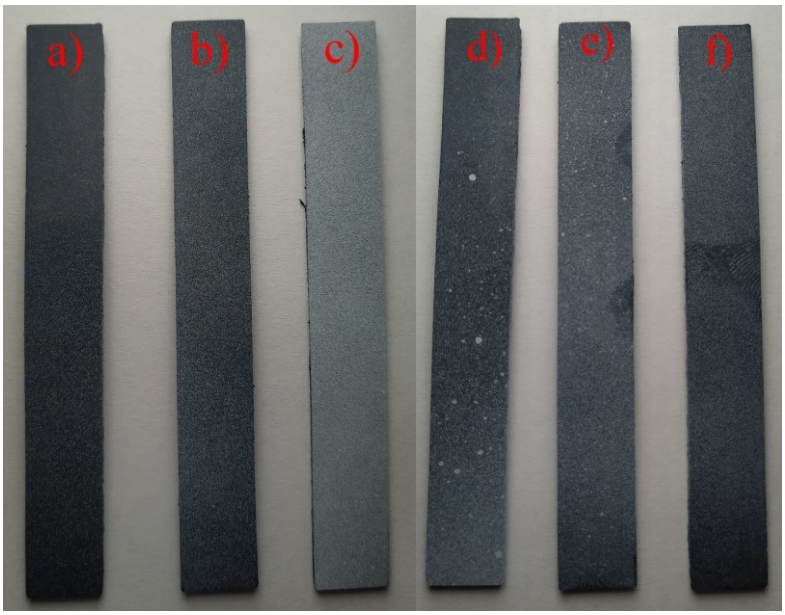

Figure 61 Pattern density (left): a) too low, b) just right, c) too high; pattern flaws (right): d) large spots and uneven pattern density, e) uneven size of spots, f) smudges in pattern

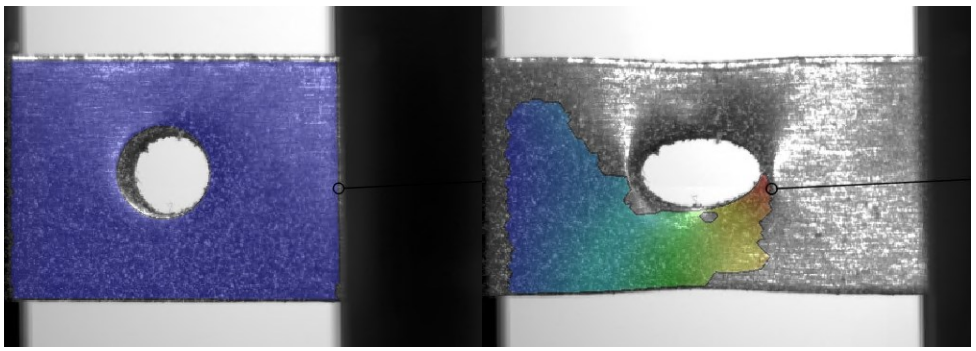

Figure 62 Example of broken DIC mesh due to surface flaws

Together with clamping errors and samples' flaws other measurement limitations were recognized:

- **Capture time** – could not exceed 40 s due to the camera's memory limit. This resulted in maximal theoretical strain around 111 % as the speed of load were set on 25 mm/min and sample length was 15 mm.
- **Camera distance** – camera position could not exceed the point from which it was no longer able to properly focus the fine pattern.
- **Shot size** – was given by the camera's frame. Shot size could be increased by moving camera further from the sample, however this resulted in focusing problems as mentioned above.

Due to this capture time – camera distance – shot size paradox the final observable deformations could not much exceed previously set strain 100 % to the original 15 mm sample length.

These circumstances led to the decision to repeat the whole practical measurement and simulations of this study, thus especially improve the DIC measurement.

5.3.2 Measurement improvements

Improved measurement was carried out on two measuring machines:

- Instron 8871 according to the experimental setup scheme shown previously in the Figure 30.
- Intrinsic Strength Analyser (Coesfeld, GmbH. Germany) - (ISA) according to the experimental setup scheme shown in the Figure 63.

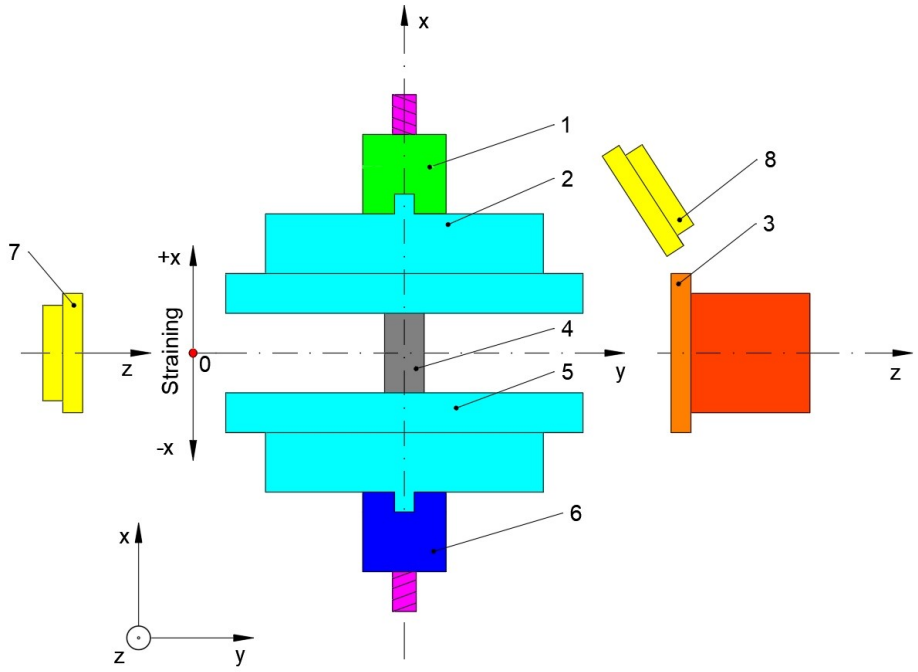

Figure 63 The scheme of ISA experimental DIC setup:
1 – loading cell in the *x* direction; 2 – upper movable clamps; 3 – monochrome camera; 4 – test sample; 5 – lower movable clamps; 6 – actuator for straining; 7 – light source; 8 – additional hand light source

Schematic illustrations of INSTRON experimental DIC setup (Figure 30) and ISA experimental DIC setup (Figure 63) shows fundamental differences in loading principles between these two measuring machines. INSTRON is based upon fixed bottom base with unmovable lower clamps and movable upper clamps, therefore the loading process is based upon unilateral strain, whereas ISA is based on both upper and lower movable clamps, thus the loading process is bilateral. This measuring process distinction results in two different boundary conditions, respectively loading principles described in Figures 64 and 65.

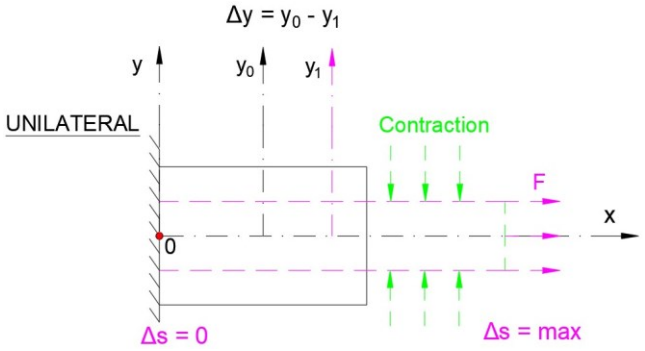

Figure 64 Unilateral loading principle

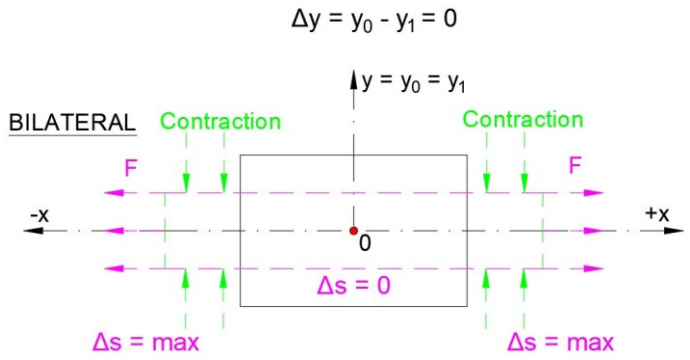

Figure 65 Bilateral loading principle

Unilateral loading principle in the Figure 64 shows movement of central y_0 axis when the sample undergoes loading. The difference between original y_0 and subsequent y_1 position is defined as $\Delta y = y_0 - y_1$.

Bilateral loading principle in the Figure 65 shows consistent position of central y_0 axis throughout the loading process, therefore $\Delta y = y_0 - y_1 = 0$.

Further measurement improvements involve changes in clamping techniques. Instead of flat clamps shown in the Figure 58, clamps with cylinder grips, illustrated in the Figure 66 were used for measurement conducted by unilateral loading. For measurement conducted by bilateral loading, clamps with cylinder grips and special ISA clamps illustrated in the Figure 67 were used.

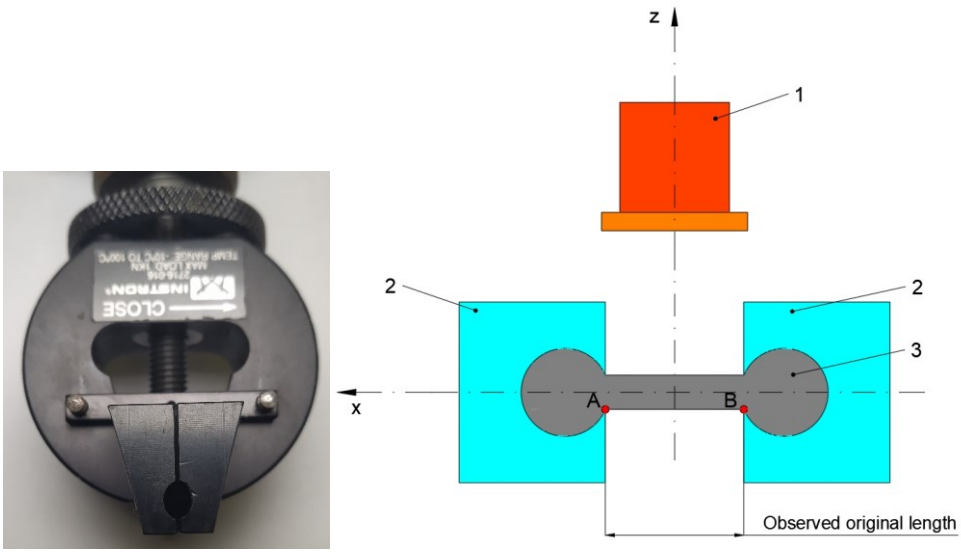

Figure 66 Picture of clamps with cylinder grips (left); scheme of clamped cylindrical sample: (right) 1 – monochrome camera, 2 – clamps with cylinder grips, 3 – sample

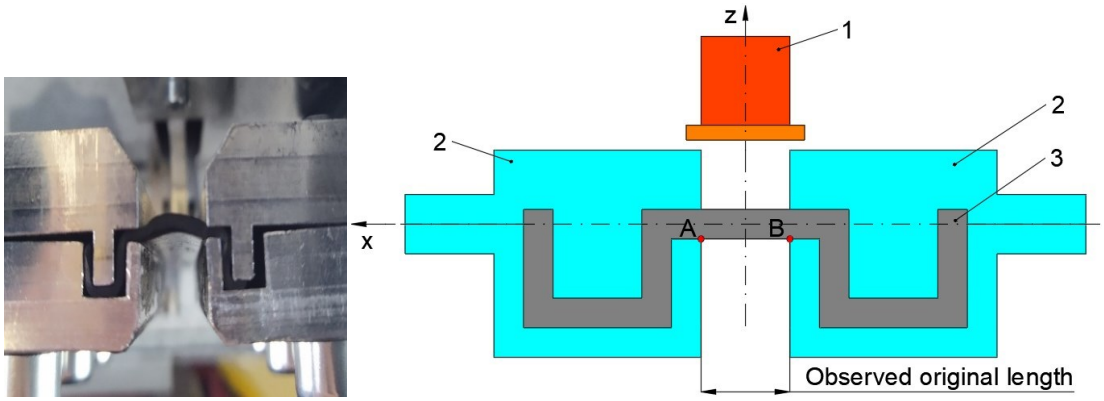

Figure 67 Picture of special ISA clamps (left); scheme of clamped flat sample: (right)
1 – monochrome camera, 2 – special ISA clamps, 3 – sample

New additional samples' geometries shown in the Figure 68 needed to be chosen for measurements using clamps with cylindrical grips. Samples' geometries for measurement using special ISA clamps remained identical to the previous geometries shown in the Figure 28.

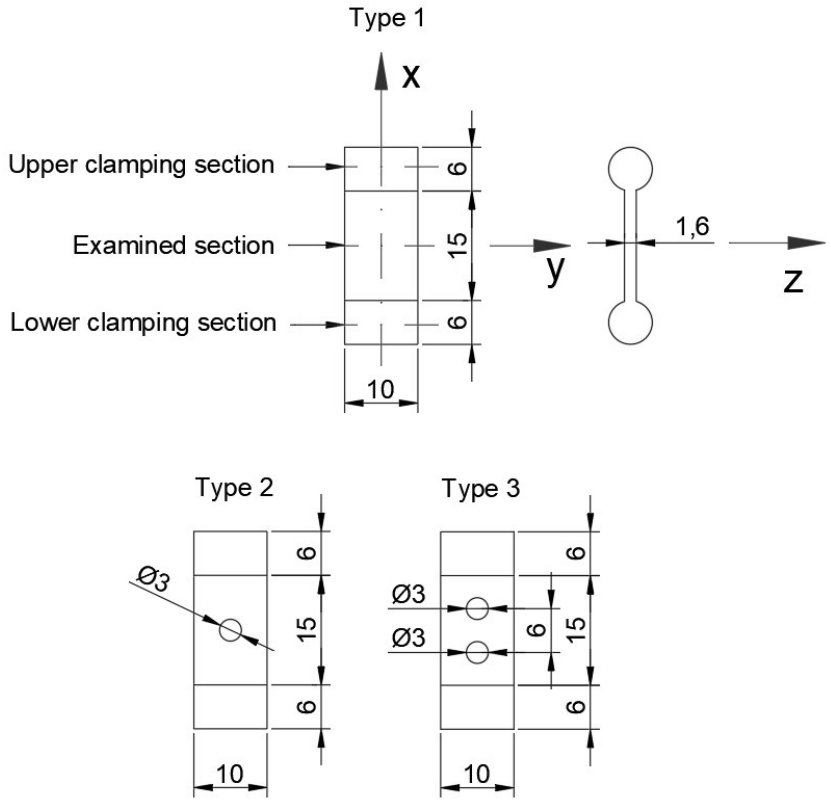

Figure 68 DIC cylinder grips sample types

Improved measurements divided by two loading principles and two clamping techniques are summarized in the Table 18 with a list of dedicated shortcuts for individual measuring techniques provided in the Table 17. From defined geometries and surface elements the true dimensions of samples' geometries in the unloaded state were recorded. These values were then during the loading process observed for transverse ε_y and lengthwise ε_x proportional strain changes to the original samples' L_2 length value, respectively changes to the original length between clamps. Results in the form of proportional changes in lengths of observed values were written down to excel sheets and evaluated for both BR and NR materials.

Table 17 Used shortcuts

Measuring technique	Unilateral - Flat samples	Bilateral - Flat samples	Unilateral - Cylindrical samples	Bilateral - Cylidrical samples
Shortcut	UNI_F	BI_F	UNI_C	BI_C

Table 18 Measurement summarization

Geometry	UNI_F	BI_F	UNI_C	BI_C	**Strain [%]**
Type 1	$\varepsilon_y - L_5$				0 – 100
Type 2	$\varepsilon_y - L_5, L_7, L_{10}, L_{11}$ $\varepsilon_x - L_6, L_8, L_9$				0 – 100
Type 3	$\varepsilon_y - L_5, L_6, L_7, L_9, L_{11}, L_{15}, L_{16}, L_{17}, L_{18}$ $\varepsilon_x - L_8, L_{10}, L_{12}, L_{13}, L_{14}$				0 – 100

Upcoming results are illustrative examples from full – scale measurement. The results are provided for the confirmation of the measurement improvements described above. Only reduced geometry type 2 is presented as the rest of the results are evaluated and presented together with FEM results in future chapter.

5.3.3 Confirmation of the measurement improvements

DIC results for both BR and NR type 2 geometry measured using four individual measurement techniques: UNI_F, BI_F, UNI_C and BI_C. Results of proportional length changes ε_x and ε_y for observed dimensions L_5, L_6 and L_7 are graphically evaluated in the Figures 70, 72 and 73.

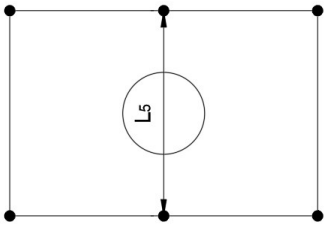

Figure 69 Observed dimension L_5 for geometry Type 2

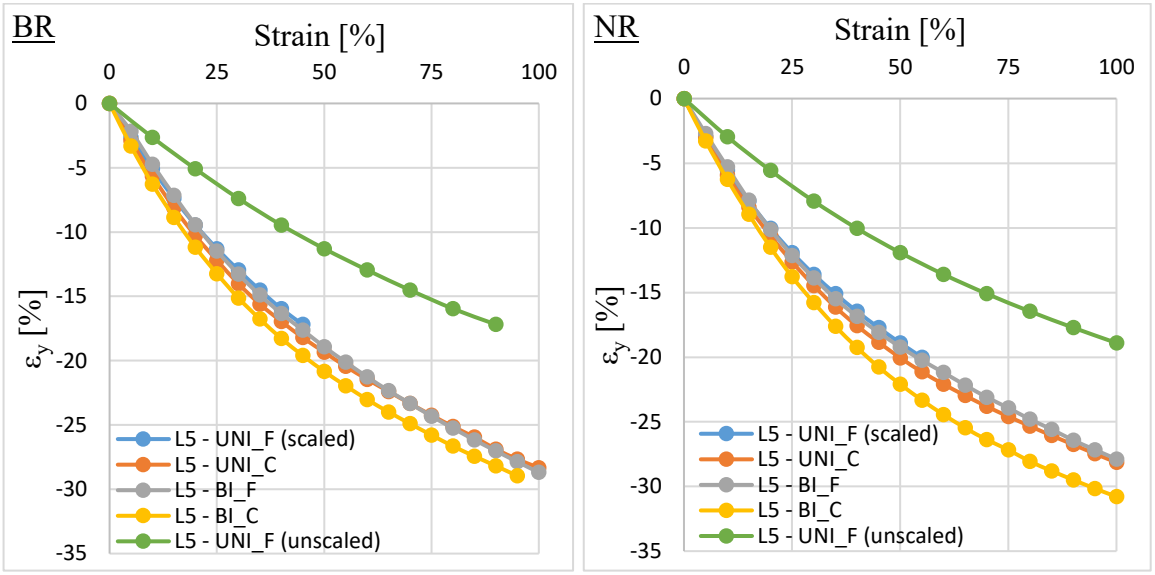

Figure 70 Graphical comparison of ε_y DIC results for BR (left) and NR (right) – Type 2 geometry – L_5

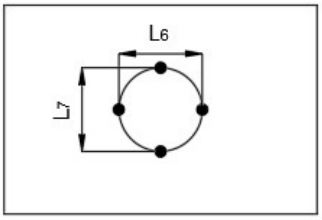

Figure 71 Observed dimensions L_6 and L_7 for geometry Type 2

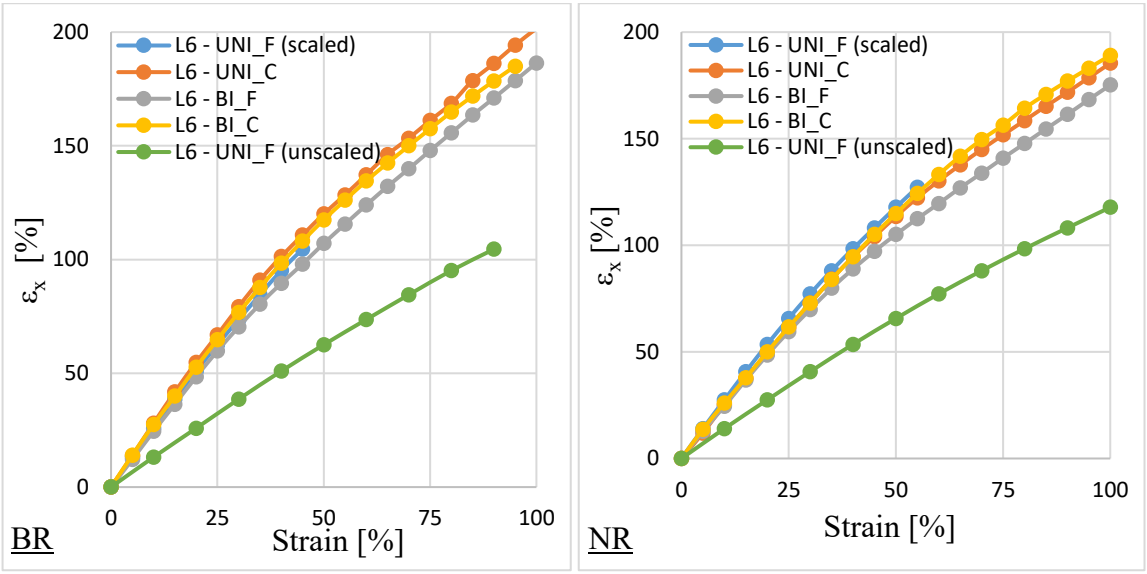

Figure 72 Graphical comparison of ε_x DIC results for BR (left) and NR (right) – Type 2 geometry – L_6

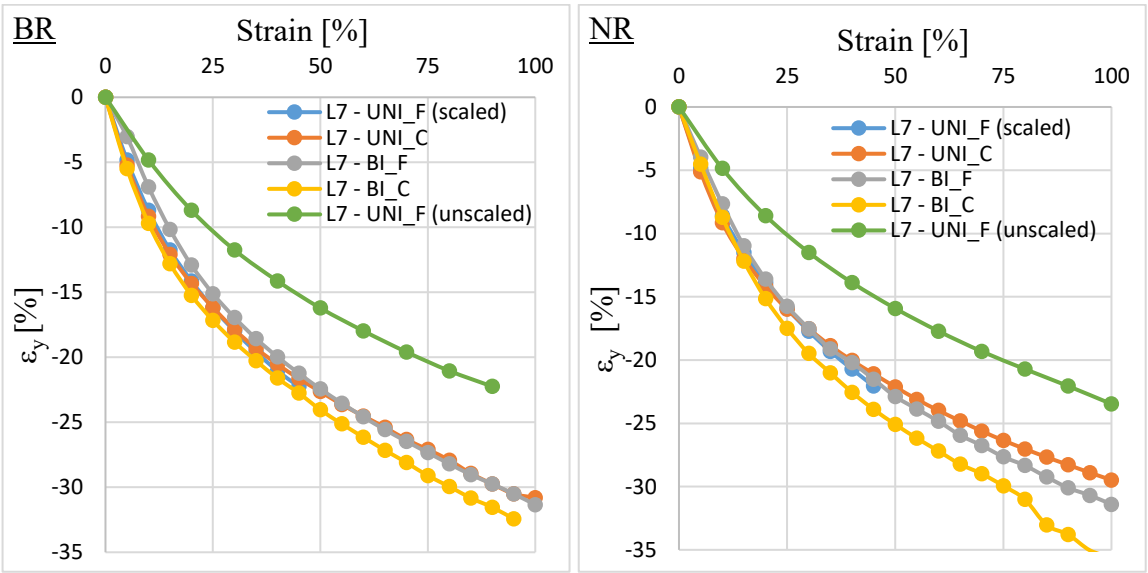

Figure 73 Graphical comparison of ε_y DIC results for BR (left) and NR (right) – Type 2 geometry – L_7

Results represented in the Figures above show efficiency of the improvements set in the previous chapter. Original measurement technique without the improvements is represented by green curves UNI_F (unscaled). These show smaller changes in ε_x and ε_y values compared to the improved techniques. However, once we scale the UNI_F (scaled) not by the clamps displacement but by true L_2 strain, we obtain nearly identical results with the other techniques. This proves ability of DIC measurement to obtain correct values not against a fixed displacement value of clamps, but by true strain of the pattern itself. The Figure 74 shows practical comparison between stages of maximal clamps displacement for individual measurement techniques. Sample BI_F seems to be the most stable one, as unwanted strains and slipping on the sides of the sample are lowest compared to other techniques. However, it needs to be stated, that the visual comparison is highly dependent on the original DIC mesh definition in unloaded state, which is not identical for each sample and thus may affect the final visual results.

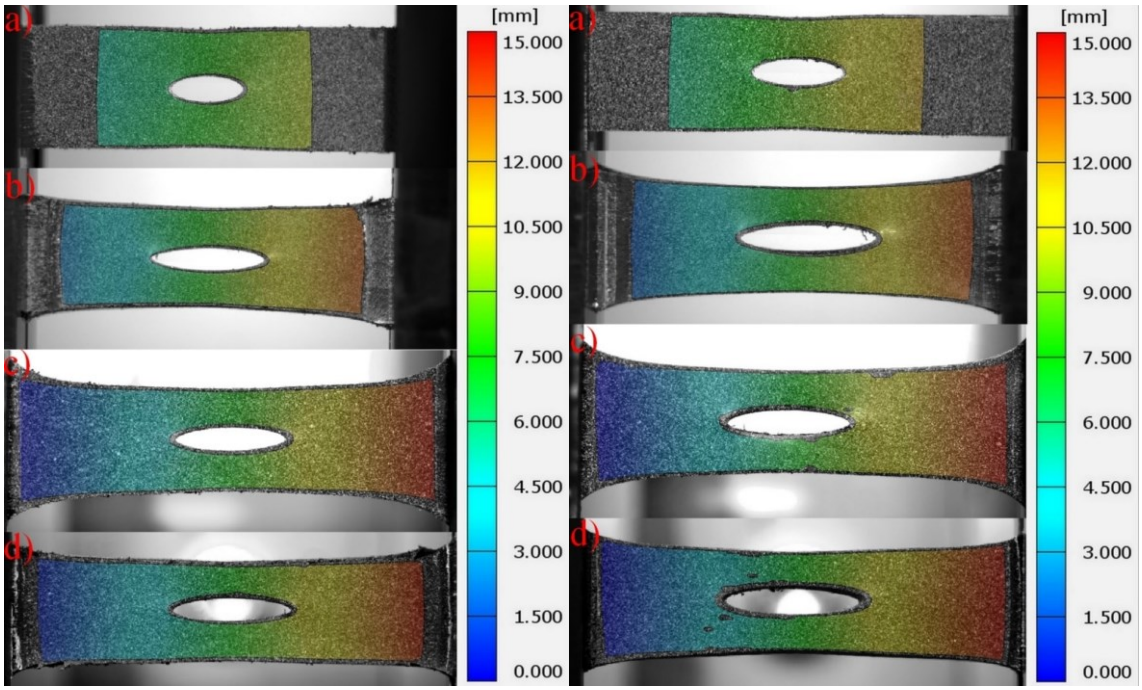

Figure 74 Visual comparison of BR (left) and NR (right) Type 2 samples in maximal clamps displacement stages: a) UNI_F, b) UNI_C, c) BI_F, d) BI_C

Even though the improvements to the DIC measurements proved to be effective to certain degree, due to the rubber hyperelastic behaviour the resulting transverse ε_y and lengthwise ε_x proportional changes could still not be compared against fixed displacement of the clamps,

thus only L_2 true strain values unique for each individual sample were used as a reference stage for observed values of proportional changes in lengths as shown in the Figure 75.

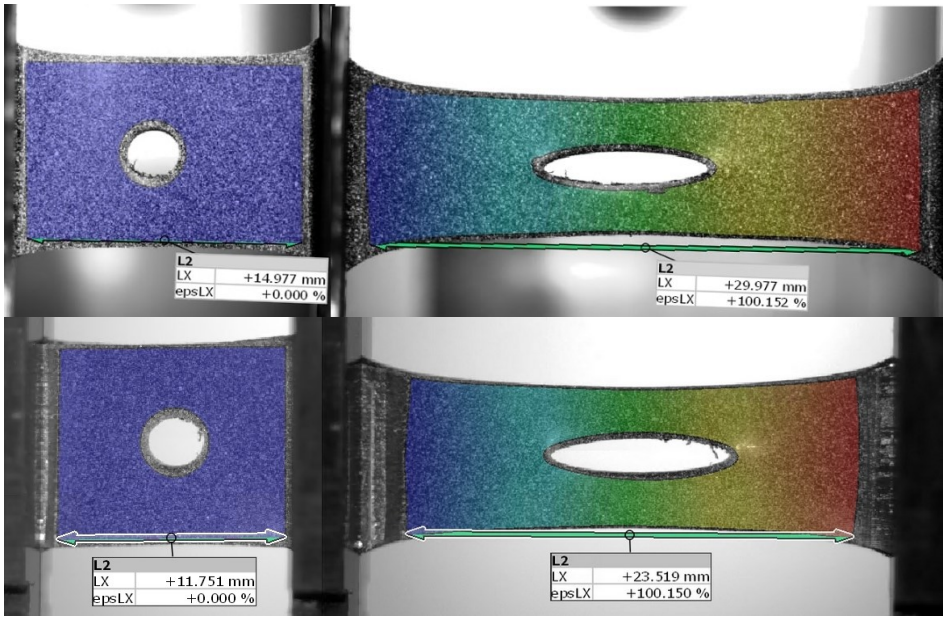

Figure 75 Comparison between two different clamps displacement with equal maximal strains of the samples

All DIC data of transverse ε_y and lengthwise ε_x proportional strain changes according to the four measurement techniques, three geometry types and both BR and NR materials were together with individual tensile data stored for future assessment and comparison with specific ABAQUS predictions.

5.3.4 Comparison of unilateral and bilateral measuring principles

In this chapter the assessment and comparison of DIC results of unilateral (UNI_C) and bilateral (BI_C) measuring principles is provided. Comparison is based on type 3 geometry which is examined for differences in sample behaviour in upper and lower clamping area. Goal of this comparison is to investigate if the individual measuring principles illustrated in the Figures 64 and 65 have any significant impact on the results within individual samples. To obtain reliable results, two transverse L_6 and L_7 and two lengthwise L_{12} and L_{14} dimensions are compared between each other for both BR and NR materials. L_6 is compared to L_7 and L_{12} to L_{14}.

Comparison of UNI_C and BI_C DIC results based on type 3 geometry for both BR and NR. Results of proportional length changes ε_x and ε_y for observed dimensions L_6, L_7, L_{12} and L_{14} are graphically evaluated in the Figures 77 and 79.

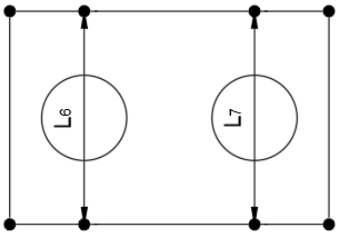

Figure 76 Observed dimensions L_6 and L_7 for geometry Type 3

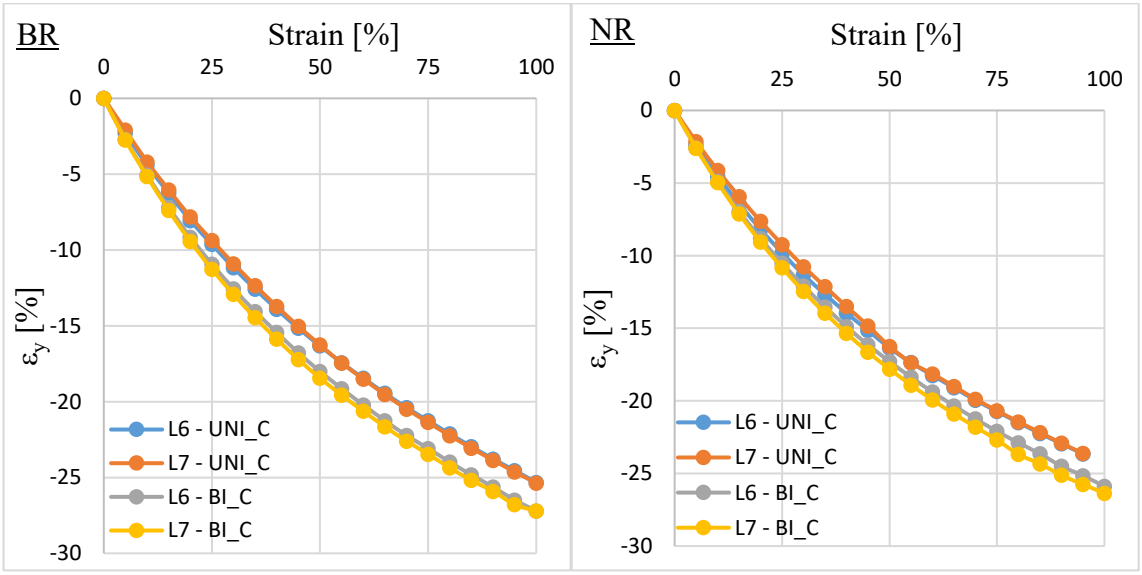

Figure 77 Graphical comparison of ε_y between L_6 and L_7 for UNI_C and BI_C measuring techniques – Geometry Type 3

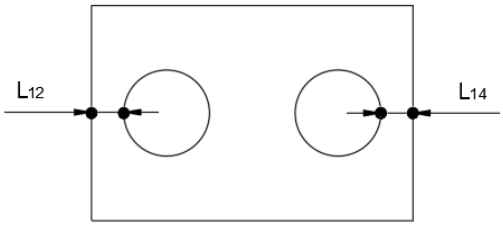

Figure 78 Observed dimensions L_{12} and L_{14} for geometry Type 3

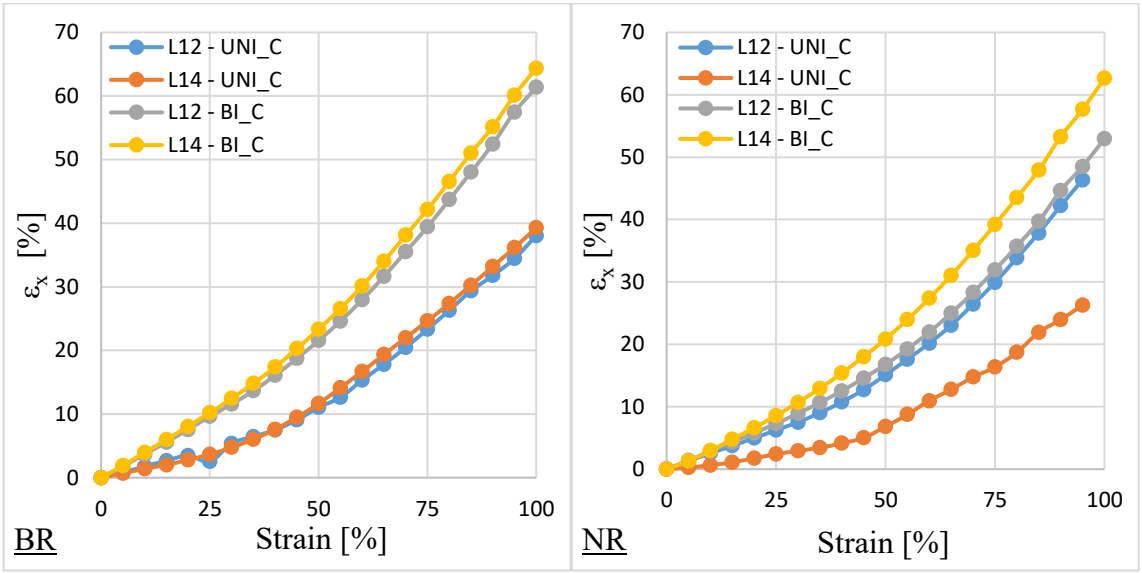

Figure 79 Graphical comparison of ε_x between L_{12} and L_{14} for UNI_C and BI_C measuring techniques – Geometry Type 3

For BR, samples' comparison of L_6 to L_7 as well as L_{12} to L_{14} showed no significant differences in samples' behaviour for both UNI_C and BI_C measuring techniques.
In the case of NR, comparison of L_6 to L_7 showed also no significant differences in samples' behaviour for both UNI_C and BI_C measuring techniques. However, in the case of L_{12} and L_{14} comparison, results showed increase in ε_x differences. These were more significant for UNI_C measuring technique then for BI_C. Nevertheless, if we consider results for both BR and NR, the comparison between L_{12} and L_{14} for NR could have been caused by practical measurement inaccuracies as the rest of the results follow similar trends with no significant differences.

Overall, comparison of L_6 to L_7 dimension and L_{12} to L_{14} dimension proved no significant differences in samples' behaviour between unilateral and bilateral measuring techniques. Thus, in the scope of this theses, these differences can be considered insignificant.

5.4 FEM and DIC comparison

This last chapter consists of the final assessment and comparison between DIC measurements' results and FEM simulations.

Comparison is carried out for both BR and NR materials by different geometry types and three measurement techniques: UNI_C, BI_F and BI_C. Each geometry type is divided into three groups: outer dimensions, inner dimensions, and hole dimensions for type 2 and type 3.

And finally, at the end of dimensional comparison of each geometry type, a comparison of stress – strain behaviour acquired from practical measurements and simulations is presented. In this assessment main focus is placed upon comparison of the original stress – strain values, stress – strain values acquired by simulations, and finally stress – strain values based on real samples' behaviour obtained by DIC evaluation.

The stress – strain behaviour comparison is divided into graphical comparison, comparison by coefficients of determination R^2 according to the equation (25) and comparison by curves' slope m which is calculated from equation (26):

$$m = \left|1 - \frac{(y_2 - y_1)}{(x_2 - x_1)}\right| \tag{26}$$

Where: $(x_1;x_2)$ is point of the origin of a curve and $(y_1;y_2)$ is end point of compared curve.

For both dimensional and stress – strain comparison the UNI_F data are left out as it did not fulfil basic condition of maximal 100 % strain, thus it is not possible to reliably compare it with the rest of data.

5.4.1 Type 1 geometry

Comparison of FEM simulations' results and DIC measurements' results for both BR and NR type 1 geometry.

Outer dimensions deformation

Change in the main transverse dimension L_5 was observed for type 1 geometry. Due to implementation of basic conditions set in chapter 5.2.3 and chosen boundary conditions set in chapter 4.3.2 we can assume sample's as $L_1 = L_3 = L_5$. L_2 and L_4 strains are then equal to the main deformation value.

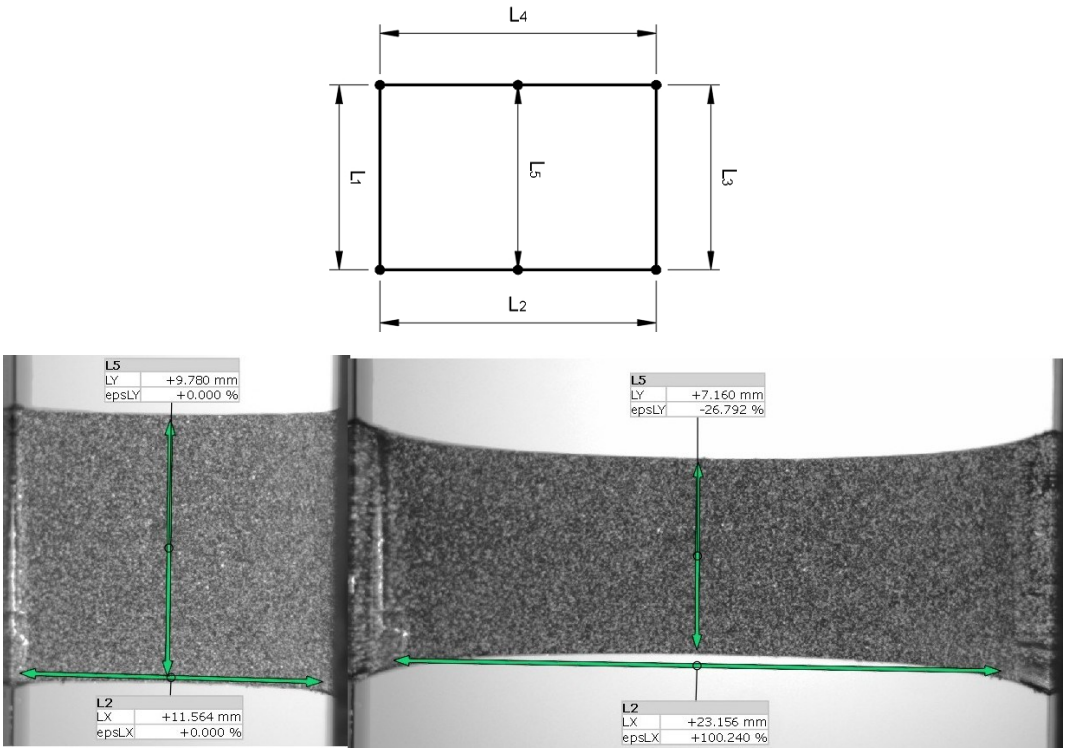

Figure 80 Outer dimensions for geometry type 1

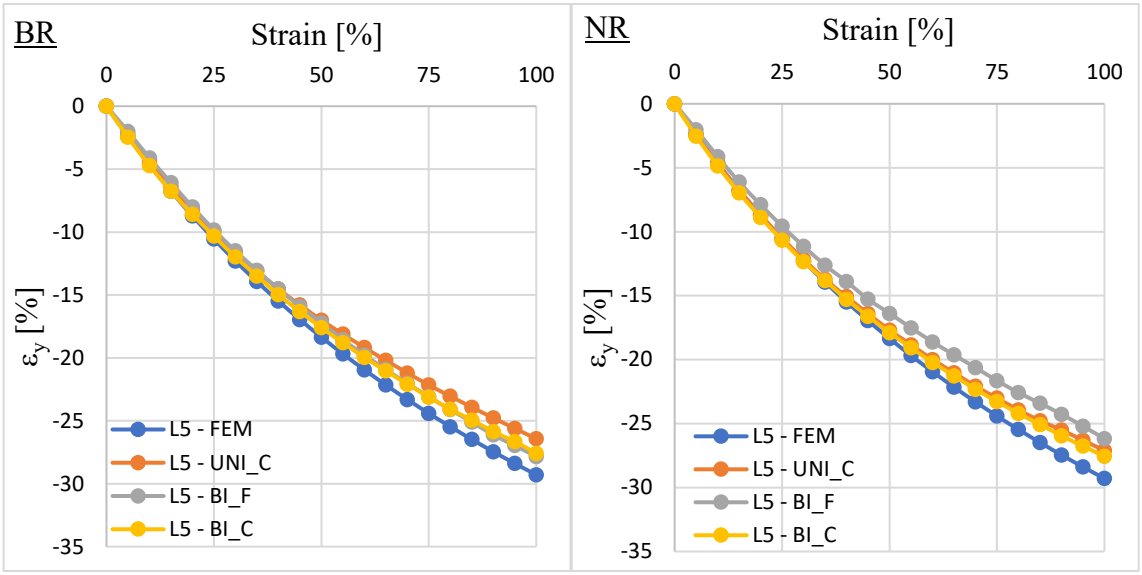

Figure 81 Graphical comparison between FEM and DIC results for BR and NR – Type 1 geometry – L_5

Comparison shows similar trends of ε_y contraction for both BR and NR samples under the full range of deformation. Values among individual measuring techniques starts to slightly differ under larger strains. However, these differences are in low percent units thus, considering possible practical measurement inaccuracies and overall simplifications, these differences can be considered within acceptable range.

Stress – strain curves comparison

The Figures 82 and 83 shows individual BR and NR comparison between 7 resulting stress – strain data sets. First set is the FEM stress – strain prediction to which stress – strain data of the individual measurement techniques are compared to. These consists of original UNI_C, BI_F and BI_C stress data sets and their equivalents evaluated and edited according to values of sample's transverse contraction ε_y. DIC data sets are thus dependent on the instantaneous sample's cross – section during loading.

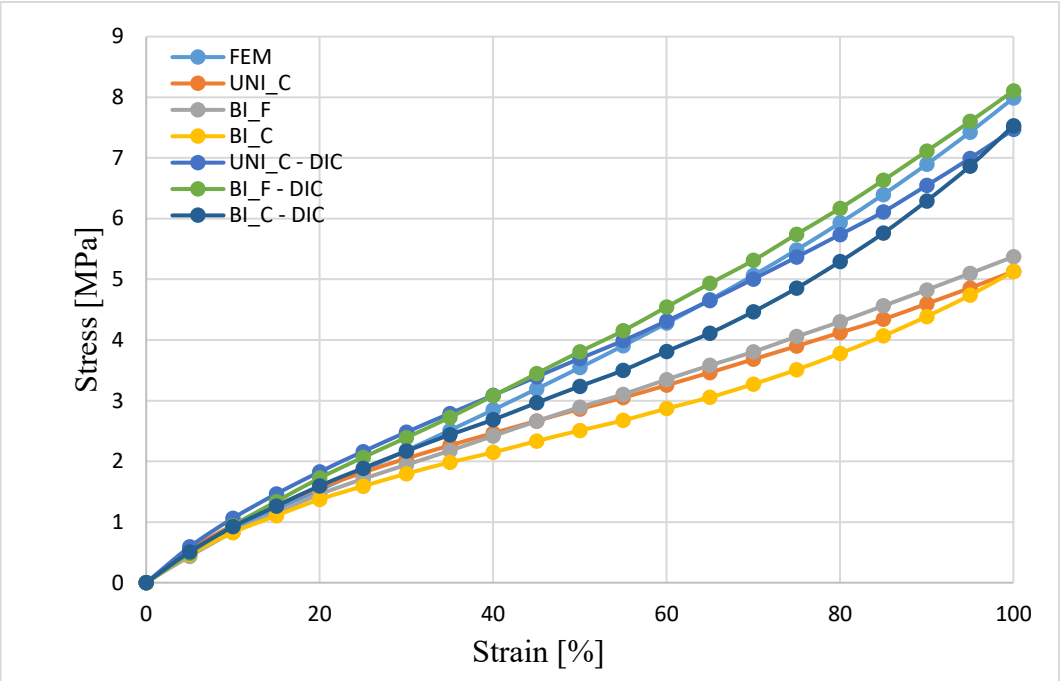

Figure 82 Comparison of stress – strain curves for BR type 1

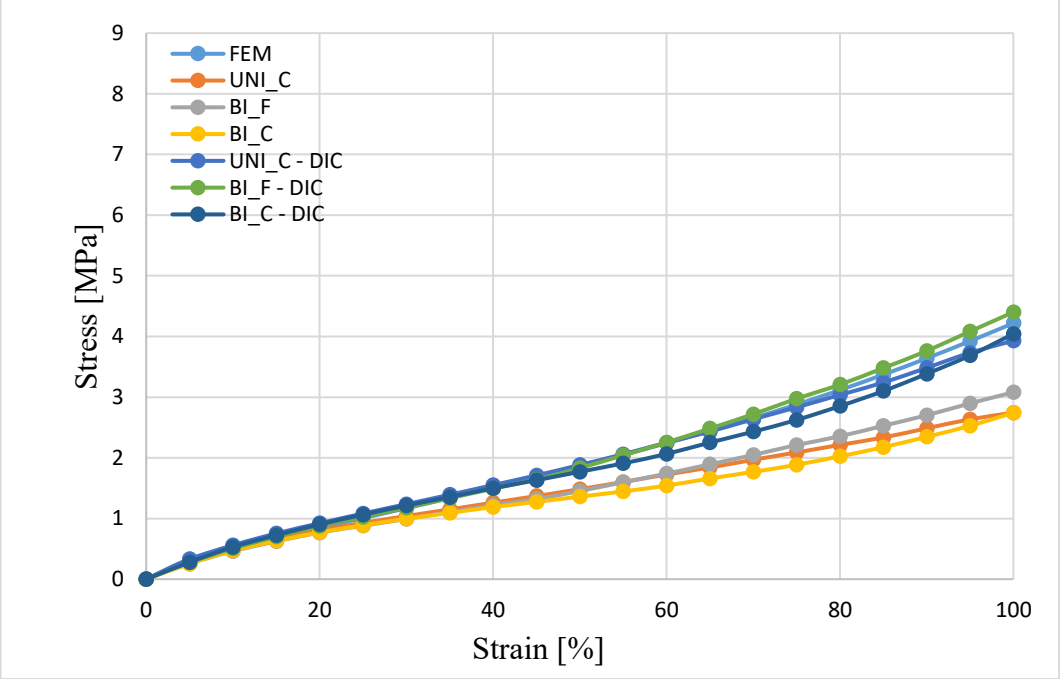

Figure 83 Comparison of stress – strain curves for NR type 1

Comparisons of stress – strain curves for BR type 1 presented in the Figure 82 and for NR type 1 presented in the Figure 83 show considerably significant improvements to the original stress – strain data when implementing DIC instantaneous sample's cross – section dependence. Stress – strain data without the implementation show high differences to the

FEM predictions, whereas DIC data show high trends' resemblance. The differences of values under the maximal strain level reached up to 3 MPa for BR and up to 1,5 MPa for NR.

These results are supported by the Figures 84 and 85 on which R^2 and m values comparisons between individual measuring techniques to the FEM predictions are showed.

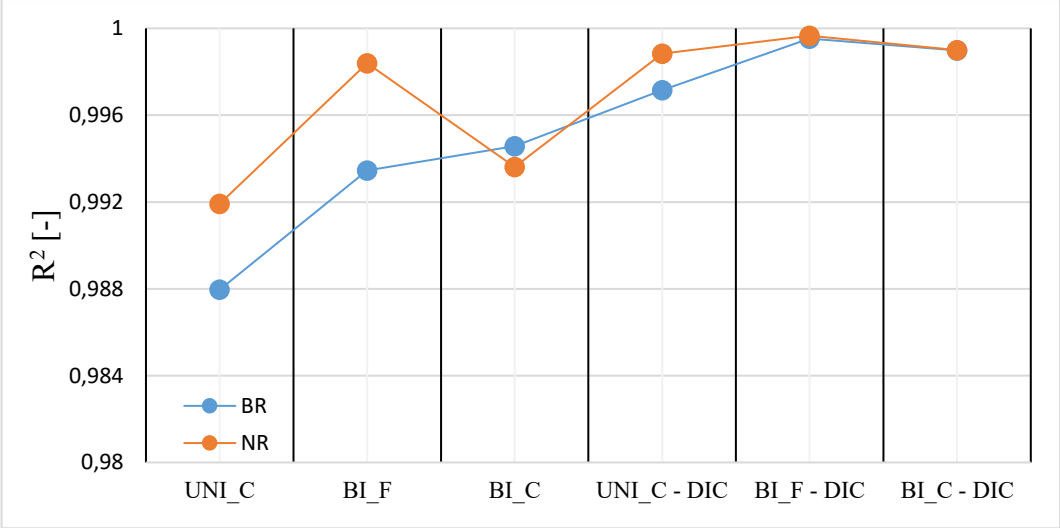

Figure 84 Comparison of R^2 values for BR and NR type 1 geometry stress – strain trends

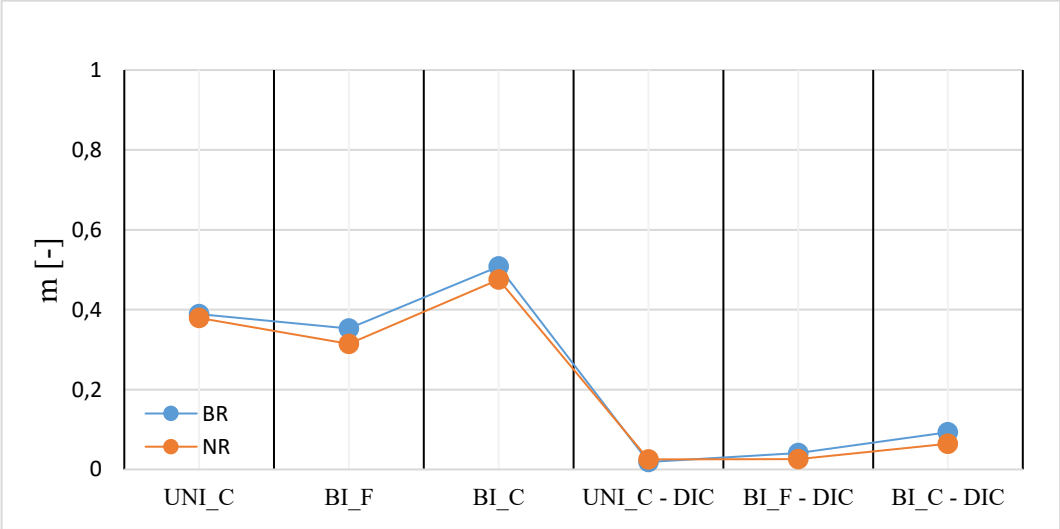

Figure 85 Comparison of m values for BR and NR type 1 geometry stress – strain trends

Figures 84 and 85 show high improvements in both R^2 and m values for DIC stress – strain data. Data for both BR and NR follow similar results with BI_F having the highest R^2 thus showing the highest correlation with FEM predictions and UNI_C is showing the best curves slope resemblance with FEM predictions.

5.4.2 Type 2 geometry

Comparison of FEM simulations' results and DIC measurements' results for both BR and NR type 2 geometry.

Outer dimensions deformation

Change in the transverse dimensions L_5 and L_1 were observed for type 2 geometry under chosen condition $L_1 = L_3$. L_2 and L_4 strains are then equal to the main deformation value.

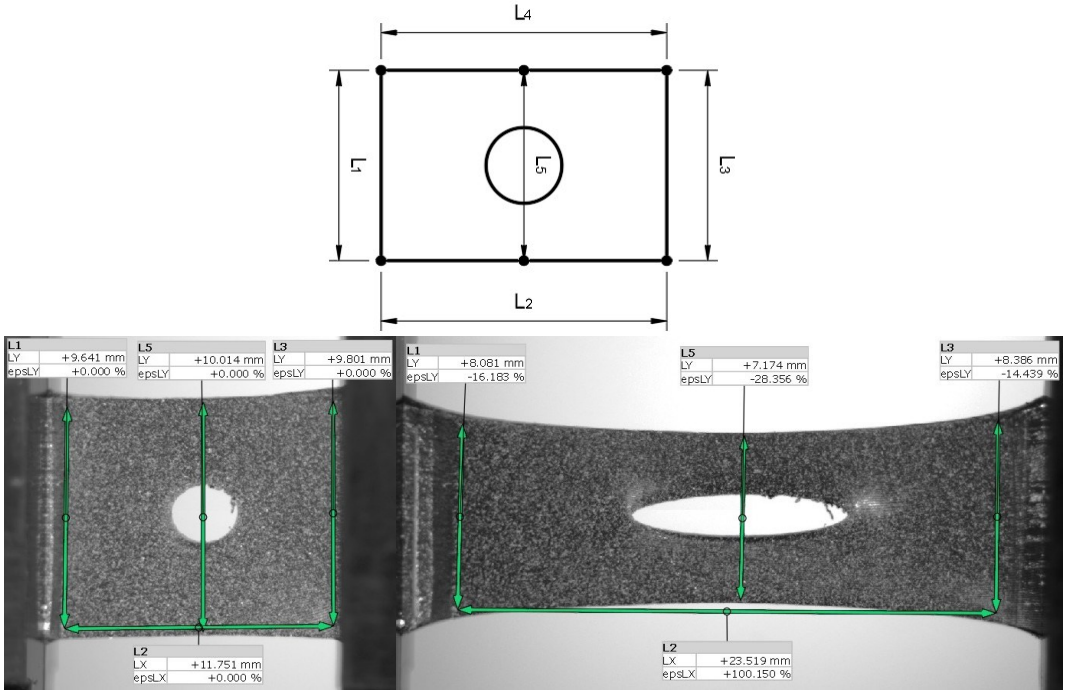

Figure 86 Outer dimensions for geometry type 2

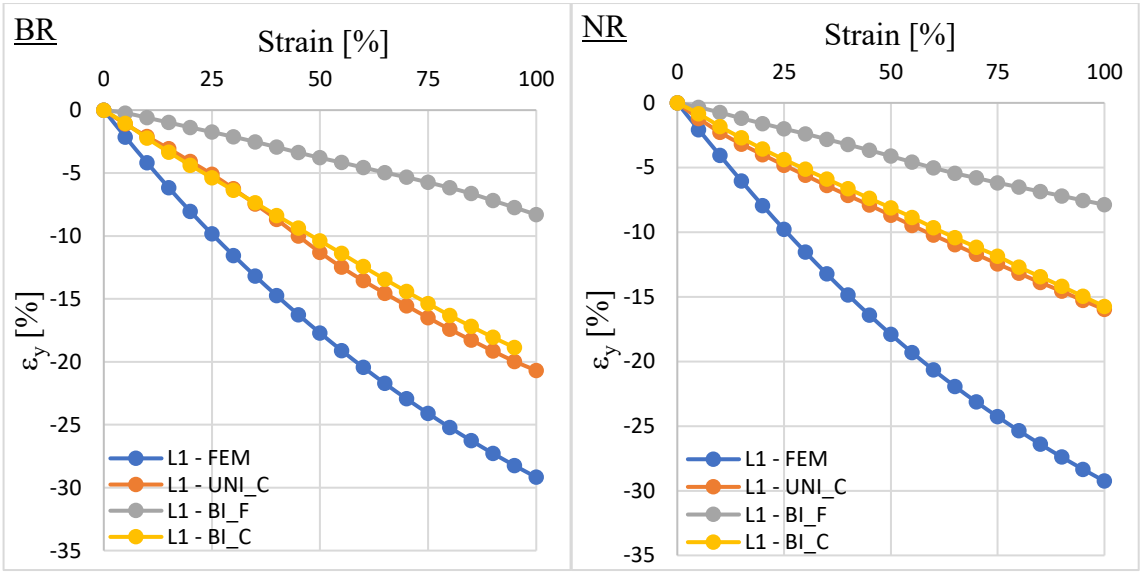

Figure 87 Graphical comparison between FEM and DIC results for BR and NR – Type 2 geometry – L_1

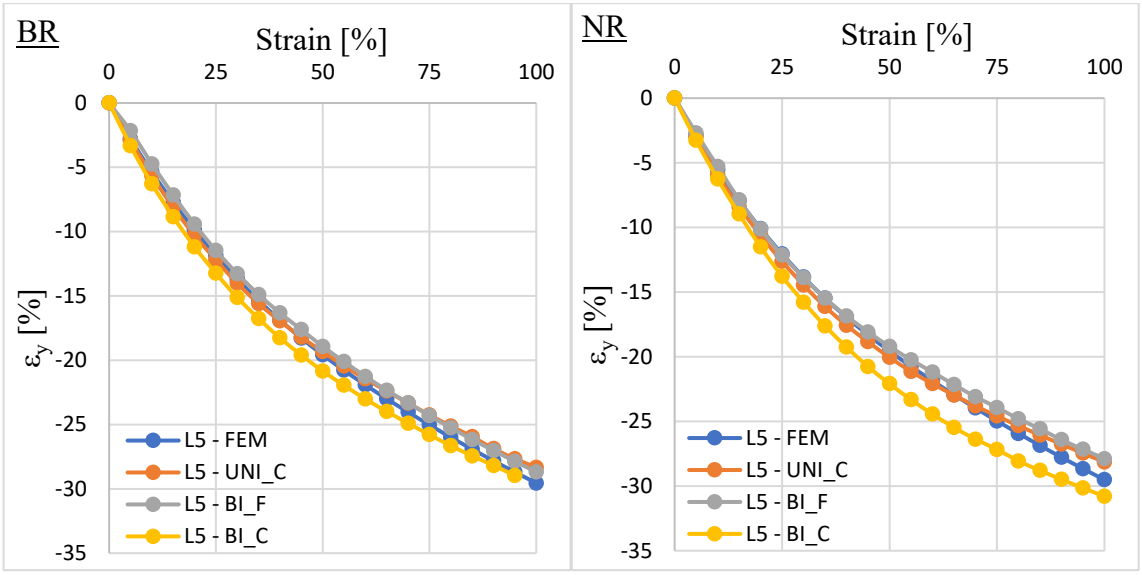

Figure 88 Graphical comparison between FEM and DIC results for BR and NR – Type 2 geometry – L_5

Comparison of L_5 for both BR and NR show similar ε_y contraction trends as in the case of type 1. Both BR and NR seem to hold constant value differences to the FEM predictions throughout the loading process. This would be considered improvement to the type 1 where values differences increased together with increasing loading. Differences within measuring techniques show slight improvements in the case of BR and slight deterioration in the case of NR. This difference could suggest higher BR samples' stability during loading.

However, comparison of L_1 shows considerable fluctuations in ε_y value among individual measuring techniques. The fluctuations apply to both BR and NR.

These high differences were identified as errors caused by samples' clamping and DIC surface area definition. As illustrated in the Figure 89 L_1 and L_3 values were unable to deform properly due to the clamping forces.

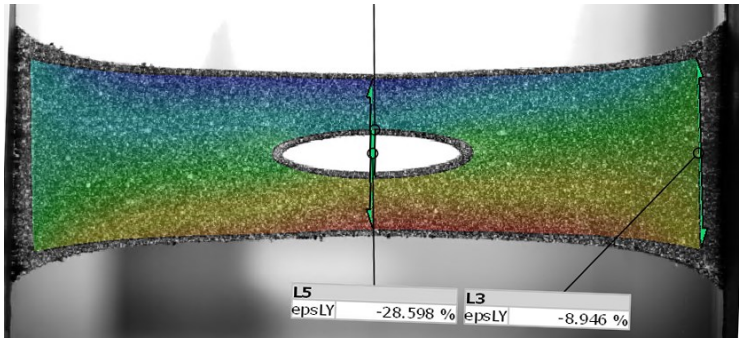

Figure 89 BI_F BR type 2 clamping error

This error could be in this particular case resolved by DIC surface area definition outside of the clamping force influence or by using longer samples which could be measured completely outside of the clamping force influence.

Hole deformations

Comparison of changes in lengthwise dimension L_6 and transverse dimension L_7 for type 2 geometry.

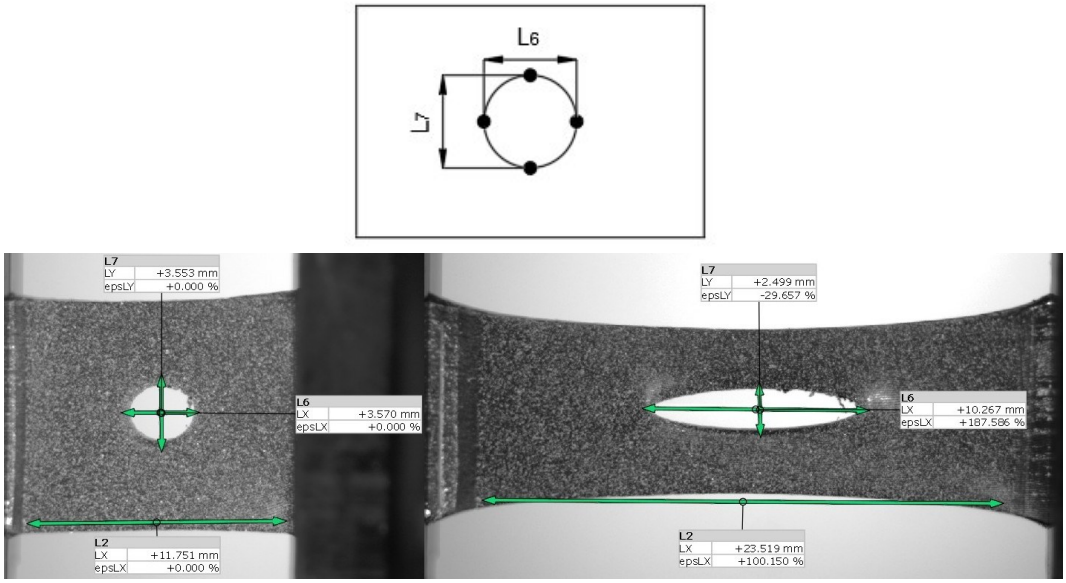

Figure 90 Groove dimensions for geometry type 2

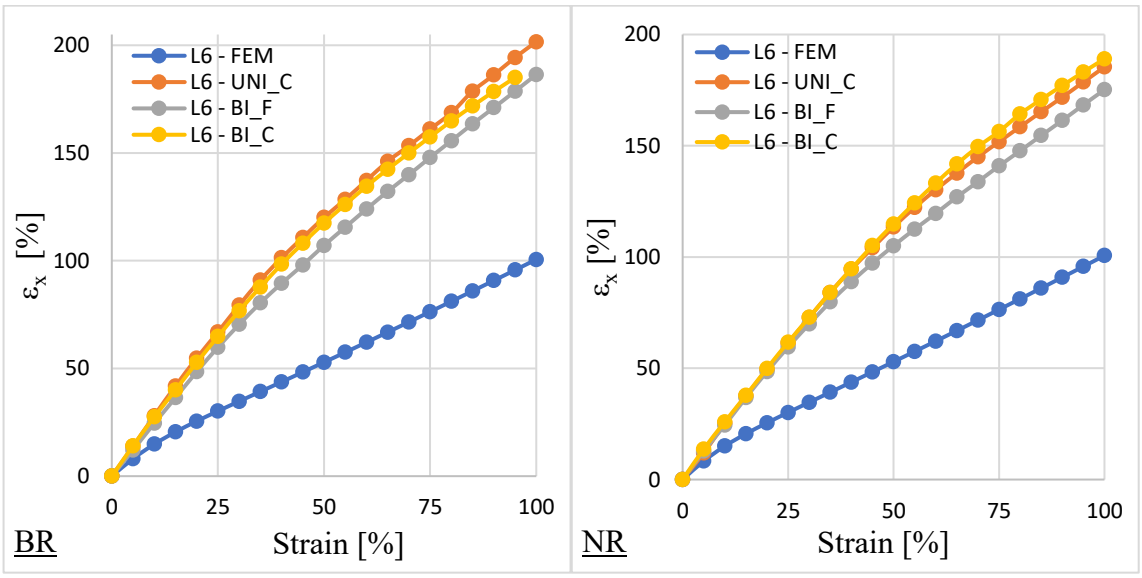

Figure 91 Graphical comparison between FEM and DIC results for BR and NR – Type 2 geometry – L_6

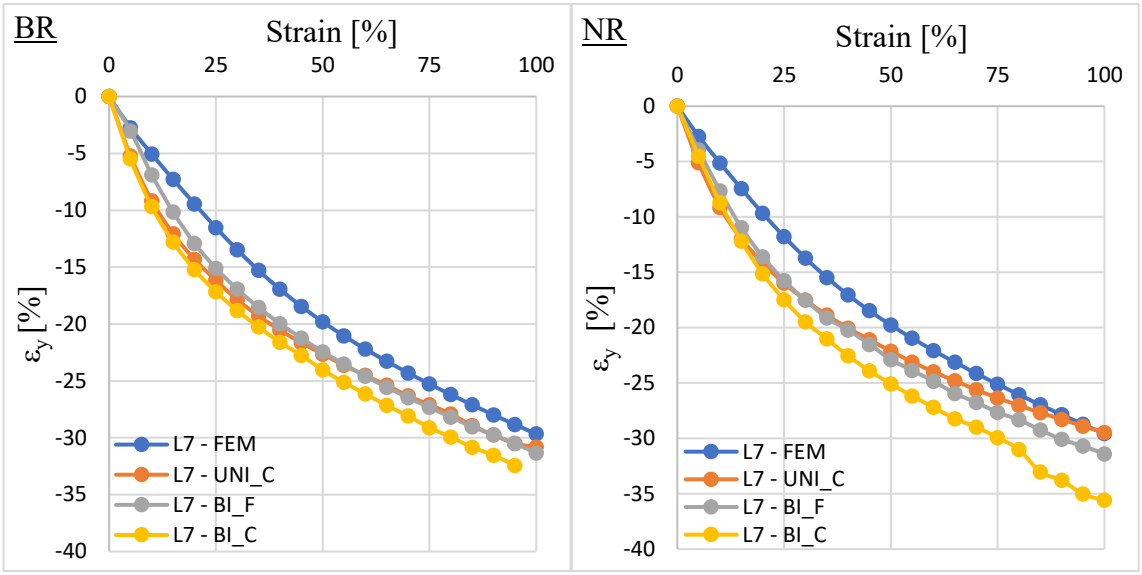

Figure 92 Graphical comparison between FEM and DIC results for BR and NR – Type 2 geometry – L_7

Comparison of L_6 for both BR and NR demonstrate first substantial distinction of obtained DIC data to the FEM predictions. Differences in ε_x for L_6 reaches for both materials almost up to 100 %. As the individual measuring techniques follows nearly similar trend no major clamping influence as in the case of L_1 is assumed.

The figure 92 then shows increase in ε_y values differences for L_7. Trends tend to differ during small strain levels from 5 to 30 % where differences in ε_y values emerge. However, with increase in the main strain, trends start to slowly balance. No significant variations among trends were observed apart from end values of the BI_C curve. However, the lack of smoothness among individual ending points of the BI_C curve can be attributed to DIC readings inaccuracies than to the material behaviour.

Inner dimensions deformation

Comparison of changes in lengthwise dimension L_8 and transverse dimension L_{10} for type 2 geometry.

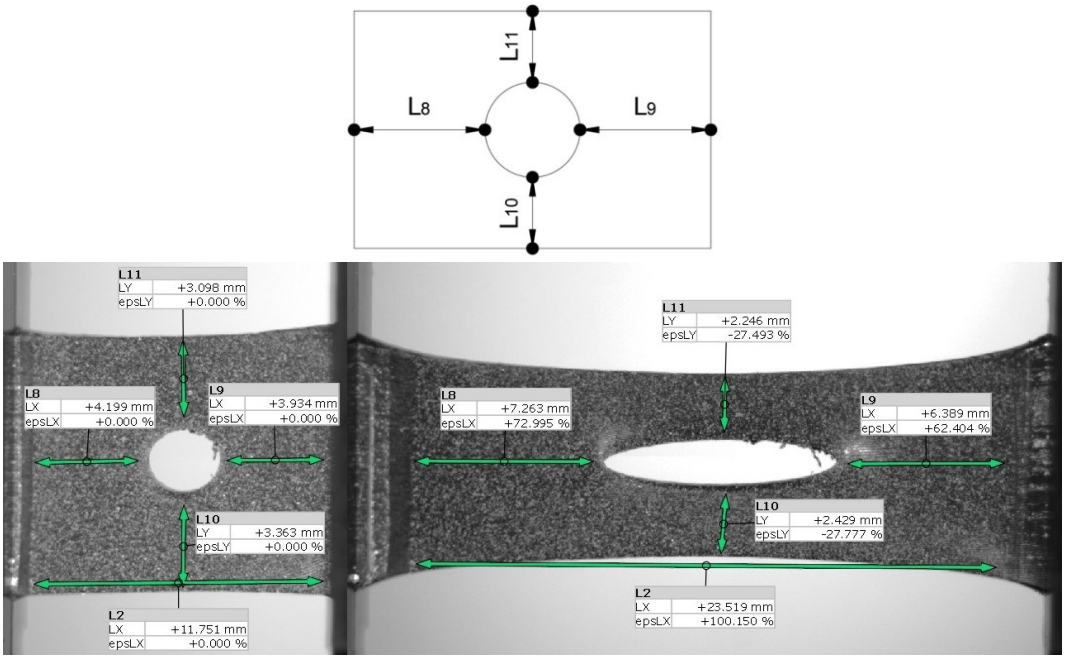

Figure 93 Inner dimensions for geometry type 2

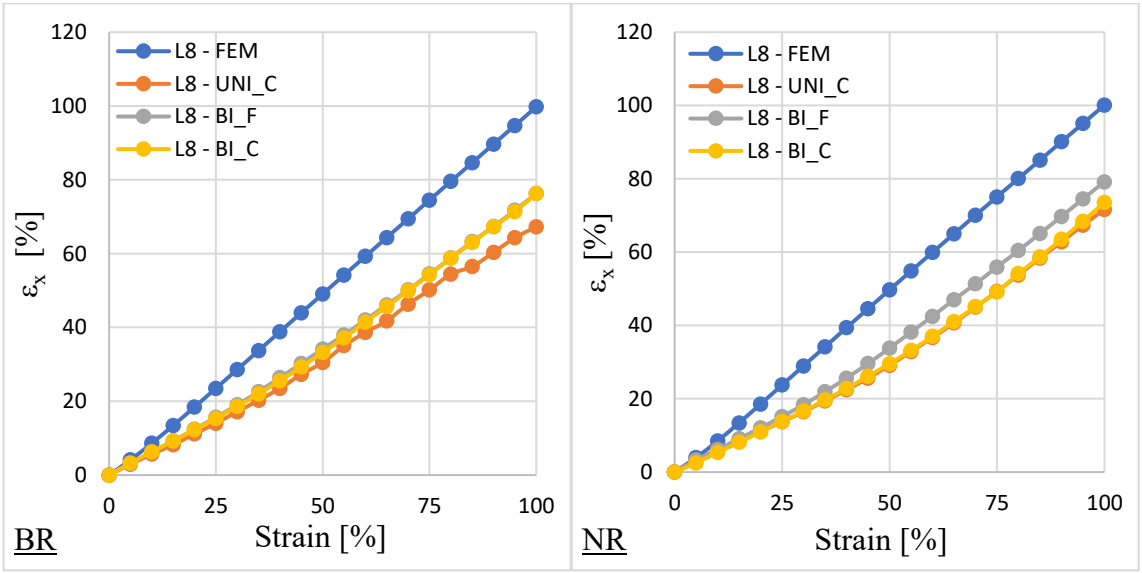

Figure 94 Graphical comparison between FEM and DIC results for BR and NR – Type 2 geometry – L_8

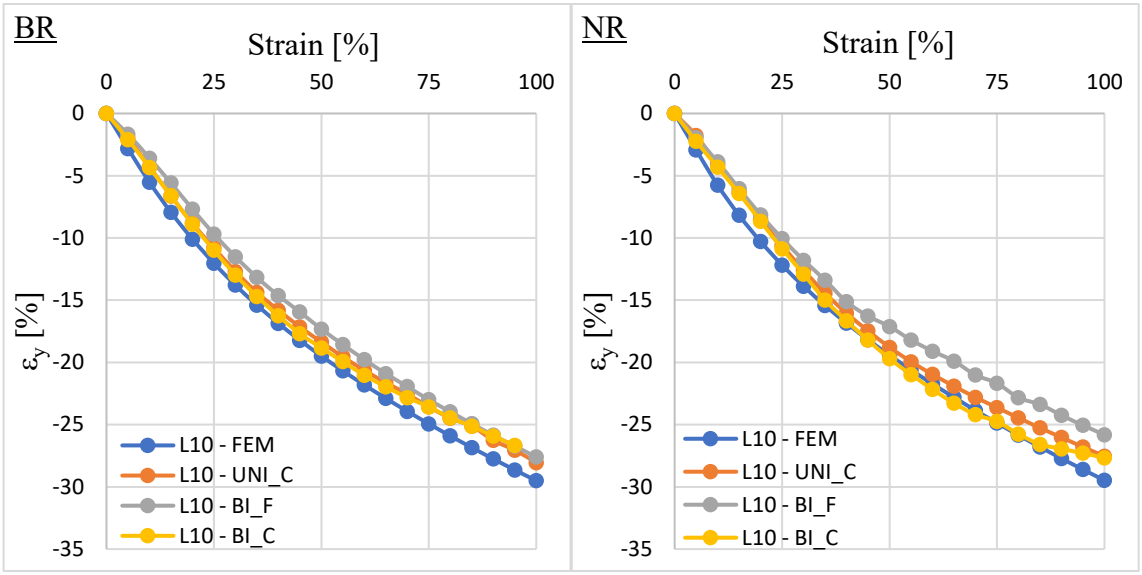

Figure 95 Graphical comparison between FEM and DIC results for BR and NR – Type 2 geometry – L_{10}

Changes in L_8 and L_{10} dimensions for both BR and NR followed similar trends as in the case of hole dimensions' changes, where differences in ε_x for lengthwise dimensions were more substantial, reaching in the case of L_8 over 20 %. At the same time differences in ε_y for transverse dimension L_{10} were in low percentage units. This suggests decreased resemblance when it comes to comparison between lengthwise dimensions.

L_9 showed similar behaviour as L_8 and at the same time L_{11} showed similar behaviour as L_{10} thus it was decided not to implement them into comparison.

Figures 96 and 97 show visual comparison between DIC and FEM samples.

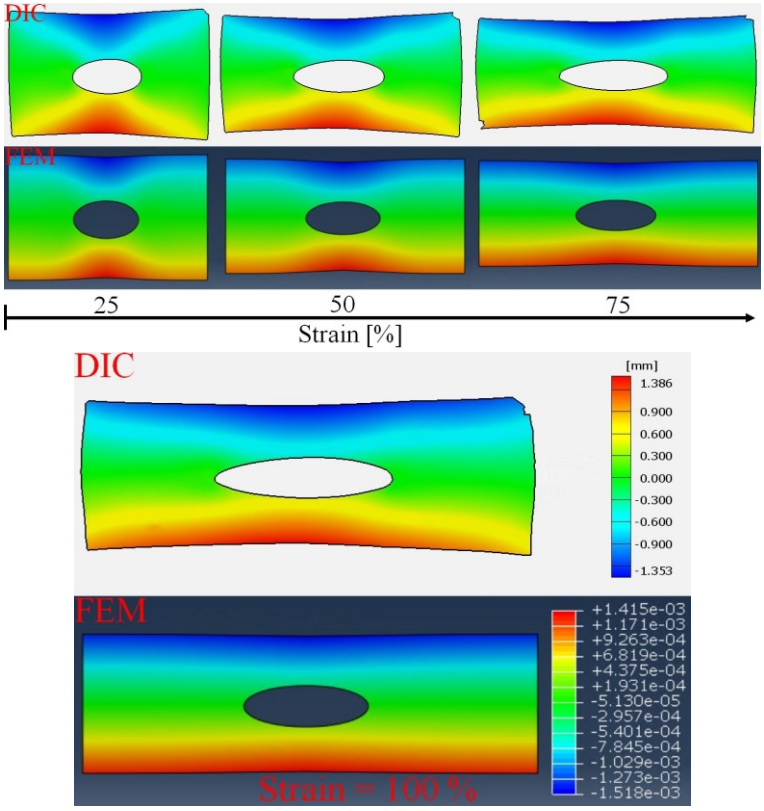

Figure 96 Visual comparison between FEM model and DIC UNI_C measurement for ε_y of BR type 2

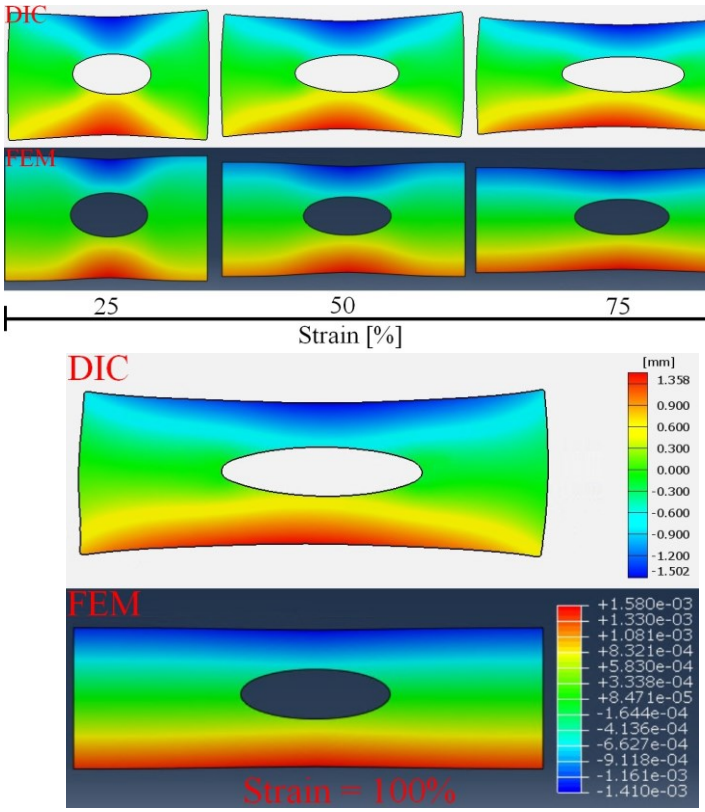

Figure 97 Visual comparison between FEM model and DIC UNI_C measurement for ε_y of NR type 2

Stress – strain curves comparison

Figures 98 and 99 show individual BR and NR comparison between 7 resulting stress – strain data sets. First set is the FEM stress – strain prediction to which stress – strain data of the individual measurement techniques are compared to. These consists of original UNI_C, BI_F and BI_C stress data sets and their equivalents evaluated and edited according to values of sample's transverse contraction ε_y. DIC data sets are thus dependent on the instantaneous sample's cross – section during loading.

Needs to be stated that in the case of type 2 and type 3 geometry, FEM prediction curves in graphs are only illustrative as they highly varied among individual samples. Comparisons in R^2 and m values are then based on evaluation of specific FEM prediction and their practically measured equivalents.

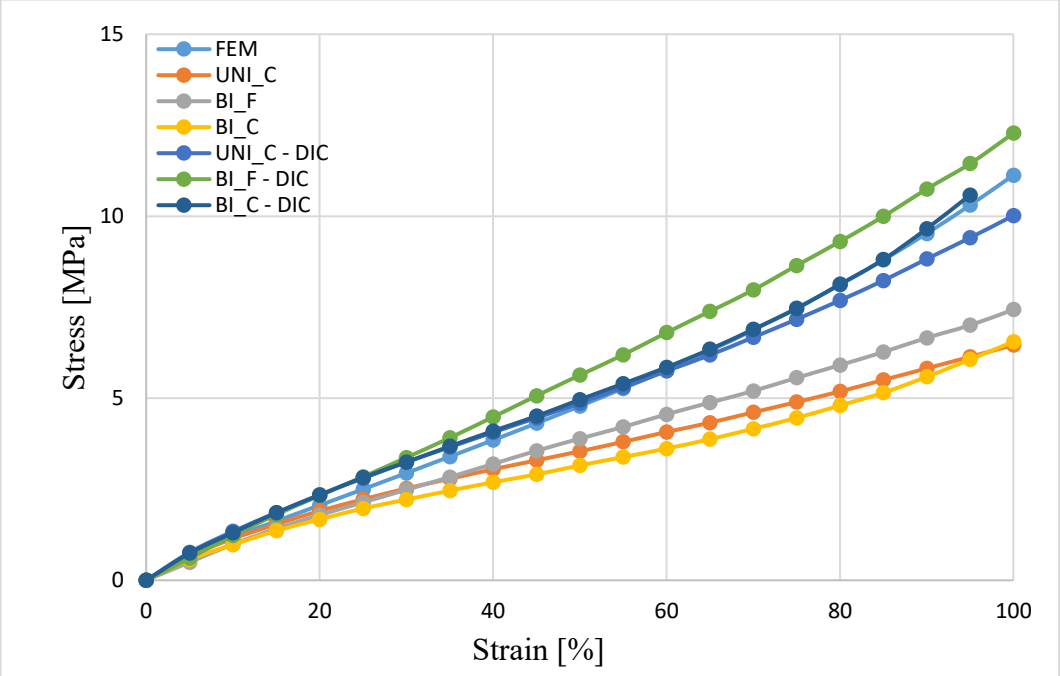

Figure 98 Comparison of stress – strain curves for BR type 2

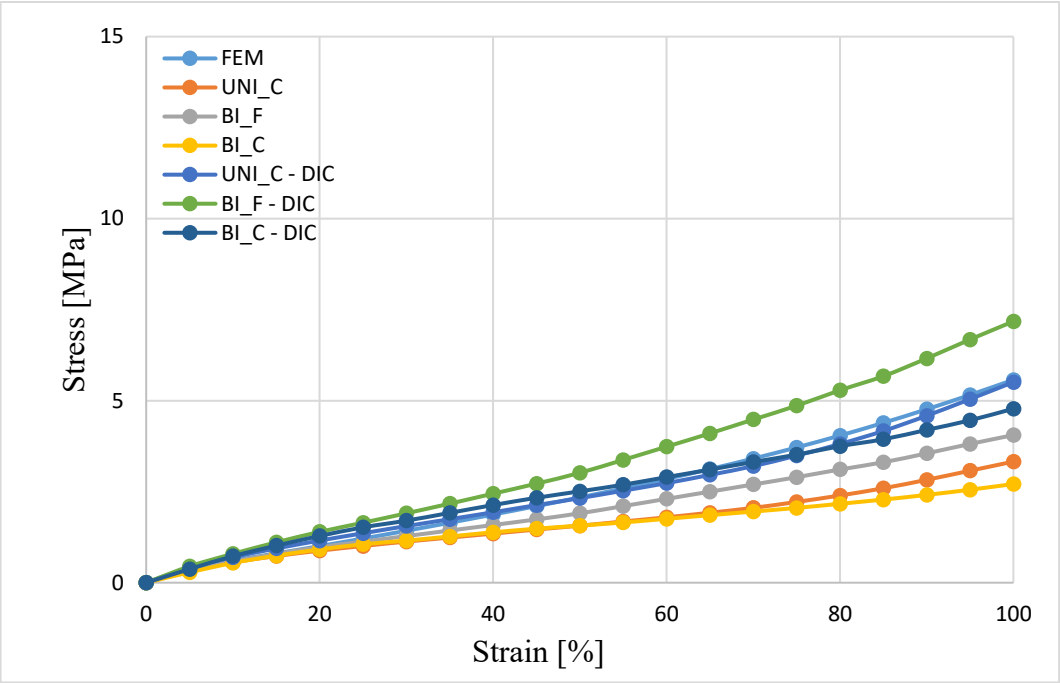

Figure 99 Comparison of stress – strain curves for NR type 2

Comparisons of stress – strain curves for geometry type 2 showed in both BR and NR cases improvements to the original data when implementing DIC instantaneous sample's cross – section dependence during loading, as showed type 1. Stress – strain data without the implementation shows high differences to the FEM predictions whereas DIC data shows high trends' resemblance. The differences of values under the maximal strain level reached up to 4,5 MPa for BR and almost up to 3 MPa for NR.

Differences between individual measuring techniques for BR remained similar as in the case of type 1. However, for NR, differences in stress – strain values between individual measuring techniques increased in comparison with previous results. It can be assumed that differences among individual measuring techniques resulted from high variations in samples' dimensions and their subsequent DIC evaluation. This assumption is supported by R^2 and m comparison in Figures 100 and 101 which presents only small fluctuations in R^2 and m values in comparison with BR material.

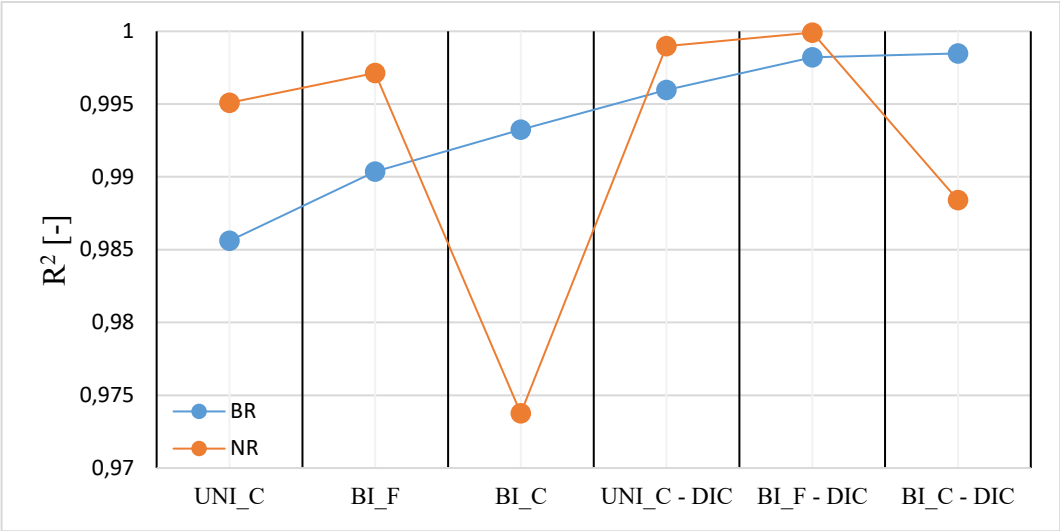

Figure 100 Comparison of R^2 values for BR and NR type 2 geometry stress – strain trends

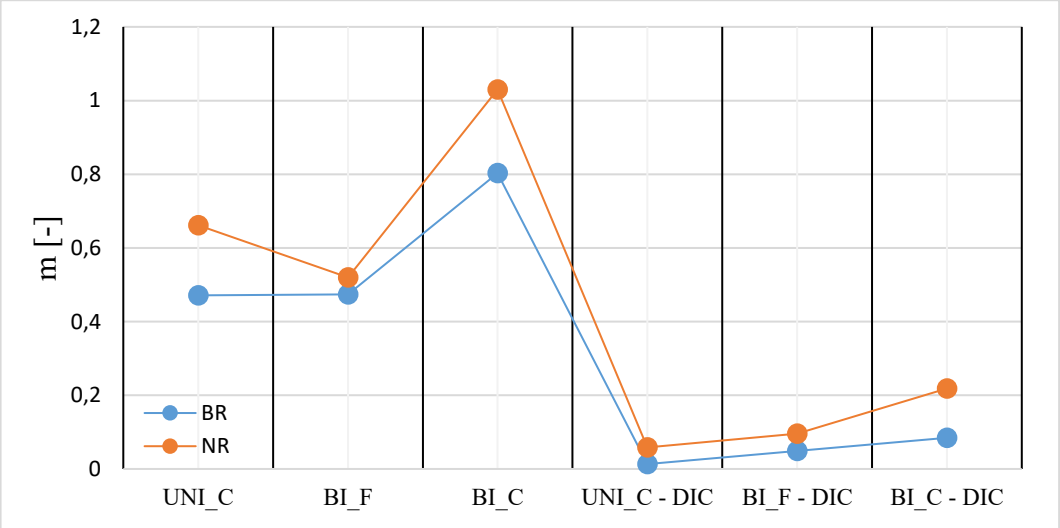

Figure 101 Comparison of *m* values for BR and NR type 2 geometry stress – strain trends

Figures 100 and 101 shows high improvements in both R^2 and *m* values for DIC stress – strain data. Data for both BR and NR follow similar results with BI_F high R^2 value, thus showing a high correlation with FEM predictions. BI_C showed substantial difference in R^2 value between BR and NR. This points out to measuring or evaluation inaccuracy as the same physical sample was used for both bilateral and unilateral measurement techniques. However, material behaviour influence cannot be excluded yet. UNI_C is showing the best curves slope resemblance with FEM predictions.

Furthermore, FEM stress predictions visualized in Figures 102 and 103 shows stress concentration areas. As presumed, these are concentrated mainly on the sides of samples'

holes where the material is thinnest. Small local stresses can be observed on the tips of the holes, however their stress value could not be adequately evaluated as one of the factors to cause these local stresses was imprecise FEM mesh behaviour.

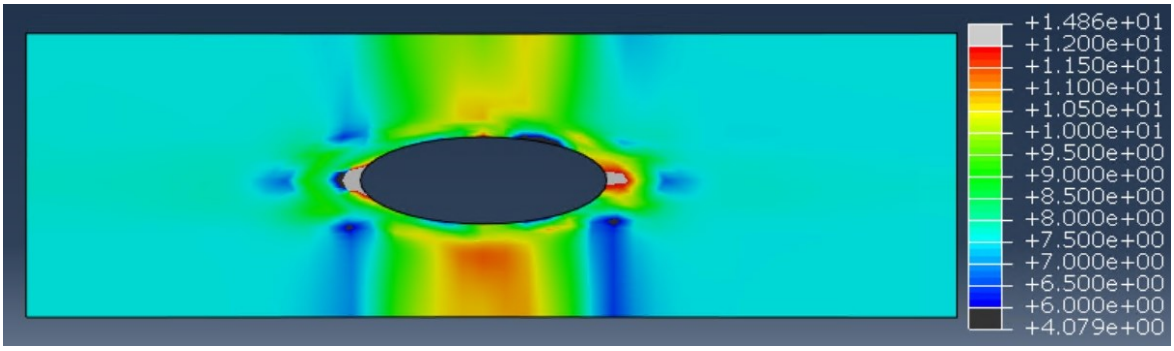

Figure 102 Visualization of FEM stress prediction under maximal strain for BR type 2 UNI_C

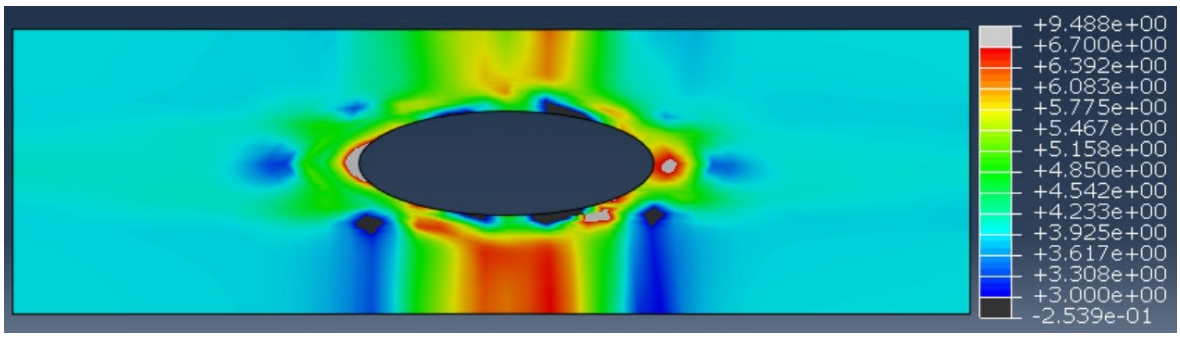

Figure 103 Visualization of FEM stress prediction under maximal strain for NR type 2 UNI_C

5.4.3 Type 3 geometry

Comparison of FEM simulations' results and DIC measurements' results for both BR and NR type 3 geometry.

Outer dimensions deformation

Change in the transverse dimensions L_5, L_6, and L_1 were observed for type 3 geometry under chosen condition $L_1 = L_3$. L_2 and L_4 strains are then equal to the main deformation value.

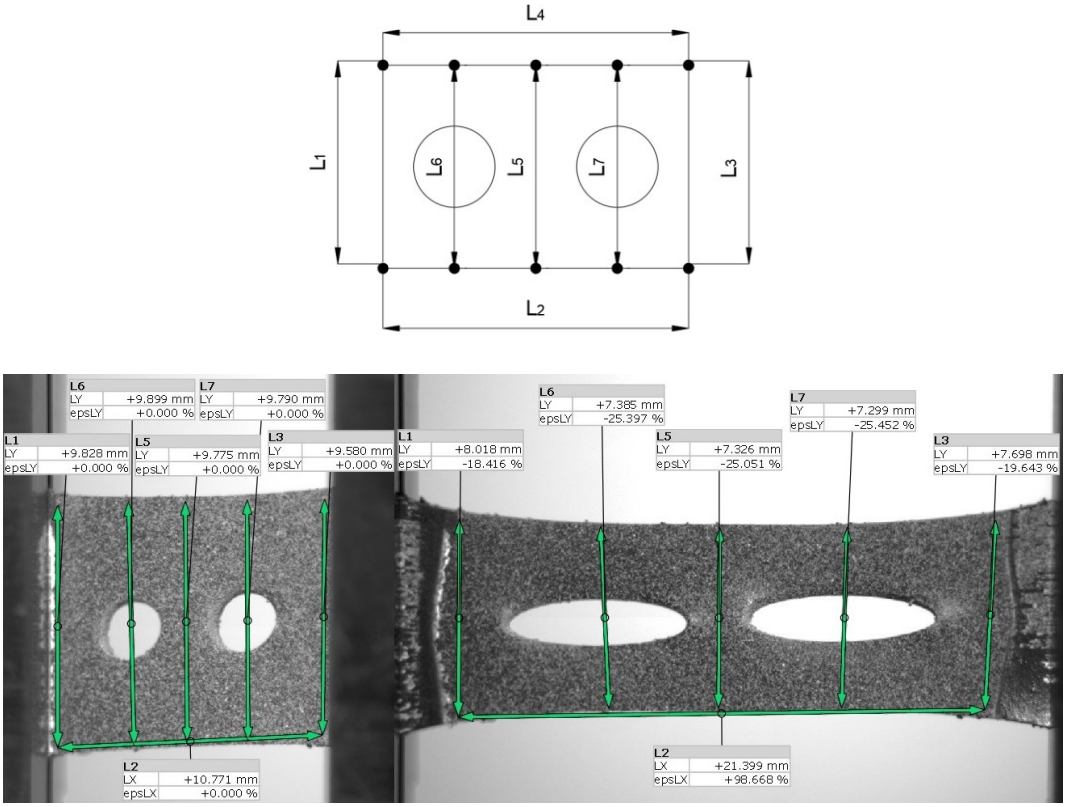

Figure 104 Outer dimensions for geometry type 3

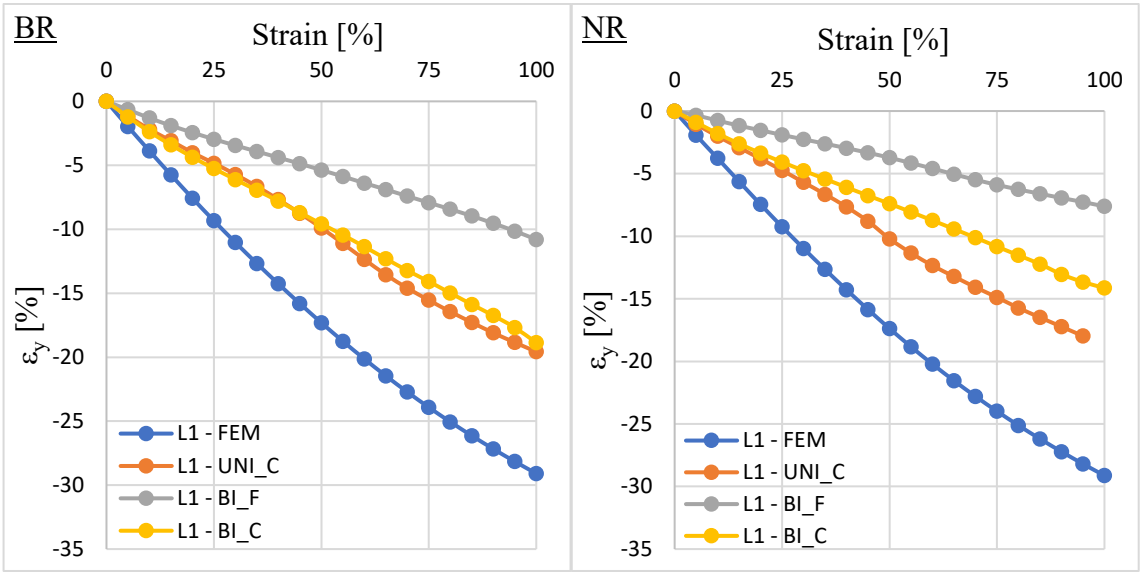

Figure 105 Graphical comparison between FEM and DIC results for BR and NR – Type 3 geometry – L_1

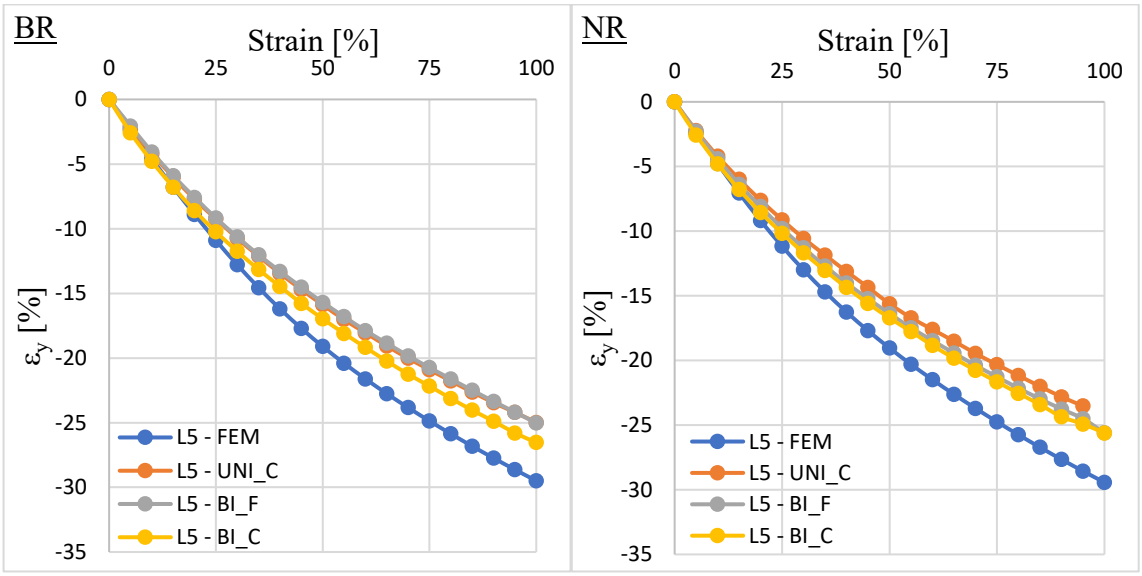

Figure 106 Graphical comparison between FEM and DIC results for BR and NR – Type 3 geometry – L_5

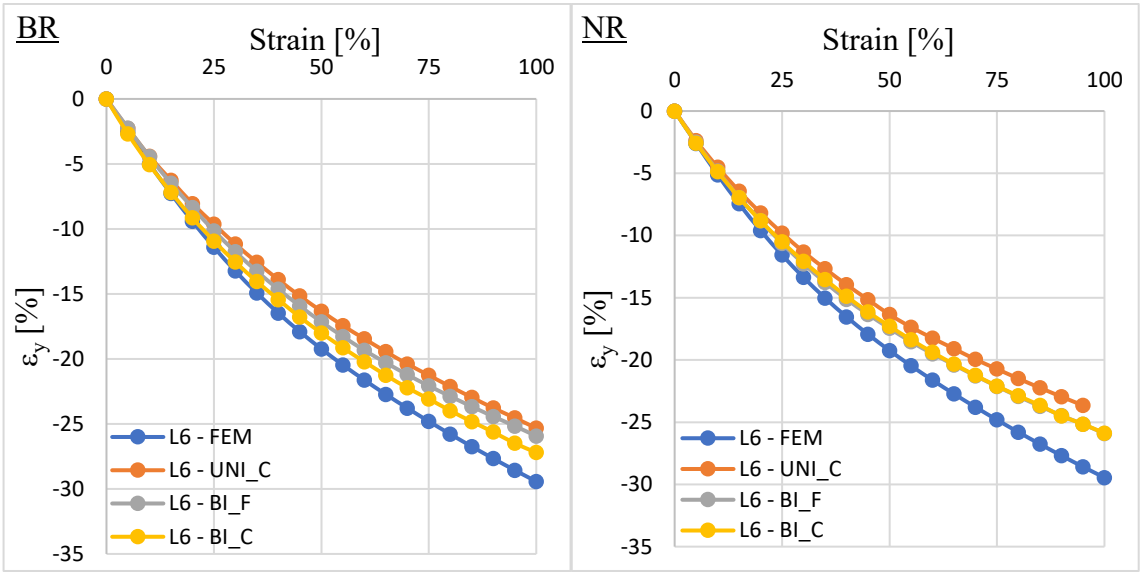

Figure 107 Graphical comparison between FEM and DIC results for BR and NR – Type 3 geometry – L_6

Comparisons of L_5 and L_6 for both BR and NR show similar trends with their type 1 and type 2 equivalents. However, differences of individual measuring techniques to the FEM predictions increased up to 4 %. This increase suggests that the more complicated geometry is used the higher increase in differences can be expected. The Figure 105 then shows identical L_1 behaviour as described for type 2 geometry.

L_7 showed similar behaviour as L_6, thus it was decided not to implement it into comparison.

Groove deformations

Comparison of changes in lengthwise dimension L_8 and transverse dimension L_9 for type 3 geometry.

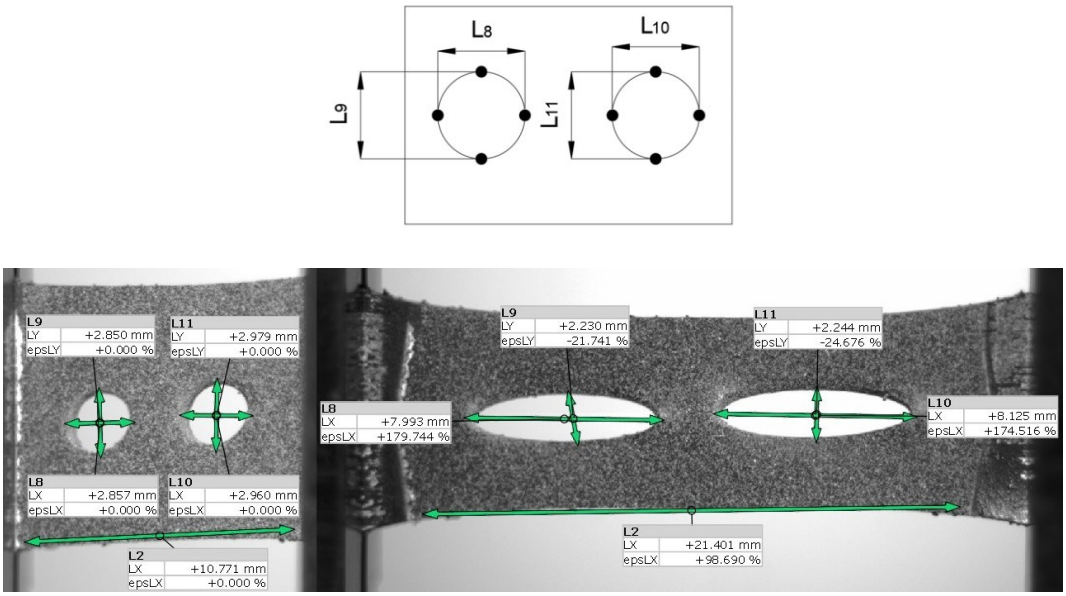

Figure 108 Groove dimensions for geometry type 3

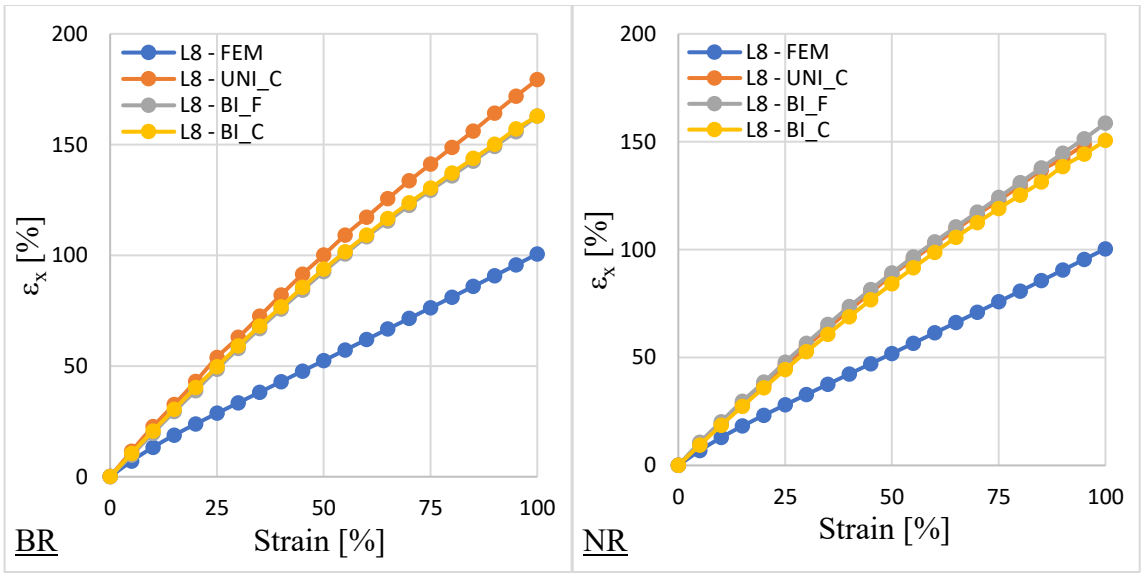

Figure 109 Graphical comparison between FEM and DIC results for BR and NR – Type 3 geometry – L_8

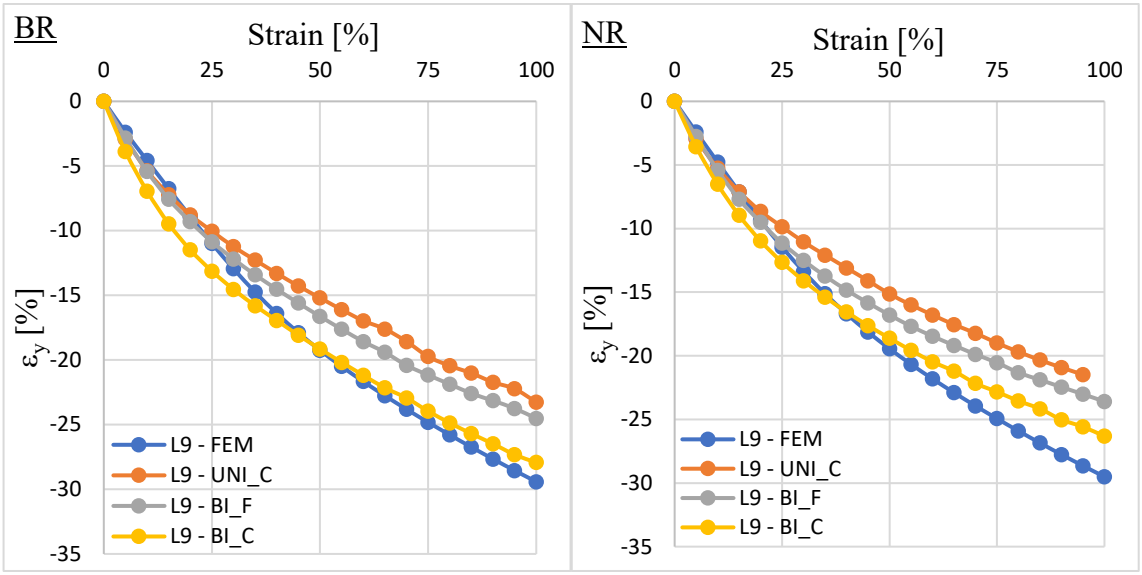

Figure 110 Graphical comparison between FEM and DIC results for BR and NR – Type 3 geometry – L_9

Comparison of L_6 for both BR and NR follow the identical trend of substantial distinction of measured DIC data to the FEM predictions as in the case of type 2 geometry. Difference in ε_x for L_6 slightly decreased for BR to approximately 80 % and for NR to 50 %.

At the same time, comparison of L_9 for both BR and NR showed increase in differences to the FEM predictions as well as among individual measuring techniques.

L_{11} showed similar behaviour as L_9 and L_{10} showed similar behaviour as L_9, thus it was decided not to implement them into the comparison.

Inner dimensions deformation

Comparison of changes in lengthwise dimensions L_{12}, L_{13} and transverse dimension L_{15} for type 3 geometry.

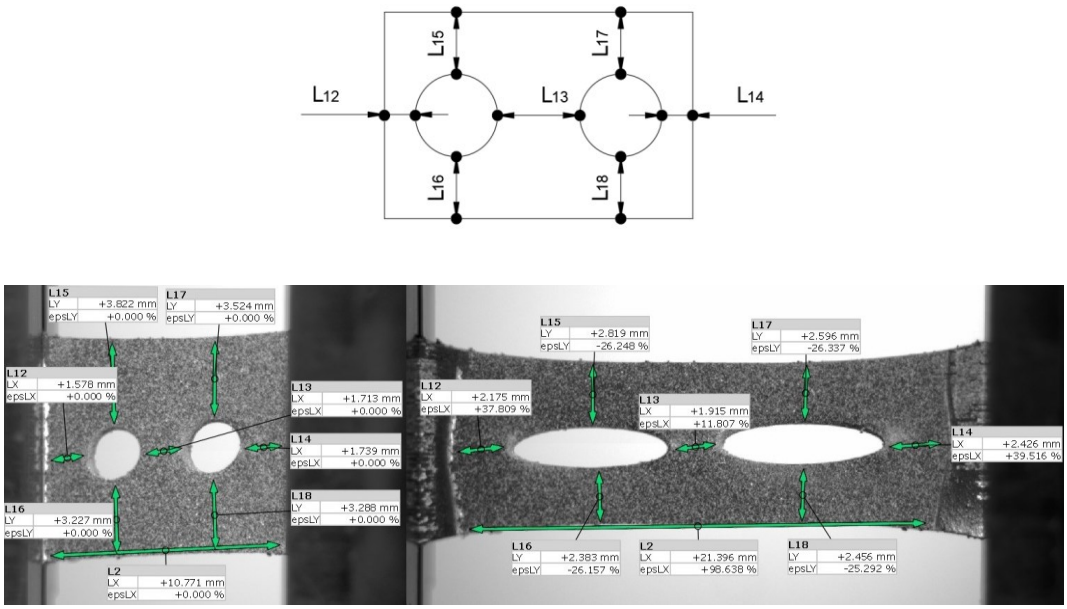

Figure 111 Inner dimensions for geometry type 3

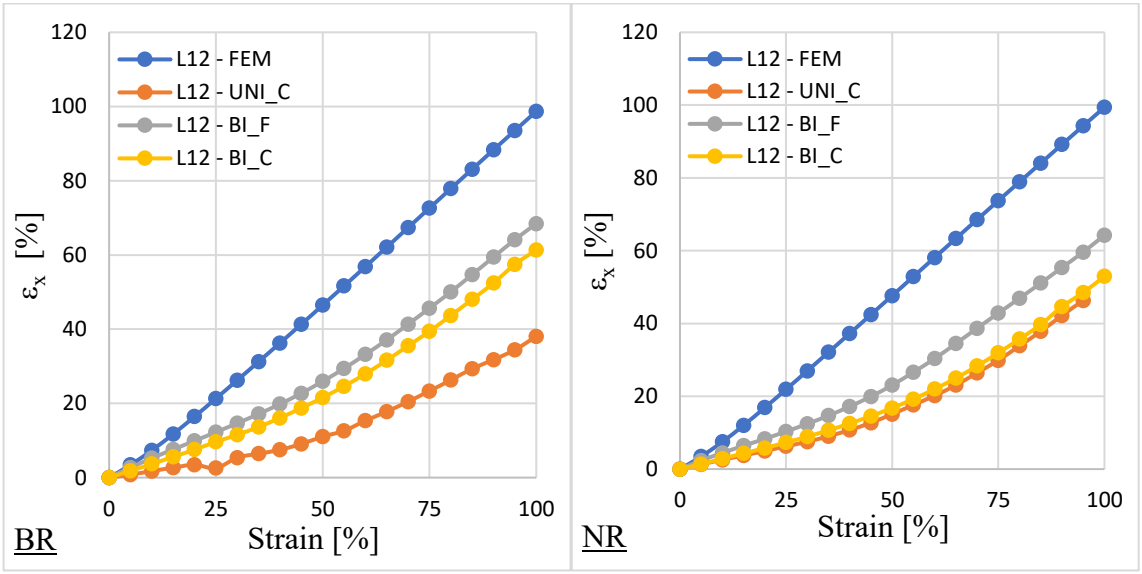

Figure 112 Graphical comparison between FEM and DIC results for BR and NR – Type 3 geometry – L_{12}

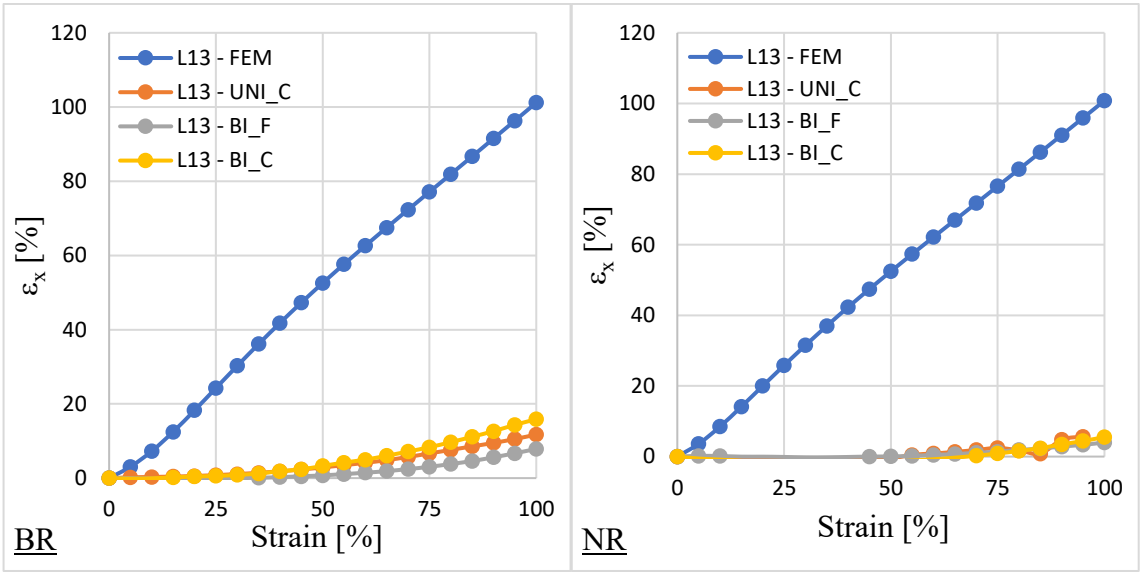

Figure 113 Graphical comparison between FEM and DIC results for BR and NR – Type 3 geometry – L_{13}

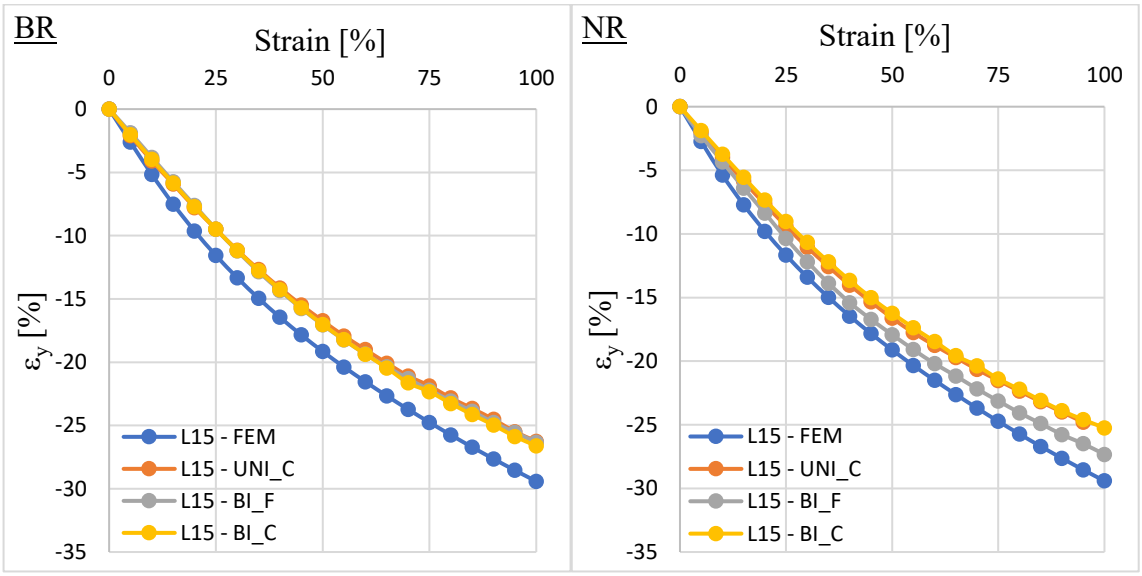

Figure 114 Graphical comparison between FEM and DIC results for BR and NR – Type 3 geometry – L_{15}

Changes in L_{12} and L_{15} dimensions followed similar trends as in the case of type 2 inner dimensions, for both BR and NR. However, whereas L_{15} kept transverse change in percentage units with similar values among measuring techniques, L_{12} increased in differences compared to the FEM prediction with high variations among measuring techniques. Furthermore, comparison of L_{13} shows completely different material behaviour than the one predicted by FEM. It is sure that this inaccuracy is partly caused by

simplification of FEM models of type 3, where the centres of the circular holes were considered completely equal in y axes, whereas the groove centres in physical samples highly varied as it was quite difficult to cut horizontally equal holes. These variations can be seen in the Figures 115 and 116.

L_{14} showed similar behaviour as L_{12} and at the same time L_{16}, L_{17}, L_{18}, showed similar behaviour as L_{15} thus it was decided not to implement them into comparison.

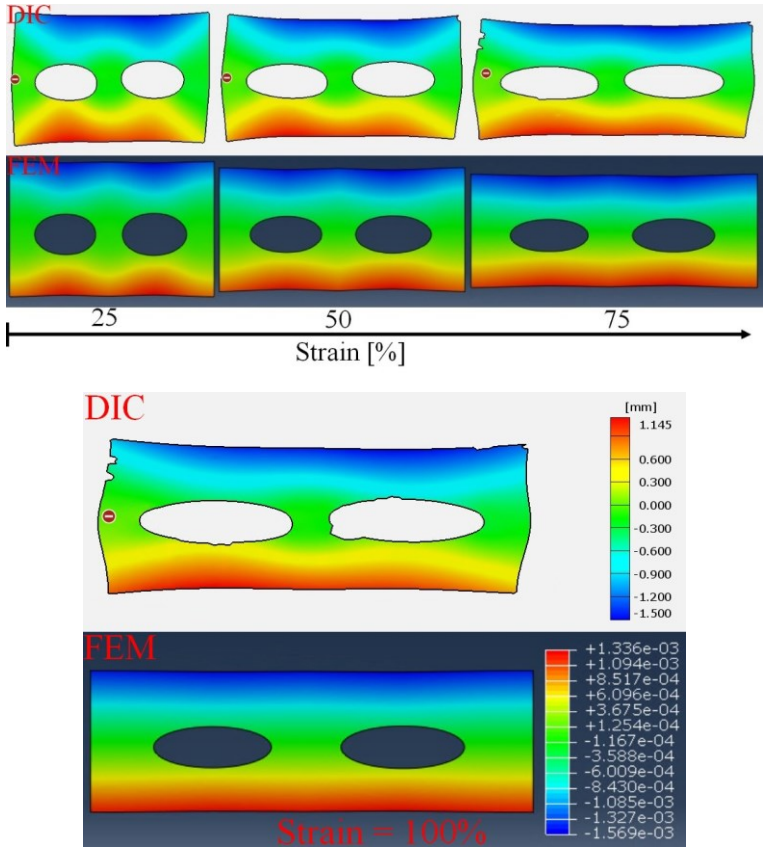

Figure 115 Visual comparison between FEM model and DIC UNI_C measurement for ε_y of BR type 3

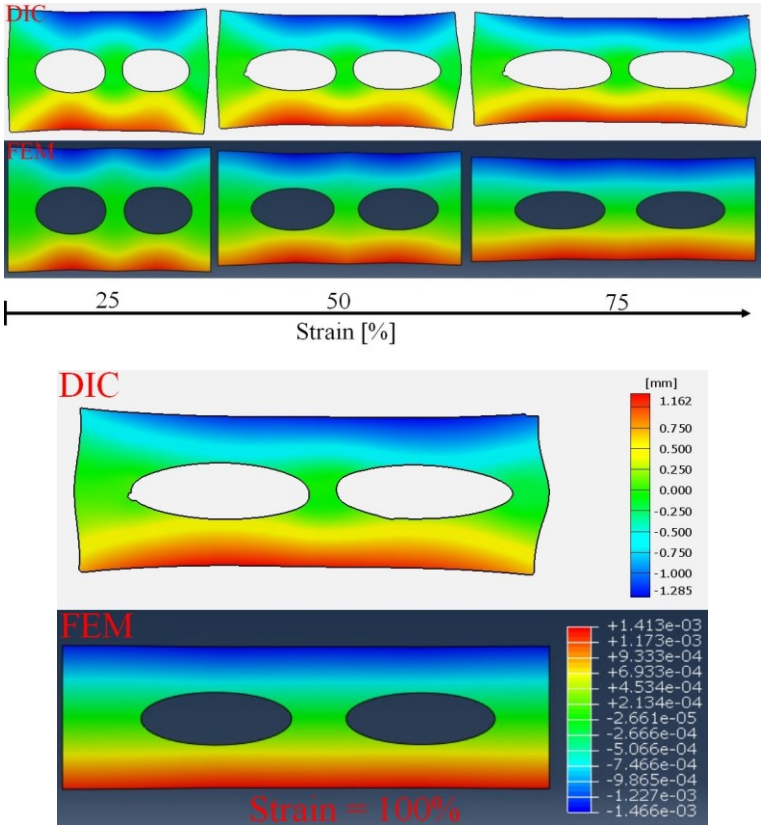

Figure 116 Visual comparison between FEM model and DIC UNI_C measurement for ε_y of NR type 3

Stress – strain curves comparison

Figures 117 and 118 shows individual BR and NR comparison between 7 resulting stress – strain data sets. First set is the FEM stress – strain prediction to which stress – strain data of the individual measurement techniques are compared to. These consists of original UNI_C, BI_F and BI_C stress data sets and their equivalents evaluated and edited according to values of sample's transverse contraction ε_y. DIC data sets are thus dependent on the instantaneous sample's cross – section during loading.

Needs to be stated that in the case of type 2 and type 3 geometry FEM prediction curves in graphs are only illustrative as they highly varied for individual samples. Comparisons in R^2 and m values are then based on evaluation of specific FEM prediction and their practically measured equivalents.

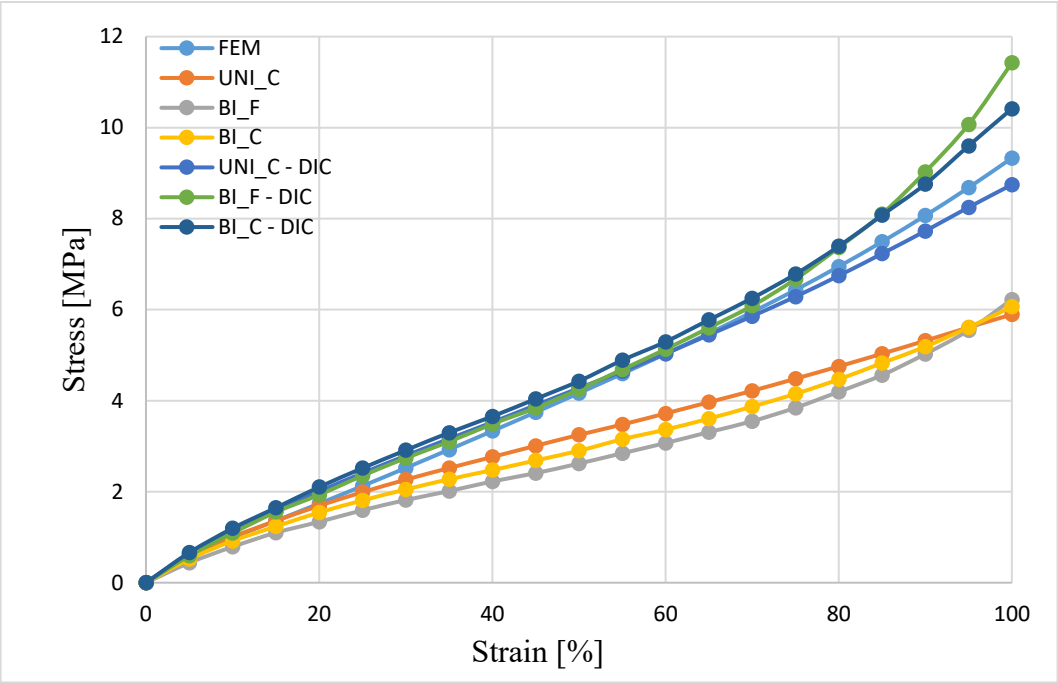

Figure 117 Comparison of stress – strain curves for BR type 3

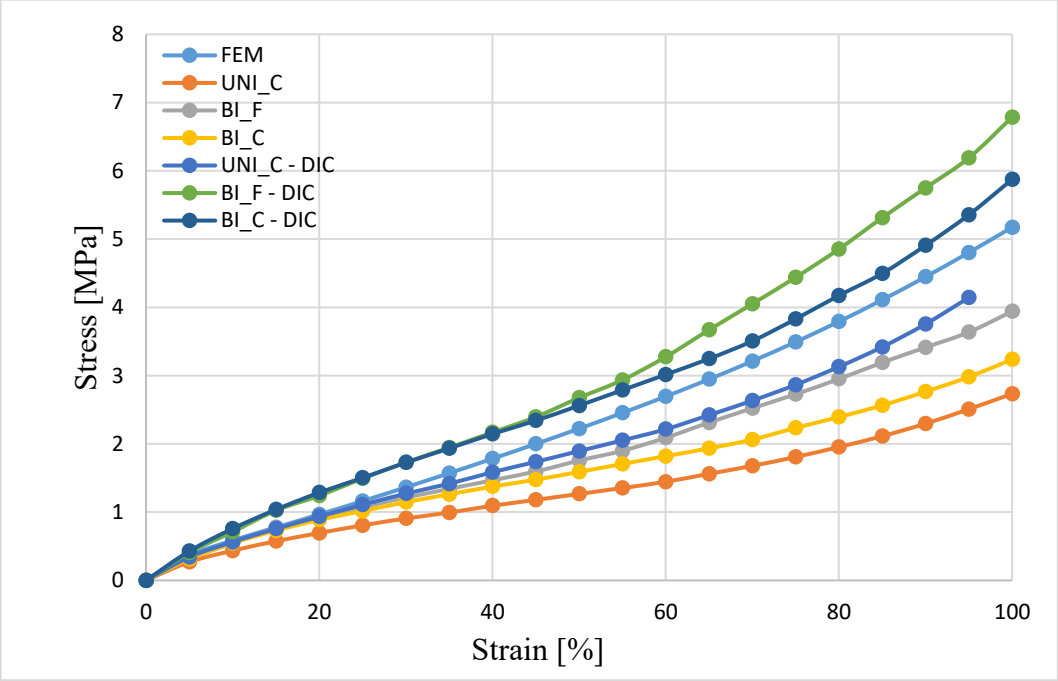

Figure 118 Comparison of stress – strain curves for NR type 3

Comparisons of stress – strain curves for geometry type 3 showed in both BR and NR cases improvements to the original data when implementing DIC instantaneous sample's cross – section dependence during loading, as showed type 1 and type 2. Stress – strain data without

the implementation shows high differences to the FEM predictions whereas DIC data shows high trends' resemblance. The differences of values under the maximal strain level reached up to 5,5 MPa for BR and up to 2,5 MPa for NR. Differences between individual measuring techniques for BR remained similar as in the case of type 1 and type 2. However, for NR, differences in stress – strain values between individual measuring techniques increased further on, in comparison with previous results. As in the case of NR type 2 it can be assumed that differences among individual measuring techniques resulted from high variations in samples' dimensions and their subsequent DIC evaluation.

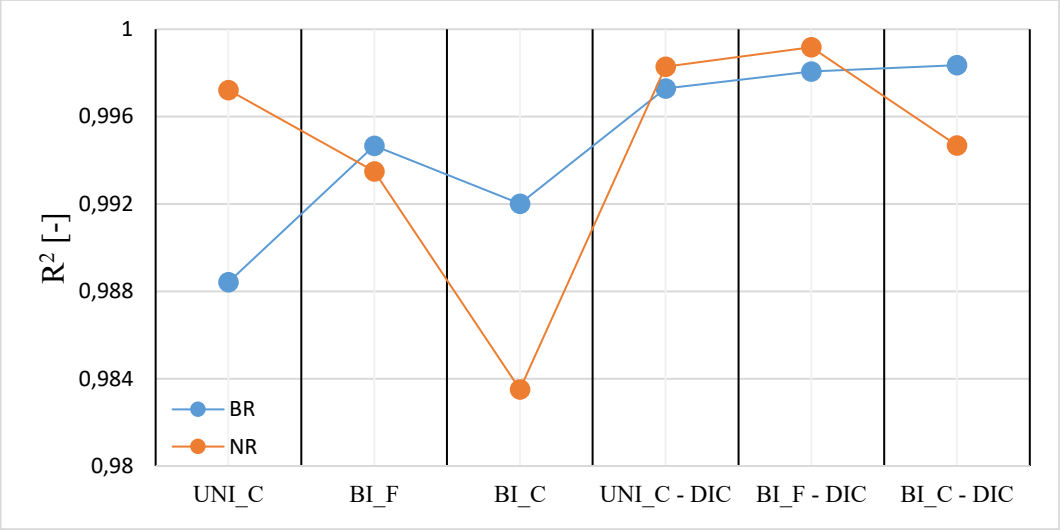

Figure 119 Comparison of R^2 values for BR and NR type 3 geometry stress – strain trends

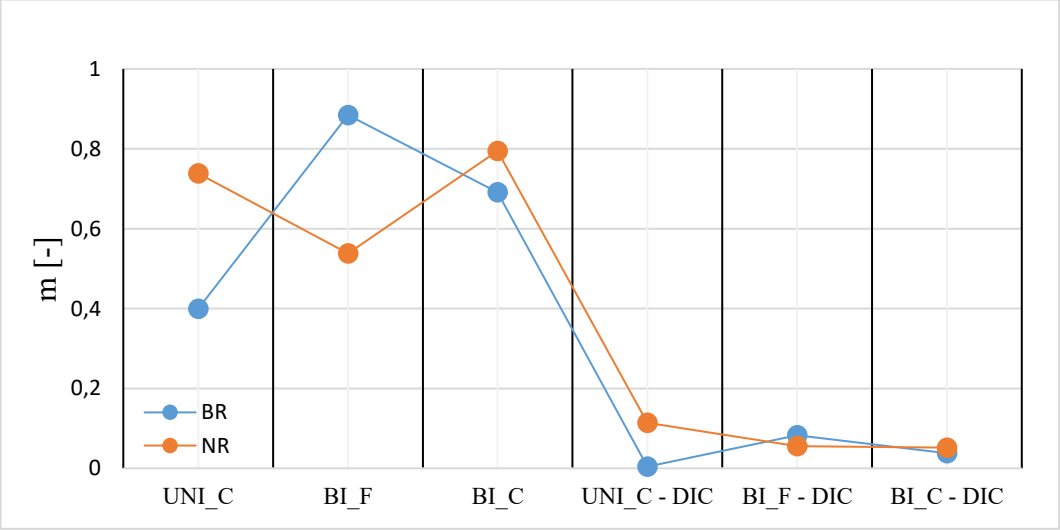

Figure 120 Comparison of *m* values for BR and NR type 3 geometry stress – strain trends

Figures 119 and 120 shows high improvements in both R^2 and m values for DIC stress – strain data as in the previous comparisons. Data for both BR and NR follow similar results with BI_F and BI_C high R^2 value, thus showing a high correlation with FEM predictions. BI_C showed difference in R^2 value between BR and NR as in the case of type 2 but with a noticeable improvement. This can support assumption that the material behaviour was not as influential as possible measuring or evaluation inaccuracies during BI_C type 2 measurement and assessment.

Variations among BR and NR occurred even in m value comparison. For BR UNI_C showed the best curve's slope resemblance with FEM predictions while for NR BI_F and BI_C were assessed as the best.

Figures 121 and 122 then shows stress concentration areas. As in the case of type 2 visualization, these are concentrated mainly on the sides of samples' holes where the material is thinnest. Small local stresses can be observed on the tips of the holes, however their stress value could not be adequately evaluated as one of the factors to cause these local stresses was imprecise FEM mesh behaviour.

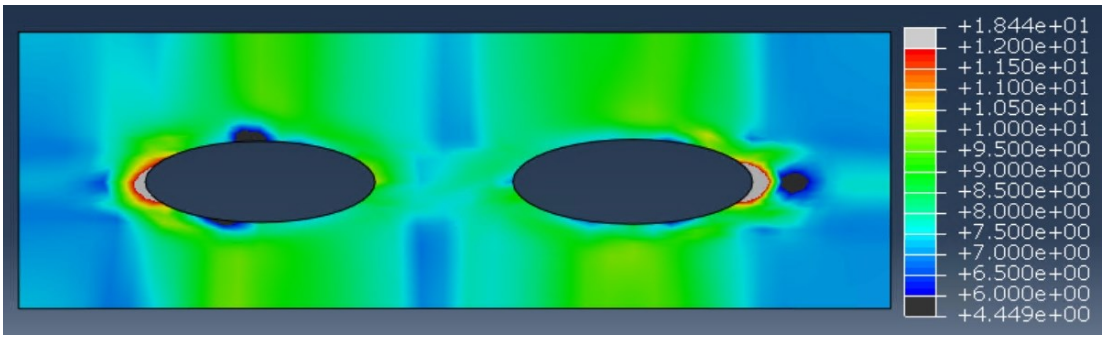

Figure 121 Visualization of FEM stress prediction under maximal strain for BR type 3 UNI_C

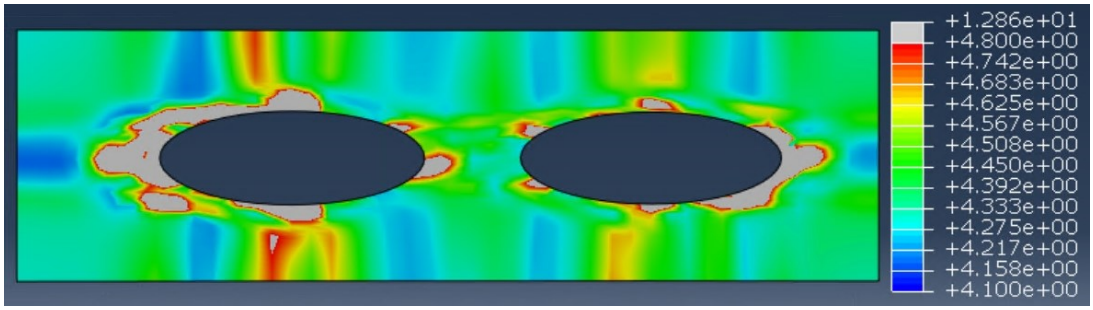

Figure 122 Visualization of FEM stress prediction under maximal strain for NR type 3 UNI_C

5.4.4 Summary

Comparison of deformation behaviour between practical DIC measurements and FEM simulations was individually carried out based on three geometry types for both BR and NR rubber materials and three measuring techniques. The goal of the comparison was to confirm or disprove similarity between the concerned data sets and thus determine the level of reliability of FEM models' predictions of material behaviour to the practically measured material behaviour data.

The first step for each geometry type was comparison of deformation behaviour for individual dimensions. The comparison was based on assessment of differences in transverse ε_y and lengthwise ε_x dimension changes. Comparison for type 1 geometry showed high trend resemblance between predicted FEM data and DIC data. The differences in ε_y values between FEM and DIC data were in percentage units, namely maximally 3 % for both BR and NR. Similar behaviour was observed for outer dimensions deformation of type 2 and type 3 geometries. For type 2, apart from L_1 dimension compromised by clamping force, the main transverse dimension L_5 even showed slight improvements in differences between FEM and DIC data, as well as among individual measuring techniques for both BR and NR. The differences in ε_y values between FEM and DIC data were maximally 1 % for BR and 3 % for NR. Type 3 geometry then showed slight deterioration compared to type 1 and type 2 geometries with maximal difference of 4.5 % for both BR and NR. However, these ε_y values fluctuations and variations in resemblance among individual geometry types are still considered to be highly reliable. In all cases the results of the main dimensions' transverse contraction for individual geometry types can be taken as normalized level of reliability for other examined dimensions.

Comparisons of circular holes deformations demonstrated first substantial differences between FEM and DIC data. Holes' transverse contraction followed similar trends to those of the outer transverse dimensions. However, differences in ε_y value increased for both BR and NR with higher variations among individual measuring techniques. Differences in ε_x value and variations among individual measuring techniques were more substantial for type 3 then for type 2. Meanwhile, comparison of ε_x value for lengthwise holes' dimensions showed high disproportions between FEM and DIC. Differences in ε_x reached up to 100 % for type 2 and up to 80 % for type 3. However, these differences to the FEM predictions were highly similar for all measuring techniques and both materials. This proves that no

substantial measuring and evaluating inaccuracies affected the results, but rather that the holes on real samples deformed seemingly more than their FEM counterparts.

The holes' behaviour is supported by comparison of inner dimensions' deformation. While transverse ε_y values followed equal trends as their outer counterparts with differences in percentage units between FEM and DIC data with low values variations among individual measuring techniques, lengthwise ε_x values showed similarly substantial disproportions between FEM and DIC as in the case of holes' lengthwise deformations. According to FEM predictions these lengthwise inner dimensions should have stretched up to 100 % but DIC data showed 80 % stretch for type 2 and only 60 % for type 3 with dimension L_{13} showing completely different behaviour than predicted. These results show that lengthwise deformation was more likely to be concentrated within individual holes rather than in the sample's material.

The final step of the comparison between FEM predictions and DIC measured data was evaluation of stress – strain curves. Comparison proved that chosen hyperelastic model and set boundary conditions are highly capable to compensate samples' width contraction behaviour and thus provide more reliable and precise stress – strain curves data, than the real stress – strain data obtained by individual measuring techniques. This could be proved due to implementation of instantaneous sample's cross – section dependence acquired by DIC measurement. DIC stress – strain data with instantaneous sample's cross – section implementation showed high resemblance with predicted FEM data for both BR and NR as well as among individual measuring techniques within geometry types.

Figures 123, 124 and 125 shows comparison of individual measuring techniques among investigated geometry types for both BR and NR throughout whole loading process. The goal of this comparison is to show differences in samples' stress – strain behaviour and precision of used measuring techniques against the complexity of investigated geometries. The comparison is based upon stress difference between DIC stress – strain data with instantaneous sample's cross – section dependence and FEM stress – strain predictions according to Equation (27):

$$Stress\ difference = Stress_{FEM} - Stress_{DIC} \tag{27}$$

which states that the closer the stress difference value is to zero the more similar was DIC stress – strain curve to the FEM predictions.

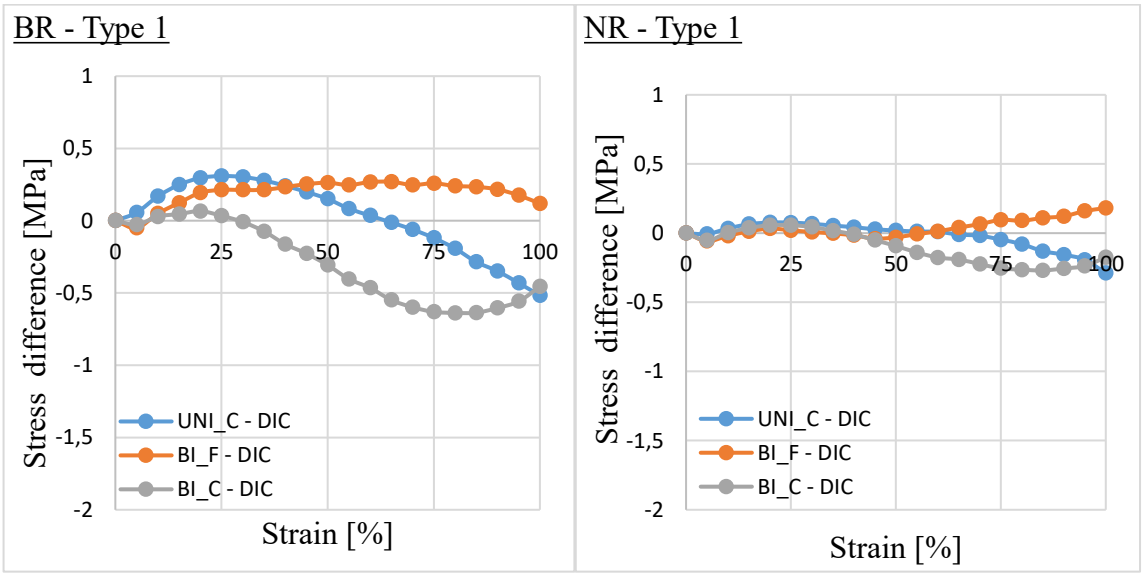

Figure 123 Comparison of absolute strain differences of individual measuring techniques for type 1 geometry; BR (left), NR (right)

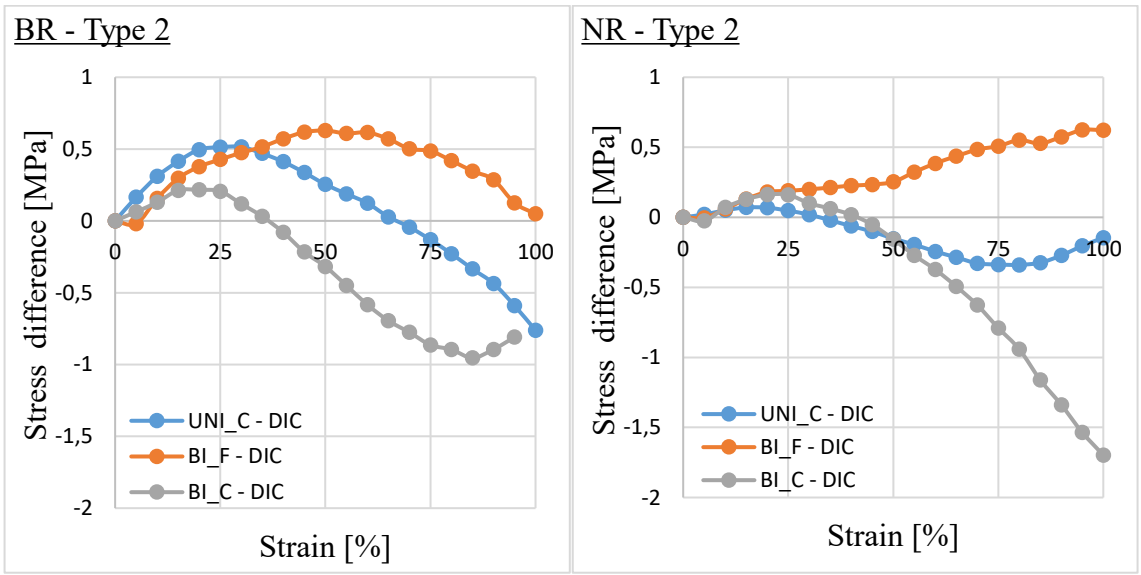

Figure 124 Comparison of absolute strain differences of individual measuring techniques for type 2 geometry; BR (left), NR (right)

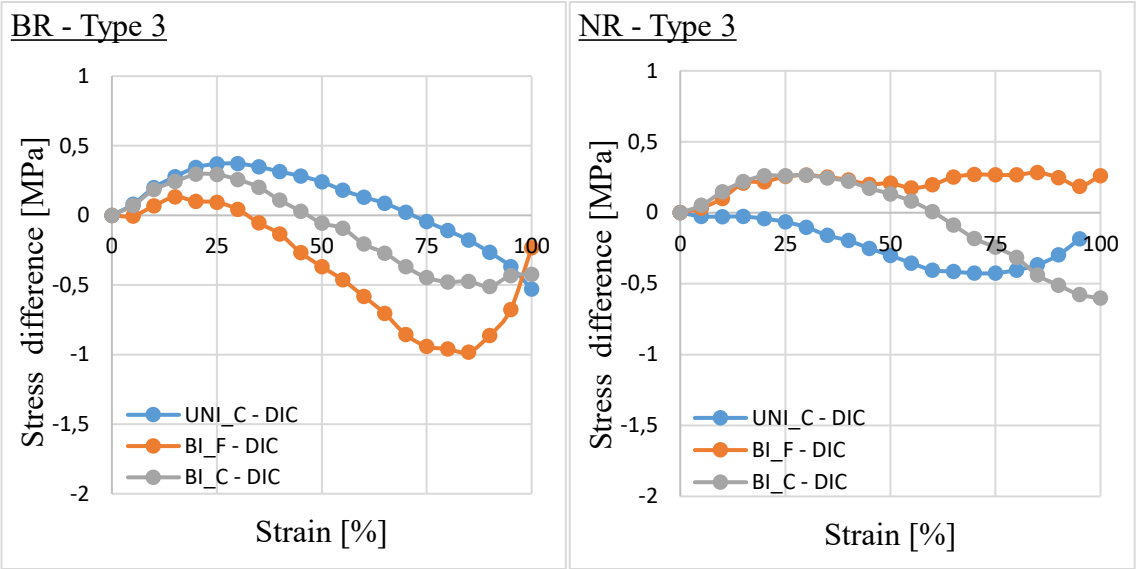

Figure 125 Comparison of absolute strain differences of individual measuring techniques for type 3 geometry; BR (left), NR (right)

The comparison shows that simple type 1 geometry was the most stable among designed geometry types. Type 1 shows low stress differences among all measuring techniques with higher resemblance with FEM predictions for smaller strain levels. Type 2 and type 3 show similarly higher stress differences. This points out, that the more complex studied geometry is, the more difficult it is to obtain precise and reliable material behaviour data. Comparisons also show overall increase in differences with rising strain level.

Figures 126, 127 and 128 shows comparison of individual geometry types among measuring techniques for both BR and NR throughout whole loading process. The comparison is based upon stress difference between DIC stress – strain data with instantaneous sample's cross – section dependence and FEM stress – strain predictions according to Equation (27). The goal of this comparison is to show differences in samples' stress – strain behaviour and precision of used measuring techniques against used loading principles and clamping techniques.

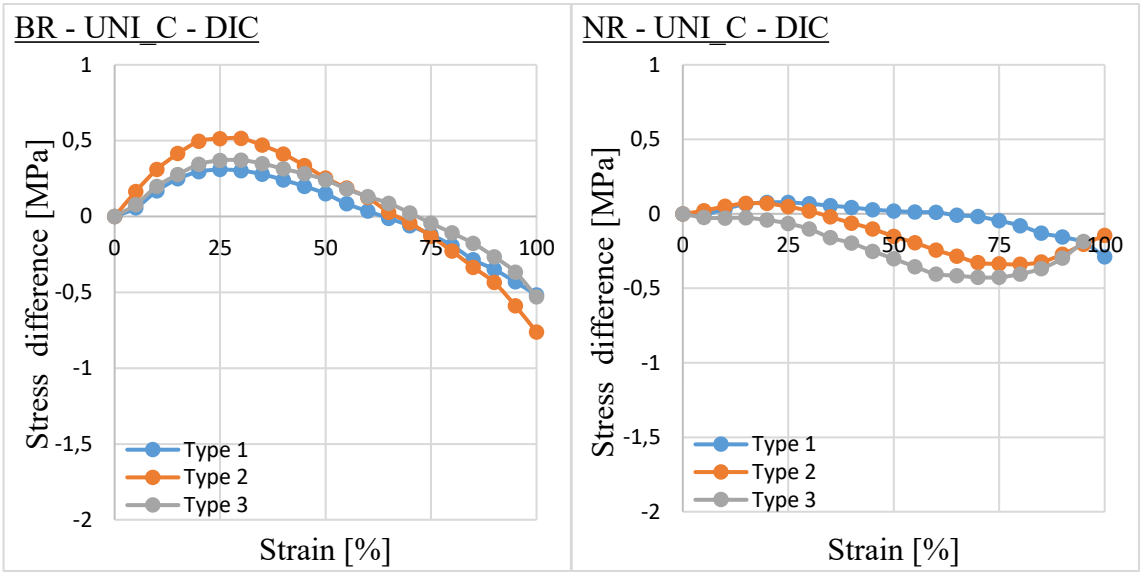

Figure 126 Comparison of absolute strain differences of individual geometry types for UNI_C measuring technique; BR (left), NR (right)

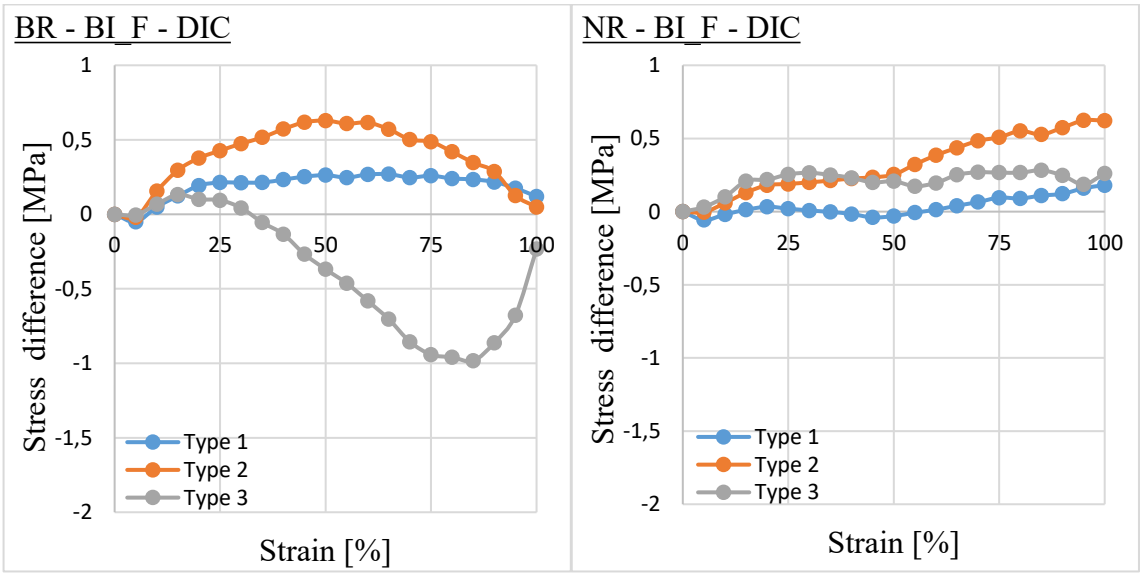

Figure 127 Comparison of absolute strain differences of individual geometry types for BI_F measuring technique; BR (left), NR (right)

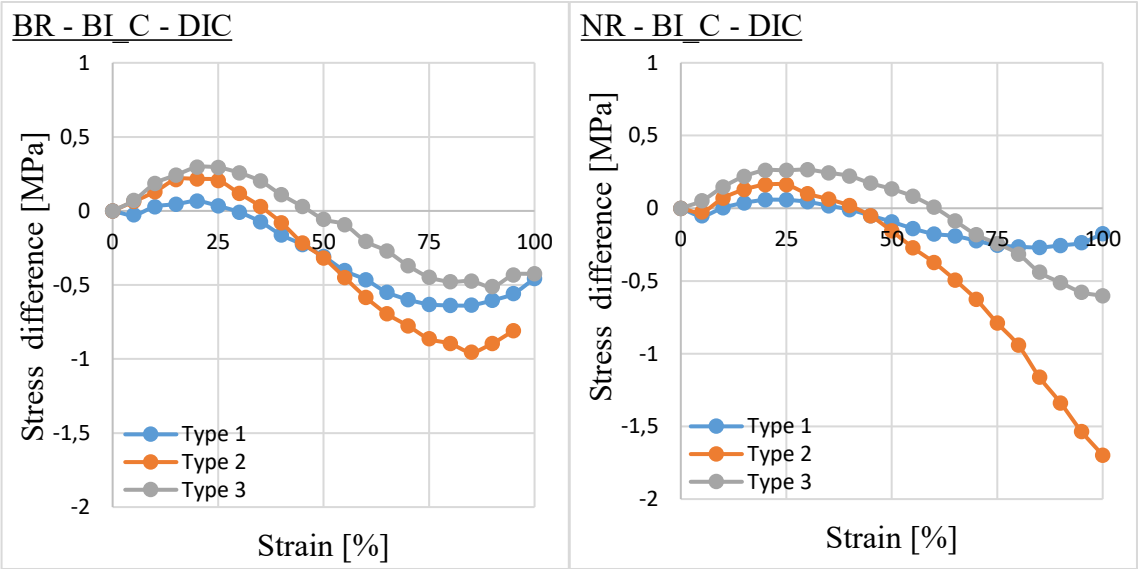

Figure 128 Comparison of absolute strain differences of individual geometry types for BI_C measuring technique; BR (left), NR (right)

The comparison shows that BI_F was in four cases the most stable measuring technique, specifically for BR type 1 and type 2 and NR type 1 and type 3 measurements. BI_F was followed by UNI_C which proved to be most stable for BR type 3 and NR type 1 and type 2. BI_C showed least reliable results. Therefore, BI_F was determined as most reliable and precise measurement technique within scope of this study as the resulting data showed the largest similarity with FEM predictions.

Overall, evaluation of comparison between FEM predictions and DIC measured data proved, that the values of proportional changes in transverse direction ε_y showed high correlations and resemblance in cases of simple geometry subjected to lower strain levels. On the contrary, more complex geometry subjected to higher loading levels showed higher differences between simulated data and real samples' behaviour. This behaviour was partly followed by comparison of results of individual measuring techniques which varied more substantially in the cases of complex geometries. The values of proportional changes in lengthwise direction ε_x showed substantial distinctions between FEM predictions and DIC measured data. During measurements and subsequent evaluations no major errors have been observed for lengthwise dimensions, thus it is highly possible that the chosen hyperelastic model together with chosen boundary conditions could not reliably describe and predict more complex geometries with lengthwise deformations parallel to loading. However, combination of inaccuracies, simplified simulations and insufficient FEM model is possible

as well. Finally, no major differences between BR and NR behaviour were observed. NR proved to be less stable during DIC measurement therefore the resulting curve data were in some cases rough in comparison to BR however, trends remained similar for both materials.

CONCLUSION

This thesis deals with the problematics of Finite Element Method (FEM) and Digital Image Correlation (DIC) practical implementation into already established measuring and testing methods of rubber materials. The main goal of the thesis was to conduct experimental study within which a practical DIC measurement was critically compared with FEM analysis and thus identifying benefits provided by implementation of these methods, but also recognize possible drawbacks and their potential solutions. The main emphasis was placed on verification, whether the implementations improve general results obtained by common testing methods.

Study was divided into four parts. First a measurement to obtain general data of material behaviour was carried out. Second part focused on practical DIC measurement of two rubber materials, with four measuring techniques, among three geometrically distinguishable sample types, was carried out, using simple quasi-static tensile loading. Next, the FEM evaluation of acquired material data, design of FEM analysis and processing of created simulations. The last part consists of detailed comparison between FEM predictions data and practical DIC data thus obtaining final results.

Study proved conclusive benefits of FEM and DIC implementation. Measurements improved by these two methods followed higher results' accuracy and reliability in comparison with plain data. DIC part of the study proved conclusive necessity of the technique. DIC was highly capable to record and evaluate samples' behaviour for every chosen geometry of focus throughout chosen loading conditions. This evaluation would be impossible without DIC implementation as the standard, mainly mechanic measuring techniques are unable to measure and record mechanical behaviour on such high level with such accuracy as they were subjected in this study. Furthermore, DIC measurement enabled to determine and prove high precision and reliability of FEM hyperelastic models' when used under adequate conditions for suitable cases.

However, weaknesses of both FEM and DIC were recognized as well. Mainly in terms of used FEM models' incapability to describe lengthwise elongations of more complex geometries under higher level of strains and also, a high dependence on precision of practical measurements for DIC.

Furthermore, several additional conclusions were recognized. Mainly the effects of loading conditions, complexity of studied samples as well as variations among measuring techniques

of DIC measurements. Loading conditions highly affected accuracy of the measurements as the higher the applied strains were, the less accurate and reliable results were obtained. Similarly, the more geometrically complex sample was studied, the more difficult it was to successfully conduct the measurement and acquire accurate data. Variations of measuring techniques' precision resulted in assessment of the bilateral loading principle conducted on Intrinsic Strength Analyser (ISA), with special clamping grips, as the most reliable and precise technique within the scope of this study. And lastly, no major effect of elastomer materials composition on the measurements were recognized, as the results were consistent for both BR and NR samples.

These overall findings provide basic information for potential future studies, thus providing foundations for implementation of FEM and DIC methods into more complex and specific problematics.

REFERENCES

[1] DVOŘÁK, Z.; JAVOŘÍK, J. *Elastomerní konstrukční materiály*. Česká společnost průmyslové chemie, 2009.

[2] MALÁČ, J. Gumárenská technologie. *Zlín: UTB Zlín*, 2005.

[3] BERGSTROM, J. *Mechanics of solid polymers: theory and computational modeling*. William Andrew, 2015.

[4] BOWER, A. *Applied mechanics of solids*. CRC press, 2009.

[5] JAVOŘÍK, J. Hyperelasticita. (učební text)

[6] MILLER, K. Testing elastomers for hyperelastic material models in finite element analysis. *Axel Products Testing and Analysis Report*, 2000.

[7] PEARSON, I.; PICKERING, M. The determination of a highly elastic adhesive's material properties and their representation in finite element analysis. *Finite elements in analysis and design*, 2001, 37.3: 221-232.

[8] SASSO, M., et al. Characterization of hyperelastic rubber-like materials by biaxial and uniaxial stretching tests based on optical methods. *Polymer Testing*, 2008, 27.8: 995-1004.

[9] GENT, A. Engineering with Rubber How to Design Rubber Components ISBN: 978-3-446-42764-8.

[10] SMITH, L. *The language of rubber: an introduction to the specification and testing of elastomers*. Butterworth-Heinemann, 1993.

[11] DALRYMPLE, T. Experimental Elastomer Analysis Course Notes. *Ann Arbor, Michigan*, 1998.

[12] CHENG, M; CHEN, W. Experimental investigation of the stress–stretch behavior of EPDM rubber with loading rate effects. *International Journal of Solids and Structures*, 2003, 40.18: 4749-4768.

[13] DAY, J. "A Method for Equibiaxial Stretching of Elastomeric Sheets", HKS Michigan Update Seminar and Users' Meeting, Novi, Michigan, November 16, 1999.

[14] REUGE, N., et al. Elastomer biaxial characterization using bubble inflation technique. I: Experimental investigations. *Polymer Engineering & Science*, 2001, 41.3: 522-531.

[15] DAY, J; POWERTRAIN, G. M. Testing and Analysis.

[16] DUNCAN, B. C., et al. Verification of hyperelastic test methods. 1999.

[17] JERRAMS, S; MURPHY, N; HANLEY, J. The significance of equi-biaxial bubble inflation in determining elastomeric fatigue properties. *Advanced Elastomers, Technology, Properties and Applications*, 2012, 379-381.

[18] DEDOVA, S., et al. Dissipative heating, fatigue and fracture behaviour of rubber under multiaxial loading. *Fatigue Crack Growth in Rubber Materials*, 2020, 421-443.

[19] COESFELD: Materialtest [online]. [cit. 2022-04-26]. Available from: https://www.coesfeld.com/en/products/detail/elastomers/dynamic/biaxial-test-stand-dynamic.html

[20] WOLF, D; Experimental Elastomer Analysis

[21] TRELOAR, L. R. G. The physics of rubber elasticity. 1975.

[22] ARRUDA, E. M.; BOYCE, M. C. A three-dimensional constitutive model for the large stretch behavior of rubber elastic materials. *Journal of the Mechanics and Physics of Solids*, 1993, 41.2: 389-412.

[23] YEOH, O. H. Some forms of the strain energy function for rubber. *Rubber Chemistry and technology*, 1993, 66.5: 754-771.

[24] RENAUD, CH., et al. The Yeoh model applied to the modeling of large deformation contact/impact problems. *International Journal of Impact Engineering*, 2009, 36.5: 659-666.

[25] MOONEY, M. A theory of large elastic deformation. *Journal of applied physics*, 1940, 11.9: 582-592.

[26] RIVLIN, R.S. Large elastic deformations of isotropic materials. I. Fundamental concepts. *Philosophical Transactions of the Royal Society of London. Series A, Mathematical and Physical Sciences*, 1948, 240.822: 459-490.

[27] OGDEN, R. W. Large deformation isotropic elasticity–on the correlation of theory and experiment for incompressible rubberlike solids. *Proceedings of the Royal Society of London. A. Mathematical and Physical Sciences*, 1972, 326.1567: 565-584.

[28] TRELOAR, L. R. G. Stress-strain data for vulcanized rubber under various types of deformation. *Rubber Chemistry and Technology*, 1944, 17.4: 813-825.

[29] MARCKMANN, G.; VERRON, E. Comparison of hyperelastic models for rubber-like materials. *Rubber chemistry and technology*, 2006, 79.5: 835-858.

[30] MCCORMICK, N.; LORD, J. Digital image correlation. *Materials today*, 2010, 13.12: 52-54.

[31] YONEYAMA, S.; MURASAWA, G. Digital image correlation. *Experimental mechanics*, 2009, 207.

[32] LEPAGE, W. *Digital Image Correlation* [online]. [cit. 2021-04-07]. Dostupné z: https://digitalimagecorrelation.org/

[33] SUTTON, M. A.; ORTEU, J. J.; SCHREIER, H. *Image correlation for shape, motion, and deformation measurements: basic concepts, theory and applications*. Springer Science & Business Media, 2009.

[34] GAO, Z., et al. Experimental analysis of image noise and interpolation bias in digital image correlation. *Optics and Lasers in Engineering*, 2016, 81: 46-53.

[35] SU, Y., et al. Fourier-based interpolation bias prediction in digital image correlation. *Optics express*, 2015, 23.15: 19242-19260.

[36] REU, P. All about speckles: speckle size measurement. *Experimental Techniques*, 2014, 38.6: 1-2.

[37] REU, P. All about speckles: aliasing. *Experimental Techniques*, 2014, 38.5: 1-3.

[38] REU, P. All about speckles: edge sharpness. *Experimental Techniques*, 2015, 39.2: 1-2.

[39] LEPAGE, W. S.; SHAW, J. A.; DALY, S. H. Optimum paint sequence for speckle patterns in digital image correlation. *Experimental Techniques*, 2017, 41.5: 557-563.

[40] REU, P. Points on paint. *Experimental Techniques*, 2015, 39.4: 1-2.

[41] HU, Y. J., et al. A new method of creating high-temperature speckle patterns and its application in the determination of the high-temperature mechanical properties of metals. *Experimental Techniques*, 2018, 42.5: 523-532.

[42] ZHAO, Z.; MU, X.; DU, F. Modeling and verification of a new hyperelastic model for rubber-like materials. Mathematical Problems in Engineering, 2019, 2019.

[43] ABAQUS, INC. *ABAQUS Analysis User's Manual* [online]. [cit. 2021-5-4]. Dostupnéz:https://classes.engineering.wustl.edu/2009/spring/mase5513/abaqus/docs/v6.5/index.html

LIST OF ABBREVIATIONS

FEM Finite element method

DIC Digital image correlation

NR Natural rubber

BR Polybutadiene rubber

CR Chloroprene rubber

ε Strain [-]

E Young's modulus [MPa]

ν Poisson's ratio

σ Stress [MPa]

μ Shear modulus [Pa]

δ_{ij} Kronecker's delta

λ Lame's constant

κ Bulk modulus [MPa]

W Strain energy density [J/m^3]

λ_i Main stretches [-]

I_i Invariants of right Cauchy – Green strain tensor

l_i Deformed length [m]

l_0 Undeformed length [m]

S_{ij} Second Piola – Kirchhoff stress tensor [Pa]

C_{ij} Right Cauchy – Green strain tensor

p Unspecified pressure [Pa]

k Boltzmann's constant

T Absolute temperature [K]

c_{ij} Material constants [Pa]

n Number of polymer chains in unitary volume

μ_i Material constant

α_i Material constant

λ_L Maximal stretch of micromechanical structure

W_{vol} Strain energy density dependent on bulk modulus [J/m^3]

ISO International Federation of the National Standardizing Associations

ε_x Proportional change in lengthwise dimension [%]

ε_y Proportional change in transverse dimension [%]

L_n Deformed length dependent on immediate strain level

L_{n0} Original length

R^2 Coefficient of determination

P_i Stress – strain values from the original tensile data

$\widehat{P}_i$ Stress – strain values from models' predictions

$\bar{P}$ The average values of P_i

CPS4R Four-node plane stress element

ISA Intrinsic Strength Analyser

m Slope of a curve

UNI_F Unilateral loading principle with flat clamps

UNI_C Unilateral loading principle with cylindrical clamps

BI_F Bilateral loading principle with flat clamps

BI_C Bilateral loading principle with cylindrical clamps

LIST OF FIGURES

LIST OF TABLES